2019

Nonlinear Optical Responses In Type-Ii Weyl Semimetals

Gerui Liu
University of Pennsylvania, liugerui2555@gmail.com

Nonlinear Optical Responses In Type-Ii Weyl Semimetals

Abstract

Weyl semimetals are gapless topological states of matter with broken inversion and/or time reversal symmetry. In this thesis, we will firstly discuss the observation of a novel photogalvanic effect in type-II Weyl semimetals including $\rm T_d-MoTe_2$, $\rm Mo_{0.9}W_{0.1}Te_2$ and $\rm Mo_{0.3}W_{0.7}Te_2$. A circulating photocurrent is obtained under the illumination of normally incident light with circular polarization and the circulating current direction is opposite with different light helicity. Through temperature induced phase transition of $\rm MoTe_2$, this effect is further confirmed to exclusively occur in the Weyl phase. Since this CPGE current is controlled by the spatially varying beam profile, we define the effect as a spatially dispersive circular photogalvanic effect (sCPGE) and current amplitude is proven to be proportional to the beam gradient. By performing frequency-dependent measurements on the Weyl phase, we observe a sign reversal of sCPGE current at high energy excitation and low energy excitation. Our theoretical derivation shows that sCPGE is controlled by a unique symmetry selection rule related to asymmetric carrier excitation and relaxation, explaining the difference between Weyl phase and trivial phase as well as frequency dependent properties.

Photoinduced anomalous Hall effect (AHE) is also observed in type-II Weyl semimetals. Longitudinal CPGE current is obtained under normally incident light while applying transverse bias, and the current magnitude is observed to be proportional to the bias voltage. Comparing the AHE conductivity in the 1T' phase and the $\rm T_d$ phase of $\rm MoTe_2$, photoinduced AHE is found to be much more significant in Weyl phase. This effect can be understood by symmetry arguments and is described by a Fermi surface modulation under the external electric field; meanwhile, the difference between two phases is evaluated. This model further predicts that under low energy excitation, Weyl points can be partially muted with tilted Fermi level, which provides a promising method to probe the band topology and Weyl nodes as well as encode more degree of freedom in device applications.

Our studies on sCPGE and photoinduced AHE in type-II Weyl semimetals provide a new idea of probing and controlling nonlinear optical responses of topological semimetals and will potentially promote the applications of those new material systems.

Degree Type

Dissertation

Degree Name

Doctor of Philosophy (PhD)

Graduate Group

Materials Science & Engineering

First Advisor

Ritesh Agarwal

Keywords

CPGE, NONLINEAR OPTICAL RESPONSES, photoinduced AHE, WEYL SEMIMETALS

Subject Categories

Mechanics of Materials

NONLINEAR OPTICAL RESPONSES IN TYPE-II WEYL SEMIMETALS

Gerui Liu

A DISSERTATION

in

Material Science and Engineering

Presented to the Faculties of the University of Pennsylvania

in

Partial Fulfillment of the Requirements for the

Degree of Doctor of Philosophy

2019

Supervisor of Dissertation

Signature:

Ritesh Agarwal, Professor, Material Science & Engineering

Graduate Group Chairperson

Signature:

Shu Yang, Professor, Material Science & Engineering

Dissertation Committee

Eugene J. Mele, Christopher H. Browne Distinguished Professor of Physics

Nader Engheta, H. Nedwill Ramsey Professor of University of Pennsylvania

Liang Feng, Assistant Professor, Materials Science & Engineering, Electrical & Systems Engineering

NONLINEAR OPTICAL RESPONSES IN TYPE-II WEYL SEMIMETALS

Dedicate to my family.

Acknowledgements

I have discovered on my hard way pursuing the PhD degree that help and support from others are indispensable. Here, I must show my sincere thanks to my professors, collaborators, group members, friends and family.

I am so grateful to get the admission from Professor Ritesh Agarwal to work and study in your group five years ago. You gave me freedom to explore the topics I was interested in and you inspired my creative thinking by scientific questioning step-by-step. You always asked me to think about the big picture which taught me the beauty of science. You encouraged me to collaborate with people in and out of our group, broadening my sight for research. Lessons I learned from not only your guide in research but your personality would be helpful for my professional life now and in the future.

I would like to thank my committee members: Professor Eugene J. Mele, Professor Nader Engheta and Professor Liang Feng. Thank you so much for the discussion with you which greatly helped me to understand the natural of physics. Your advice and support pointed out the right direction for me, significantly pushing the progress of my research.

I must specifically thank to my collaborator Zhurun Ji, one of the most talented and diligent researchers I have ever met in my life. She was only 17 years old when she got into the group, but her maturity and ability was much more than her age. I was truly inspired by her deep thinking and passion in research. I was really grateful to have her as my college in these years.

I also want to thank all members in Agarwal's Group. Some members have already left the group, such as Dr. Rahual Agarwal, Dr. Pavan Nukala, Dr. Joohee Park, Dr. Jacob Berger, Dr. Daksh Agarwal, Dr. Sajal Dhara, Dr. Bumsu Lee, Dr. Ho-Seok EE and Dr. Mingliang Ren, who taught me a lot when I just joined the group. Even though they graduated, they still patiently answered my questions when I needed them. I am grateful to current students and post docs including Yuhui Wang, Gaurav Modi, Harshvardhan Jog, Zijian Xiao and Zhurun Ji of course and Dr. Wenjing Liu, Dr. Hwang Minsoo, Dr. Xiaopeng Fan and Dr. Leem Youngchul who gave me invaluable support.

I feel really lucky to have so much wonderful friends. Thank you Liyan Wu, Xuan Cao, Dequan Er, Zeyu Chen, Sixiang Yu and Zhe Liu. From studying to entertainment, you make my PhD life colorful.

Finally, I must acknowledge my family. Thank you to my parents. Without you, I would not be who I am now. Even though we were living far from each other during my PhD years, I can feel your love and concern. In the end, I want to thank my future wife Jinxi, loving me, supporting me and understanding me for all these years.

ABSTRACT

NONLINEAR OPTICAL RESPONSES IN TYPE-II WEYL SEMIMETALS

Gerui Liu

Ritesh Aagrwal

Weyl semimetals are gapless topological states of matter with broken inversion and/or time reversal symmetry. In this thesis, we will firstly discuss the observation of a novel photogalvanic effect in type-II Weyl semimetals including $T_d - MoTe_2$, $Mo_{0.9}W_{0.1}Te_2$ and $Mo_{0.3}W_{0.7}Te_2$. A circulating photocurrent is obtained under the illumination of normally incident light with circular polarization and the circulating current direction is opposite with different light helicity. Through temperature induced phase transition of $MoTe_2$, this effect is further confirmed to exclusively occur in the Weyl phase. Since this CPGE current is controlled by the spatially varying beam profile, we define the effect as a spatially dispersive circular photogalvanic effect (sCPGE) and current amplitude is proven to be proportional to the beam gradient. By performing frequency-dependent measurements on the Weyl phase, we observe a sign reversal of sCPGE current at high energy excitation and low energy excitation. Our theoretical derivation shows that sCPGE is controlled by a unique symmetry selection rule related to asymmetric carrier excitation and relaxation, explaining the difference between Weyl phase and trivial phase as well as frequency dependent properties.

Photoinduced anomalous Hall effect (AHE) is also observed in type-II Weyl semimetals. Longitudinal CPGE current is obtained under normally incident light while applying transverse bias, and the current magnitude is observed to be proportional to the bias voltage. Comparing the AHE conductivity in the 1T' phase and the T_d phase of $MoTe_2$, photoinduced AHE is found to be much more significant in Weyl phase. This effect can

be understood by symmetry arguments and is described by a Fermi surface modulation under the external electric field; meanwhile, the difference between two phases is evaluated. This model further predicts that under low energy excitation, Weyl points can be partially muted with tilted Fermi level, which provides a promising method to probe the band topology and Weyl nodes as well as encode more degree of freedom in device applications.

Our studies on sCPGE and photoinduced AHE in type-II Weyl semimetals provide a new idea of probing and controlling nonlinear optical responses of topological semimetals and will potentially promote the applications of those new material systems.

Contents

List of Figures

List of Tables

Chapter 1

Introduction

1.1 Topological Semimetal

For a long history, materials were simply divided into metal, semiconductor and insulator according to their conductivity. For insulators and semiconductors, the filled valence band is separated from the empty conduction band by a band gap. On the contrast, the conduction band for a metal is partially filled leading to an appreciable density of states at Fermi level. Semimetal is a material partway between metals and semiconductor, with a slight overlap between the conduction band and the valence band. The density of states at the Fermi level for semimetal is much smaller than real metal even though it has no band gap. More specifically in semimetals, topological

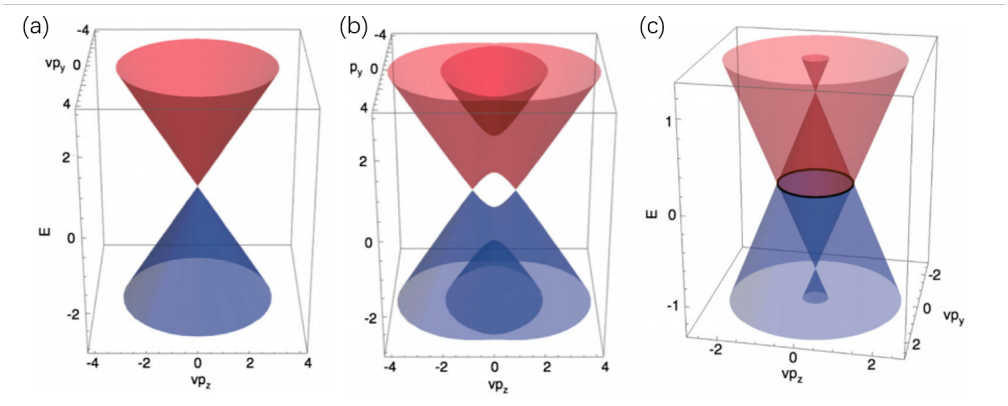

FIGURE 1.1: Energy spectra of (a)Dirac semimetal, (b)Weyl semimetal and (c)nodal line semimetal. Reprinted figure with permission from reference [1] Copyright (2019) by the American Physical Society.

semimetal is characterized by the topologically band crossing, which is a new class of quantum materials. [1] In recent decade, topological semimetals has attached a lot of interests in fundamental studies as well as macroscopic phenomena for promising technological applications.

Based on properties of the band crossing, such as the degeneracy and the geometry, topological semimetals are distinguished into several types including Dirac semimetal [2–4], Weyl semimetal [5, 16] and nodal line semimetal [7]. Simply speaking, Dirac semimetal consists of a pair of degenerate linear band; bands of Weyl semimetal touches at a pair of isolated points; in nodal line semimetal, two bands cross each other along a closed curve. The energy spectra of these three topological materials are given in the Fig 1.1. [1] With different band crossing structure, topological semimetals host different low energy excitations and exhibits various properties, motivating studies in wide area. In this thesis, we mainly works on one of these topological materials - Weyl semimetal.

1.1.1 Basic Concepts of Weyl Semimetal

Hermann Weyl simplified the Dirac equation to demonstrate the existence of massless fermion with finite chirality in 1929. [8]. With m=0, the Dirac equation can be expressed as:

$$i\hbar\frac{\partial}{\partial t}\chi_{\pm} = \pm c\boldsymbol{\sigma}\cdot\boldsymbol{p}\chi_{\pm} \tag{1.1}$$

This is the Weyl equation and the χ is referred to the Weyl fermions and a pair of opposite charality Weyl fermions can be combined to obtain a Dirac fermion. The Weyl semimetal is a solid state crystal with Weyl fermions acting as low energy exitations. In Weyl semimetal, non-degenerate bands touching occurs in the three-dimensional momentum space forming linear dispersion. Suppose two bands touching at point $\boldsymbol{k}_0$ and energy ϵ_0, the Hamiltonian can be expressed as:

$$H(\boldsymbol{k}) = \epsilon_0\sigma_0 \pm \hbar v_f(\boldsymbol{k}-\boldsymbol{k}_0)\cdot\boldsymbol{\sigma} \tag{1.2}$$

where σ_0 is a unit matrix, $\boldsymbol{\sigma}$ is the Pauli matrix, $\boldsymbol{k}$ represents the momentum and v_f is the Fermi velocity. [9] If the band touching point is set to be zero and this Hamiltonian becomes the exact Weyl Hamiltonian. Clearly, the band crossing is robust and irremovable no matter how to change parameters in this expression if non-degenerated bands in three-dimensional system is satisfied. To meet these requirements, time reversal symmetry and inversion symmetry can not be preserved at the same time, which means that Weyl semimetal breaks either inversion symmetry or time reversal symmetry.

The topology of the Weyl point is understood by the Berry curvature. The eigenstates of Eqn 1.2 can be labelled by the sign of $\boldsymbol{\sigma}$ projected on $\boldsymbol{k}$ (helicity). For each helicity, the expectation value of $\boldsymbol{\sigma}$ forms a vector field around the Weyl point in momentum space, acting as a source or a sink. The Weyl points behave as monopole and antimonopole correspondingly, characterized by a topological invariant:

$$\boldsymbol{\Omega}(\boldsymbol{k}) = \pm\frac{\boldsymbol{k}}{2|\boldsymbol{k}|^3} \tag{1.3}$$

[9] The sign represents the chirality of the Weyl nodes. The chirality χ is defined as:

$$\chi = \frac{1}{2\pi}\oint \boldsymbol{\Omega}(\boldsymbol{k}) \cdot d\boldsymbol{s}(\boldsymbol{k}) \tag{1.4}$$

This flux of vector enclosing the Weyl nodes by a surface in $\boldsymbol{k}$ space is called Berry curvature. For a pair of Weyl nodes, the chirality is opposite. [10]

1.1.2 Discovery of Weyl Semimetal

As mentioned above, since time reversal or inversion symmetry needs to be broken for Weyl semimetal, two categories of Weyl semimetals were theotically calculated and predicted. The first one is time reversal symmetry broken candidates such as magenetic pyrochlories $A_2Ir_2O_7$ [11], ferromagenetic hald-metal $HgCr_2Se_4$ and $Hg_{1-x-y}Cd_xMn_yTe$ [12,13]. However, these compounds were failed to be experimentally observed. In 2016,

Co-based Heusler compounds were proposed as Weyl semimetal [14] and proven by giant anomalous Hall effect [15]

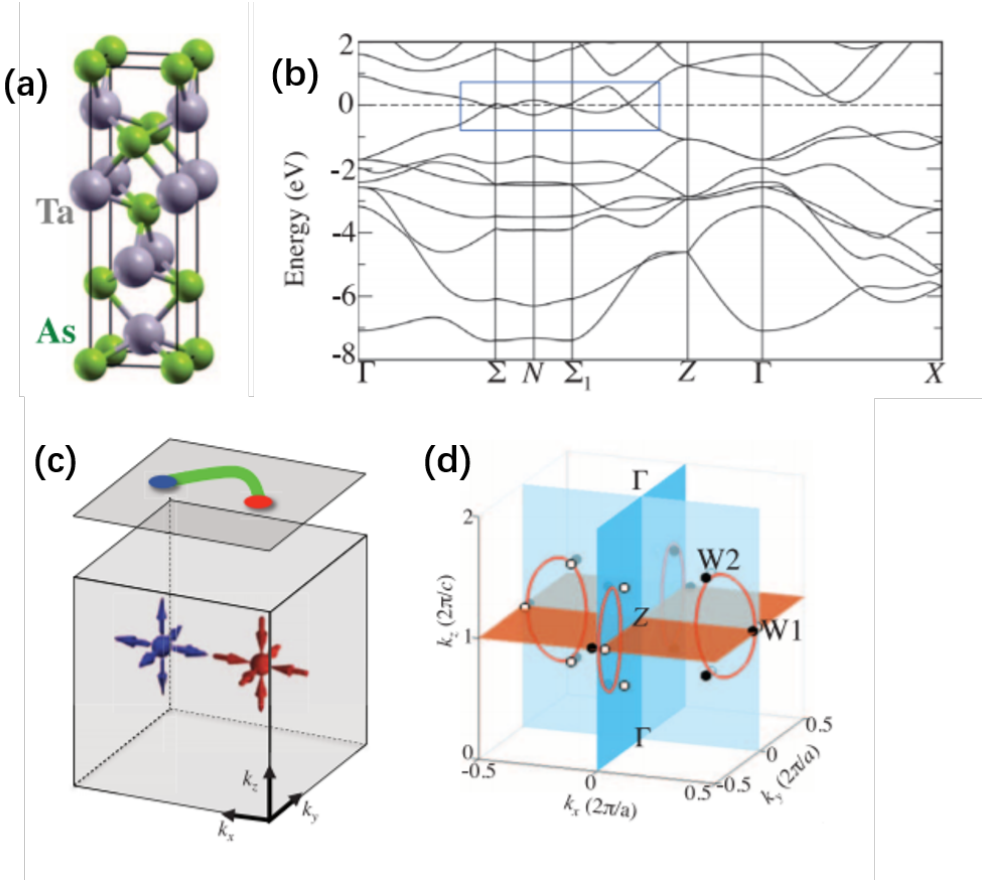

FIGURE 1.2: (a) Body-centered tetragonal structure of TaAs, shown as stacked Ta and As layers. The lattice of TaAs does not have space inversion symmetry.(b) First-principles band structure calculations of TaAs without spin-orbit coupling. The blue box highlights the locations where bulk bands touch in the BZ. (c) Illustration of the simplest Weyl semimetal state that has two single Weyl nodes with the opposite (T1) chiral charges in the bulk. (d) In the absence of spin-orbit coupling, there are two line nodes on the kx mirror plane and two line nodes on the ky mirror plane (red loops). In the presence of spin-orbit coupling, each line node reduces into six Weyl nodes (small black and white circles). Black and white show the opposite chiral charges of the Weyl nodes. Reprinted figure with permission of [18]

The other category is achieving Weyl semimetal by breaking inversion symmetry with strong spin-orbit coupling. Angle-resolved photoemission spectroscopy (ARPES), a tool can directly observe the band structure of a material, was utilized to obtain the band crossing and Weyl nodes in nonmagentic Weyl semimetals. In 2015, TaAs, TaP, NbAs, and NbP were calculated by theorists [16, 17] and the Fermi arc in TaAs

was directly observed by ARPES in the same year, indicating the realization of three-dimensional Weyl semimetal. [18–20]. Later on, more and more compounds of Weyl semimetals were discovered in theory and observed in experiments, including Na_3Bi, Cd_3As_2, $MoTe_2$, $MoWTe_2$ alloys, WTe_2 and $TaIrTe_4$. [21–24, 26–31]

Take TaAs family as example. (Fig 1.2) This compound is a semimetallic material whose crystallization is body centered tetragonal lattice and space group is $I4_1md$ (number109, C_{4v}). [18] Calculation has demonstrated that the conduction band and the valence band cross on the k_x and k_y plane when the SOC is turned off. When the SOC is turned on, the band structure would form spin splitting because of the noncentrosymmetric structure. Each line node will be gapped out and shrink into six Weyl nodes away from the original mirror planes, which will finally result in 24 bulk Weyl nodes. 8 Weyl nodes are located at the $k_z = \frac{2\pi}{c}$ plane marked as W1. The other 16 nodes that are away from this plane as marked by W2. These 24 Weyl cones are all linear dispersive and are associated with single chiral charge of ± 1. [18] In experiments, the surface and bulk electronic structure of TaAs including the topological Fermi arc and bulk Weyl cones were observed by the vacuum ultraviolet and soft X-ray ARPES. Beacuse of the unique band structure, the discovery of the Weyl semimetals motivated researchers to characterize the nontrivial topology of these materials such as the unusual magnetoresistance and the chiral anomaly. Negative magnetoresistance induced by chiral anomaly was observed in TaAs [25] and extremely large magnetoresistance and ultrahigh mobility were also obtained in the TaAs family [32].

1.1.3 Type-II Weyl Semimetal

The concept of type-II Weyl semimetal was firstly introduced by Soluyanov in the late 2015 [26] according to the calculation on the layered transition-metal dichalcogenide WTe_2. To distinguish from the previously discovered Weyl semimetal whose Fermi surface at Weyl point is point-like, this new type Weyl semimetal has Weyl fermions emerging at boundary between electron and hole pockets. Since the formation of the Weyl point is different, the Weyl cone for type-II has a tilted shape as shown

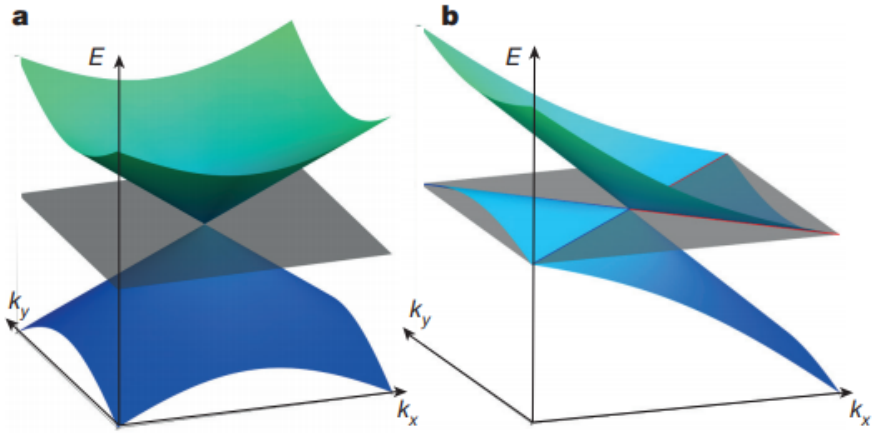

FIGURE 1.3: Possible types of Weyl semimetals. (a) Type-I WP with a point like Fermi surface. (b) A type-II WP appears as the contact point between electron and hole pockets. The grey plane corresponds to the position of the Fermi level, and the blue (red) lines mark the boundaries of the hole (electron) pockets. Reprinted figure with permission of [26]

in Fig 1.3, even though it is still linear dispersive. The crystal structure of WTe_2 is orthorhombic with space group $Pmn2_1(C_{2v}^7)$, which is a layered structure. By calculating the band structure of WTe_2 with and without SOC, the Weyl points were found to be located only slightly (0.052eV and 0.058eV) above the Fermi energy with very small separation, which was very difficult to be observed in the resolution of ARPES. Actually, whether WTe_2 is Weyl semimetal is still controversial due to the tiny Fermi arc. Then, $MoTe_2$ was found to be a strong candidate for this new type Weyl semimetal and the calculation was proposed very soon by Sun. [33]

$MoTe_2$ which is also a layered transition metal dichalcogenide, has three crystalline phsaes: 2H, 1T′ and T_d phases, in which 2H phase is semiconducting having Mo atom trigonal primatic coordinated with Te atoms. The 1T′ and T_d are semimetallic phases exhibiting very similar layered structure. 1T′ phase structure has inversion symmetry with space group $P12_1/m1$, No. 11, while the T_d (space group $Pmn2_1$, No. 31) breaks the symmetry by slightly sliding the later stacking of the monoclinic lattice of 1T′ phase. Since 1T′ preserves both time reversal symmetry and inversion symmetry, T_d phase is the only one that could be Weyl semimetal. Via ab initio DFT calculation, four pairs of Weyl points were found in the band structure of T_d-$MoTe_2$. [33]

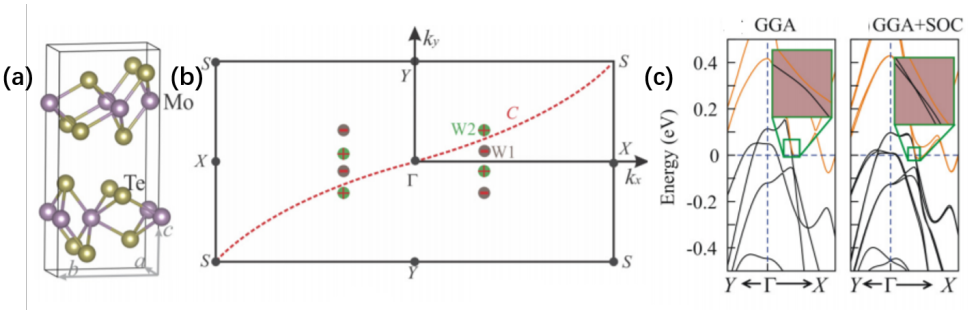

FIGURE 1.4: (a) Orthorhombic crystal lattice structure of T_d phase $MoTe_2$ in the space group of $Pnm2_1$. (b) Brillouin zone (BZ) in the $k_z = 0$ plane. WPs with positive and negative chiralities are marked as green and gray dots. The evolution of Wannier charge centers between the Γ and S points is calculated along the red curve (c)Bulk band structure around the Γ point in the $Y - \Gamma - X$ direction without and with the inclusion of SOC. Reprinted figure with permission from reference [33] Copyright (2019) by the American Physical Society.

As shown in Fig 1.4, each pair of Weyl points showed about 4.2% spacing in the Brillouin zone where two Weyl points located merely 6mV and 59mV above the Fermi energy respectively. Different from the WTe_2, this large spacing in the reciprocal lattice vector of Weyl points as well as small energy difference between Weyl points and Fermi energy make Fermi arcs much easier to be observed in experiment by ARPES. [33] Similarly, $Mo_xW_{1-x}Te_2$ alloys were also predicted to be Type-II Weyl semimetals, sharing the same property with T_d- $MoTe_2$. Besides, the length of the Fermi arcs was tunable by the concentration x of Mo composition according to the calculation. The Fermi arc would be enlarged with higher Mo doping, which agreed with the previous calculation on $MoTe_2$ and WTe_2. [34] The tunability of the length of the Fermi arcs also shines light on studying the influence of the Fermi arc by adjusting the doping level.

With the rapid development of theory prediction, $MoTe_2$ family was directly observed as type-II Weyl semimetal very soon. Take the $MoTe_2$ as an example. (Fig 1.5) [27] Comparing the calculated band structure of T_d phase $MoTe_2$ and the real structure obtained by ARPES, an agreement indicated a clear evidence of Weyl points formed by the electron pocket and hole pocket. With the absence of Fermi arc in centrosymmetric 1T' phase, the origin of the Weyl semi-metallic state in this material was further confirmed.

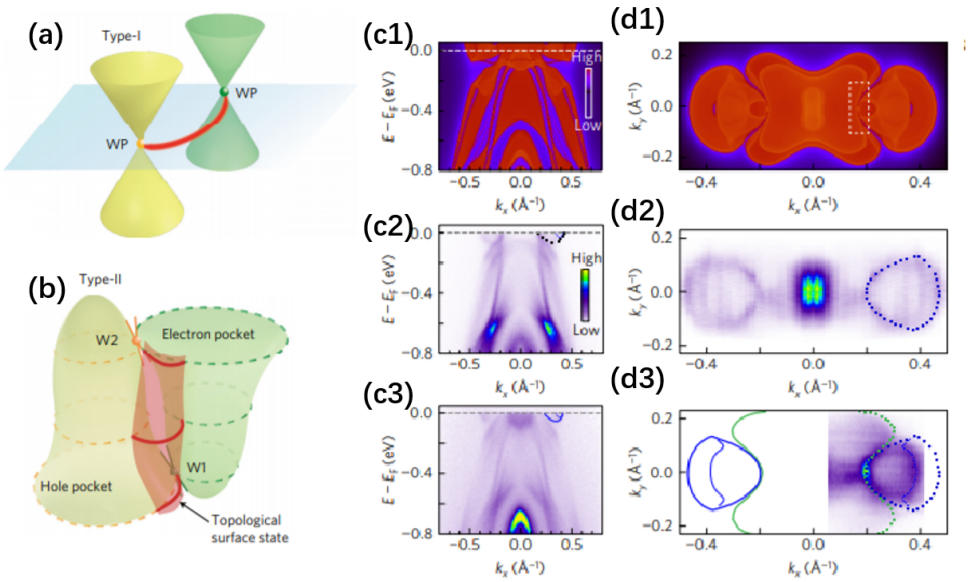

FIGURE 1.5: (a) Dispersions for type-I Weyl fermion near Fermi energy. The WPs are labelled by yellow and green dots. (b) Type-II Weyl semimetal with electron and hole pockets touching at two different energies. (c1) Calculated dispersion along the $X - \Gamma - X$ direction. (c1&2) Measured dispersions along the $X - \Gamma - X$ direction with horizontal and vertical polarizations at photon energy of 32.5 eV. (d) Calculated spectral function at Fermi energy. (d1&2) Intensity maps measured at Fermi energy with p polarization using a 6.3 eV laser source with light polarizations perpendicular to the b and a axis respectively. The electron and hole pockets are highlighted by blue and green colour. Reprinted figure with permission of [27]

Other than the transport measurements of unusual magnetoresistance [35], the inversion symmetry breaking property also inspires the possibility of nonlinear optical response. such as the second harmonic generation, photovoltaic and photogalvanice effect. In this thesis, we will focus on the nonlinear optical response, especially the photogalvanic effect in type-II Weyl semimetal.

1.2 Photogalvanic Effect

Photogalvanic effect (PGE) is the phenomenon of a direct current (dc) generated in a homogeneous medium under uniform illumination, which occurs in media lacking of centrosymmetry. PGE has been widely studied in a lot of materials such as ferroelectircs, piezoelectrics and gyrotropic crystals for probing the symmetry and band information as well as potential electronics applications.

1.2.1 Phenomenological Description

For a phenomenological description, the electric current in a homogeneous medium can be expanded in a power series of the electric field:

$$j_i = \sigma^0_{ij} E_j + \beta^0_{inl} E_l E_n + \sigma^0_{ilnm} E_l E_n E_m + \gamma_{ilnm} E_l E'_n E'^*_m + \beta_{iln} E'_l E'^*_n \tag{1.5}$$

where E is the electric field and $E'(\omega) = E'^*(-\omega)$ is the intensity of illumination. The first three terms represents the conductivity considering the nonlinear correction. The fourth term is the photoconductivity, defined as j^{ph}_i. PGE is described by the last term with second order of E and the property of PGE is governed by the photogalvanic tensor $\beta_{iln}(\omega)$. [36]

Since the current j^{ph}_i should changes sign under inversion but $E'_l E'^*_n$ keeps the sign, $\beta_{iln}(\omega)$ needs to consist of centrosymmetric breaking elements. Besides, for real j^{ph}_i, photogalvanic tensor satisfies $\beta_{iln}(\omega) = \beta^*_{inl}(\omega)$, indicating real component of $\beta_{iln}(\omega)$ is symmetric with index l and n. The independent components is determined by the crystal structure. In the crystals of class T and T_d, there is only one independent component in the tensor. [36] The type-II Weyl semimetal, such as the $MoTe_2$ and $MoWTe_2$ alloys with T_d phase, is expected to exhibit PGE in principle.

1.2.2 Circular Photogalvanic Effect

Among all PGE, we mainly focus on the circular photogalvanic effect (CPGE) which descibes the helicity-dependent photocurrent. Photocurrent of CPGE only appears under the exciation of circularly polarized light and the photocurrent direction is reversed while changing the sign of circular polarization. The CPGE photocurent can be understood by a simple explanation that the photon angular momenta is transformed into the motion of a free carrier for two reasons: wheel effect and screw effect. [37] The photon helicity can be described by the degree of circular polarization:

$$P_c = \frac{I_{\sigma+} - I_{\sigma-}}{I_{\sigma+} + I_{\sigma-}} \tag{1.6}$$

where $I_{\sigma\pm}$ are the light intensity of right ($\sigma+$) and left ($\sigma-$) handed circularly polarized light.

From the phenomenological equation of current response mentioned above, the tensor β can be separated into two parts:

$$j_i = \beta_{iln} E'_l E'^*_n = \frac{1}{2}(\beta_{iln} + \beta_{inl}) E'_l E'^*_n + \frac{1}{2}(\beta_{iln} - \beta_{inl}) E'_l E'^*_n \tag{1.7}$$

The first term is the symmetric part, describing the linear photogalvanic effect (LPGE); while the second term is the antisymmetric part, describing CPGE, which can be written as:

$$j_{i,CPGE} = \frac{1}{2}(\beta_{iln} - \beta_{inl}) E'_l E'^*_n = \beta^{anti}_{iln} P_c E'_l E'^*_n \tag{1.8}$$

The antisymmetric tensor β^{anti}_{iln} is related to the point group and gyrotropy of the system. In all 21 crystal classes breaking inversion symmetry, 3 of them are nongyrotropic which are T_d, C_{3h} and D_{3h}. [37] This effect, predicted by Ivchenko and Belinicher in 1978 [38,39], was experimentally obtained by Asnin [40] in the same year. Later on, this effect was broadly studied in quantum well structures, topological insulators and other materials due to the reduction of symmetry.

1.2.3 CPGE in Weyl Semimetal

The discovery of Weyl semimetal with topological band crossing motivated the study of nonlinear optical response in these materials, including the CPGE. The theoretical calculation was proposed in 2017 by Chan, who predicted a significant photocurrent in Weyl semimetal with inversion symmetry breaking and tilted Weyl cone. [42]

As shown in the Fig 1.6, in the Dirac system, the electron in two branches will be excited symmetrically by the circularly polarized light. The excited electrons have same magnitude but opposite direction momentum resulting in zero net current. Different from the Dirac system, the Weyl semimetal breaks either time reversal symmetry or inversion symmetry, and each Weyl cone has finite chirality. In a single Weyl cone, the asymmetric excitation by circularly polarized light allows the net photocurrent whose

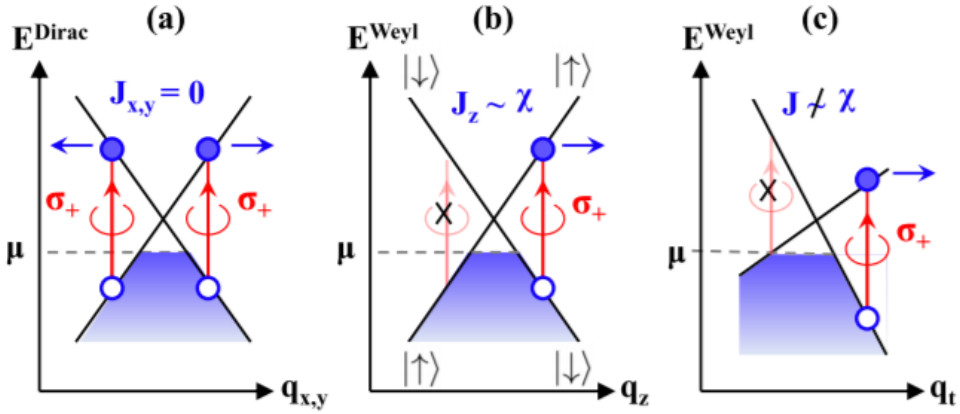

FIGURE 1.6: Schematics of photocurrent generations in Dirac and Weyl systems. Circularly polarized photons propagating along the z axis induce spin-flip vertical transitions denoted by the red arrows. (a) In an ideal 2D Dirac system, the excitations are symmetricabout the node and thus the photocurrent vanishes. (b) In a 3D Weyl system with an upright crossing spectrum, the extra dimension allows an asymmetric particle-hole excitation along q_z and creates a chirality-dependent photocurrent from each Weyl cone. However, the chiral currents from a monopole and an antimonopole negate each other, yielding no net current. (c) In the presence of tilt along some direction q_t , asymmetric excitations can happen when the system is doped away from the neutrality. The resultant photocurrent is not just determined by the node chirality and the total current is generically nonzero. Reprinted figure with permission from reference [42] Copyright (2019) by the American Physical Society.

direction is governed by the chirality of this Weyl cone. However, the Weyl cones in Weyl semimetal appear in pairs with opposite chairlaty, which means that a pair of Weyl cones will generate the same magnitude of photocurrent but different sign, thus vanish each other. As mentioned above, the type-II Weyl semimetal has tilted Weyl cone which can further reduced the symmetry, making the net photocurrent possible. For some Type-II Weyl semimetals, such as $MoWTe_2$ family, the inversion symmetry is broken but time reversal symmetry is preserved. Therefore, the monopoles and antimonopoles are not symmetry related but have different tilts, suggesting a finite net current. The combination of inversion symmetry breaking and tilted Weyl cone allows the existence of photocurrent, in other words, CPGE is expected in these materials. [42]

Shortly after this prediction, Ma observed the CPGE in TaAs, a type-I Weyl semimetal, and concluded it as a direct observation of Weyl fermion chirality. To detect the chirality of Weyl fermion, sensitivity to the WF chirality is required, and CPGE is a good

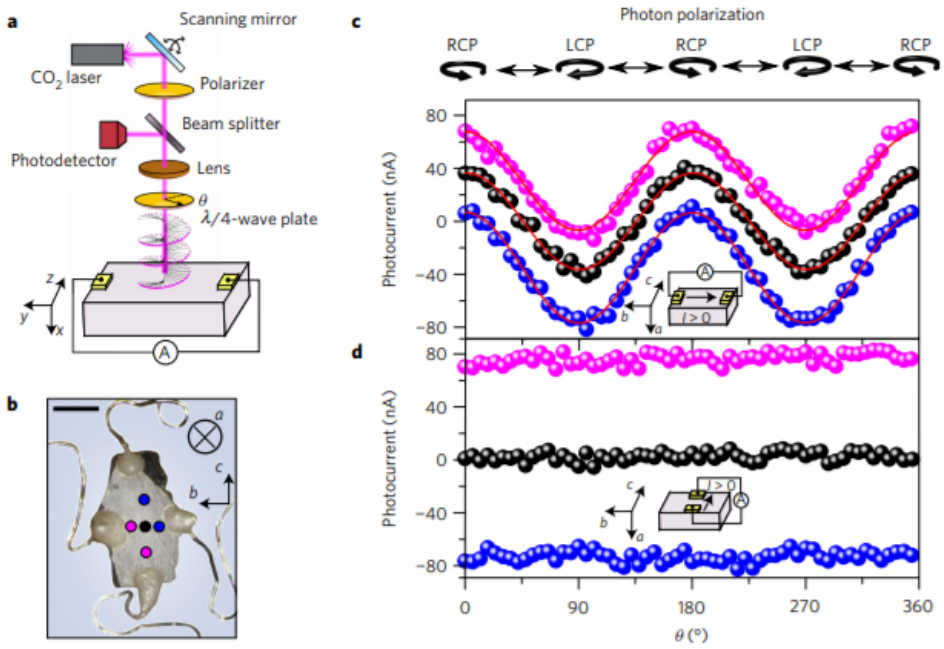

FIGURE 1.7: (a) Schematic illustration of the mid-IR photocurrent microscope setup. A laser power about 10 mW was used throughout the main text. (b) A photograph of the measured TaAs sample. The crystal axes a, b, c are denoted. Scale bar: 300 um. (c,d) Polarization-dependent photocurrents at T=10 K measured along the b axis (c) or c axis (d) direction with the laser applied at the horizontally (c) or vertically (d) aligned pink, black and blue dots in b. LCP, left-handed circularly polarized. Reprinted figure with permission of [43]

option. TaAs has inversion symmetry breaking and the tilt of the Weyl cone was also claimed to be large enough for net photocurrent according to Ma's calculation. [43] Mid IR laser with 10.6um wavelength was used in their experiments to excite electrons from the lower part of Weyl cone to the upper part. Controlling the light polarization by a quarter wave plate, they detected maximum current in b axis for RCP light, minimum for LCP and zero for linearly polarized light, without considering the polarization independent current. The total photocurrent was a cosine function in agreement with the CPGE behavior. In the c direction, the CPGE current was not observable because of the symmetry. The photcurrent can be expressed as : [43]

$$J_\alpha = \eta_{\alpha\beta\gamma} E_\beta(\omega) E^*_\gamma(\omega) \tag{1.9}$$

in which the $\eta_{\alpha\beta\gamma}$ was the second order photocurrent response tensor, an intrinsic property of the material. According to the symmetry of TaAs, there was cancellation in certain directions. Because the photon energy for the excitation was 120meV, they excluded other mechanisms and focused on the transition in the Weyl cone. By microscopic model, they founded that the photocurrent from W2 Weyl cone was negligible and the current direction predicted from W1 agreed with the experimentally measured results. Therefore, they thought this CPGE current singly probed the chirality of the W1 Weyl cone. By different doping, they predicted that the other Weyl point could also be probed by CPGE.

1.3 Thesis Outline

In this thesis, we are going to show our effort to broaden the concept of conventional CPGE via different methods to reduce the symmetry such as beam profile gradient and electric field, and demonstrate for further device applications. Utilizing the platform of Weyl semimetal with strong spin orbit coupling and inversion symmetry breaking, we will try to achieve new types of CPGE with novel response function working in a wider range of energy, which can be used as a more general tool to study the band topology of the material.

In Chapter 2, we will show the observation of CPGE in Type-II Weyl semimetal under the condition that the conventional CPGE should be forbidden. By the measurements on different locations of the sample, we discovered a unique spatial dependent property of this CPGE. Through repeating the CPGE experiments on different phases of $MoTe_2$, we also found that this new type of CPGE only exists in Weyl phase and named it as spatially dispersive CPGE (sCPGE).

Chapter 3 explores more properties of this sCPGE and confirms that the sCPGE current is swirling around the beam center, instead of flowing in a certain direction as conventional CPGE. Using a microscopic model to explain this sCPGE, we also performed wavelength dependent sCPGE measurements and confirmed that the results

were in good agreement with the prediction by the model, helping us to deep dive the topological physics of Weyl semimetal including the electric band structure and the Berry curvature.

Chapter 4 further discusses another way to break the symmetry in Weyl semimetal to obtain CPGE. The CPGE current can be induced and controlled by a transverse bias voltage. In other words, we observed photoinduced anomalous Hall effect in Weyl semimetal which has time reversal symmetry without magnetic field. The symmetry is broaken by the circularly polarized light. This Chapter ends up with the discussion of a microscopic model to explain the origin of the phenomenon, and a low energy excitation experiment was designed to separate the contribution from two Weyl cones under different transverse bias.

Bibliography

[1] Armitage, N.P., Mele, E.J. and Vishwanath, A., 2018. Weyl and Dirac semimetals in three-dimensional solids. Reviews of Modern Physics, 90(1), p.015001.

[2] Young, S.M., Zaheer, S., Teo, J.C., Kane, C.L., Mele, E.J. and Rappe, A.M., 2012. Dirac semimetal in three dimensions. Physical review letters, 108(14), p.140405.

[3] Wang, Z., Sun, Y., Chen, X.Q., Franchini, C., Xu, G., Weng, H., Dai, X. and Fang, Z., 2012. Dirac semimetal and topological phase transitions in A 3 Bi (A= Na, K, Rb). Physical Review B, 85(19), p.195320.

[4] Wang, Z., Weng, H., Wu, Q., Dai, X. and Fang, Z., 2013. Three-dimensional Dirac semimetal and quantum transport in Cd 3 As 2. Physical Review B, 88(12), p.125427.

[5] Weng, H., Fang, C., Fang, Z., Bernevig, B.A. and Dai, X., 2015. Weyl semimetal phase in noncentrosymmetric transition-metal monophosphides. Physical Review X, 5(1), p.011029.

[6] Huang, S.M., Xu, S.Y., Belopolski, I., Lee, C.C., Chang, G., Wang, B., Alidoust, N., Bian, G., Neupane, M., Zhang, C. and Jia, S., 2015. A Weyl Fermion semimetal with surface Fermi arcs in the transition metal monopnictide TaAs class. Nature communications, 6, p.7373.

[7] Horava, P., 2005. Stability of Fermi surfaces and K theory. Physical review letters, 95(1), p.016405.

[8] Weyl, H., 1929. Gravitation and the electron. Proceedings of the National Academy of Sciences, 15(4), pp.323-334.

[9] Burkov, A.A., Hook, M.D. and Balents, L., 2011. Topological nodal semimetals. Physical Review B, 84(23), p.235126.

[10] Yan, B. and Felser, C., 2017. Topological materials: Weyl semimetals. Annual Review of Condensed Matter Physics, 8, pp.337-354.

[11] Wan, X., Turner, A.M., Vishwanath, A. and Savrasov, S.Y., 2011. Topological semimetal and Fermi-arc surface states in the electronic structure of pyrochlore iridates. Physical Review B, 83(20), p.205101.

[12] Xu, G., Weng, H., Wang, Z., Dai, X. and Fang, Z., 2011. Chern semimetal and the quantized anomalous Hall effect in $HgCr_2Se_4$. Physical review letters, 107(18), p.186806.

[13] Bulmash, D., Liu, C.X. and Qi, X.L., 2014. Prediction of a Weyl semimetal in $Hg_{1-x-y}Cd_xMn_yTe$. Physical Review B, 89(8), p.081106.

[14] Wang, Z., Vergniory, M.G., Kushwaha, S., Hirschberger, M., Chulkov, E.V., Ernst, A., Ong, N.P., Cava, R.J. and Bernevig, B.A., 2016. Time-reversal-breaking Weyl fermions in magnetic Heusler alloys. Physical review letters, 117(23), p.236401.

[15] Liu, E., Sun, Y., Kumar, N., Muechler, L., Sun, A., Jiao, L., Yang, S.Y., Liu, D., Liang, A., Xu, Q. and Kroder, J., 2018. Giant anomalous Hall effect in a ferromagnetic kagome-lattice semimetal. Nature physics, 14(11), p.1125.

[16] Huang, S.M., Xu, S.Y., Belopolski, I., Lee, C.C., Chang, G., Wang, B., Alidoust, N., Bian, G., Neupane, M., Zhang, C. and Jia, S., 2015. A Weyl Fermion semimetal with surface Fermi arcs in the transition metal monopnictide TaAs class. Nature communications, 6, p.7373.

[17] Weng, H., Fang, C., Fang, Z., Bernevig, B.A. and Dai, X., 2015. Weyl semimetal phase in noncentrosymmetric transition-metal monophosphides. Physical Review X, 5(1), p.011029.

[18] Xu, S.Y., Belopolski, I., Alidoust, N., Neupane, M., Bian, G., Zhang, C., Sankar, R., Chang, G., Yuan, Z., Lee, C.C. and Huang, S.M., 2015. Discovery of a Weyl fermion semimetal and topological Fermi arcs. Science, 349(6248), pp.613-617.

[19] Lv, B.Q., 2015. BQ Lv, HM Weng, BB Fu, XP Wang, H. Miao, J. Ma, P. Richard, XC Huang, LX Zhao, GF Chen, Z. Fang, X. Dai, T. Qian, and H. Ding, Phys. Rev. X 5, 031013 (2015). Phys. Rev. X, 5, p.031013.

[20] Yang, L.X., Liu, Z.K., Sun, Y., Peng, H., Yang, H.F., Zhang, T., Zhou, B., Zhang, Y., Guo, Y.F., Rahn, M. and Prabhakaran, D., 2015. Weyl semimetal phase in the non-centrosymmetric compound TaAs. Nature physics, 11(9), p.728.

[21] Liu, Z.K., Zhou, B., Zhang, Y., Wang, Z.J., Weng, H.M., Prabhakaran, D., Mo, S.K., Shen, Z.X., Fang, Z., Dai, X. and Hussain, Z., 2014. Discovery of a three-dimensional topological Dirac semimetal, Na3Bi. Science, 343(6173), pp.864-867.

[22] Liu, Z.K., Jiang, J., Zhou, B., Wang, Z.J., Zhang, Y., Weng, H.M., Prabhakaran, D., Mo, S.K., Peng, H., Dudin, P. and Kim, T., 2014. A stable three-dimensional topological Dirac semimetal Cd 3 As 2. Nature materials, 13(7), p.677.

[23] Neupane, M., Xu, S.Y., Sankar, R., Alidoust, N., Bian, G., Liu, C., Belopolski, I., Chang, T.R., Jeng, H.T., Lin, H. and Bansil, A., 2014. Observation of a three-dimensional topological Dirac semimetal phase in high-mobility Cd 3 As 2. Nature communications, 5, p.3786.

[24] Borisenko, S., Gibson, Q., Evtushinsky, D., Zabolotnyy, V., Büchner, B. and Cava, R.J., 2014. Experimental realization of a three-dimensional Dirac semimetal. Physical review letters, 113(2), p.027603.

[25] Huang, X., Zhao, L., Long, Y., Wang, P., Chen, D., Yang, Z., Liang, H., Xue, M., Weng, H., Fang, Z. and Dai, X., 2015. Observation of the chiral-anomaly-induced negative magnetoresistance in 3D Weyl semimetal TaAs. Physical Review X, 5(3), p.031023.

[26] Soluyanov, A.A., Gresch, D., Wang, Z., Wu, Q., Troyer, M., Dai, X. and Bernevig, B.A., 2015. Type-ii weyl semimetals. Nature, 527(7579), p.495.

[27] Deng, K., Wan, G., Deng, P., Zhang, K., Ding, S., Wang, E., Yan, M., Huang, H., Zhang, H., Xu, Z. and Denlinger, J., 2016. Experimental observation of topological Fermi arcs in type-II Weyl semimetal MoTe 2. Nature Physics, 12(12), p.1105.

[28] Huang, L., McCormick, T.M., Ochi, M., Zhao, Z., Suzuki, M.T., Arita, R., Wu, Y., Mou, D., Cao, H., Yan, J. and Trivedi, N., 2016. Spectroscopic evidence for a type II Weyl semimetallic state in MoTe 2. Nature materials, 15(11), p.1155.

[29] Wang, C., Zhang, Y., Huang, J., Nie, S., Liu, G., Liang, A., Zhang, Y., Shen, B., Liu, J., Hu, C. and Ding, Y., 2016. Observation of Fermi arc and its connection with bulk states in the candidate type-II Weyl semimetal WTe 2. Physical Review B, 94(24), p.241119.

[30] Belopolski, I., Sanchez, D.S., Ishida, Y., Pan, X., Yu, P., Xu, S.Y., Chang, G., Chang, T.R., Zheng, H., Alidoust, N. and Bian, G., 2016. Discovery of a new type of topological Weyl fermion semimetal state in $Mo_xW_{1-x}Te_2$. Nature communications, 7, p.13643.

[31] Belopolski, I., Yu, P., Sanchez, D.S., Ishida, Y., Chang, T.R., Zhang, S.S., Xu, S.Y., Mou, D., Zheng, H., Chang, G. and Bian, G., 2016. A minimal," hydrogen atom" version of an inversion-breaking Weyl semimetal. arXiv preprint arXiv:1610.02013.

[32] Shekhar, C., Nayak, A.K., Sun, Y., Schmidt, M., Nicklas, M., Leermakers, I., Zeitler, U., Skourski, Y., Wosnitza, J., Liu, Z. and Chen, Y., 2015. Extremely large magnetoresistance and ultrahigh mobility in the topological Weyl semimetal candidate NbP. Nature Physics, 11(8), p.645.

[33] Sun, Y., Wu, S.C., Ali, M.N., Felser, C. and Yan, B., 2015. Prediction of Weyl semimetal in orthorhombic MoTe 2. Physical Review B, 92(16), p.161107.

[34] Chang, T.R., Xu, S.Y., Chang, G., Lee, C.C., Huang, S.M., Wang, B., Bian, G., Zheng, H., Sanchez, D.S., Belopolski, I. and Alidoust, N., 2016. Prediction of an arc-tunable Weyl Fermion metallic state in $Mo_xW_{1-x}Te_2$. Nature communications, 7, p.10639.

[35] Ali, M.N., Xiong, J., Flynn, S., Tao, J., Gibson, Q.D., Schoop, L.M., Liang, T., Haldolaarachchige, N., Hirschberger, M., Ong, N.P. and Cava, R.J., 2014. Large, non-saturating magnetoresistance in WTe 2. Nature, 514(7521), p.205.

[36] Belinicher, V.I. and Sturman, B.I., 1980. The photogalvanic effect in media lacking a center of symmetry. Physics-Uspekhi, 23(3), pp.199-223.

[37] Ivchenko, E.L. and Ganichev, S.D., 2017. Spin-dependent photogalvanic effects (A Review). arXiv preprint arXiv:1710.09223.

[38] Ivchenko, E.L., 1978. EL Ivchenko and GE Pikus, JETP Lett. 27, 604 (1978). JETP Lett., 27, p.604.

[39] Belinicher, V.I., 1978. Space-oscillating photocurrent in crystals without symmetry center. Physics Letters A, 66(3), pp.213-214.

[40] Asnin, V.M., Bakun, A.A., Danishevskii, A.M., Ivchenko, E.L., Pikus, G.E. and Rogachev, A.A., 1978. Observation of a photo-emf that depends on the sign of the circular polarization of the light. JETP Letters, 28, pp.74-77.

[41] McIver, J.W., Hsieh, D., Steinberg, H., Jarillo-Herrero, P. and Gedik, N., 2012. Control over topological insulator photocurrents with light polarization. Nature nanotechnology, 7(2), p.96.

[42] Chan, C.K., Lindner, N.H., Refael, G. and Lee, P.A., 2017. Photocurrents in Weyl semimetals. Physical Review B, 95(4), p.041104.

[43] Ma, Q., Xu, S.Y., Chan, C.K., Zhang, C.L., Chang, G., Lin, Y., Xie, W., Palacios, T., Lin, H., Jia, S. and Lee, P.A., 2017. Direct optical detection of Weyl fermion chirality in a topological semimetal. Nature Physics, 13(9), p.842.

Chapter 2

Observation of Spatially Dispersive Circular Photogalvanic Effect in Type-II Weyl Semimetal

Reproduced in part with permission from "Ji, Z., Liu, G., Addison, Z., Liu, W., Yu, P., Gao, H., Liu, Z., Rappe, A.M., Kane, C.L., Mele, E.J. and Agarwal, R., 2018. Spatially dispersive circular photogalvanic effect in a Weyl semimetal. arXiv preprint arXiv:1802.04387."

2.1 Introduction

The unique band structure of Weyl semimetal has attracted a lot of attention in studying their electronic and transport properties [1–12]. Recently, these studies have been extended to their optical properties, especially through the measurements of nonlinear responses. Until now, most experiments were focused on the type-I Weyl semimetal, such as monopnictide TaAs, where a zero-bias photocurrent under chiral optical excitation at mid-infrared frequencies [13] has been attributed to the distinct chirality of each tilted Weyl cone, and exceedingly large values of the second order nonlinear optical susceptibility at visible frequencies were observed [14]. Some theoretical work have also been conducted to understand the mechanism of injection photocurrent under low frequency excitation at Weyl semimetal [15–19]. In this chapter, a novel circular photogalvanic effect discovered in type-II Weyl semimetal will be discussed.

$MoTe_2$, which was theoretically predicted and confirmed by experiments to be a type-II Weyl semimetal [20,21], provides a promising platform for studying the optical response in this kind of topological material. Bulk $MoTe_2$ has three different crystal phases: hexaginal 2H, monoclinic ($P2_1/m$) 1T′ Fig(2.1.a) and orthorhombic ($Pmn2_1$) T_d phase Fig(2.1.b), in which the 1T′ phase and T_d phase will be discussed in this work.

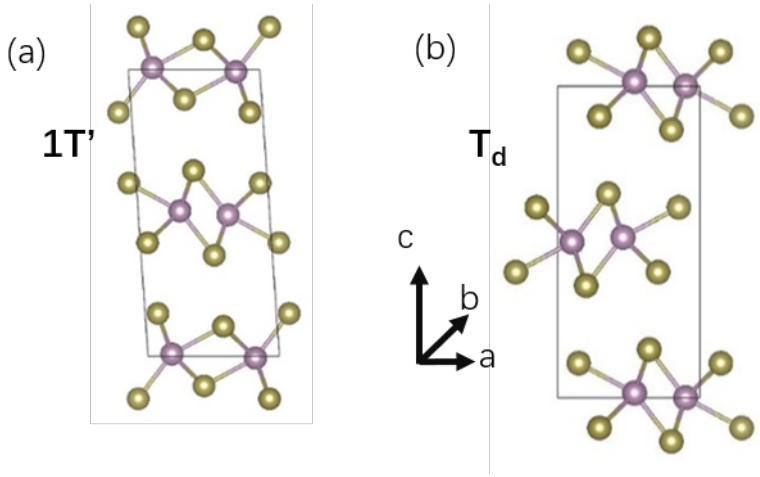

FIGURE 2.1: Crystal structures of 1T′ (a) and T_d phase of $MoTe_2$ (b). Yellow (purple) spheres represent Te (Mo) atoms.

As reported in the previous work [24, 25] on $MoTe_2$, this material shows a phase transition at about 250 K between the high temperature centrosymmetric semimetal 1T′ phase (trivial phase) and the inversion symmetry broken T_d phase (non-trivial phase). 1T′ phase and T_d phase possess both layered structures and share the same in-plane symmetry, while the atomic stacking in the c axis of these two phases are different. As shown in Fig 2.2.b, the structural phase transition is revealed by an abrupt change in the temperature-dependent resistivity, which occurs at about 260 K upon warming and around 250 K upon cooling. By comparing the Raman spectra in Fig 2.2.c, two new peaks labeled by A and D only show in low temperature phase, which strongly indicates the existence of phase transition.

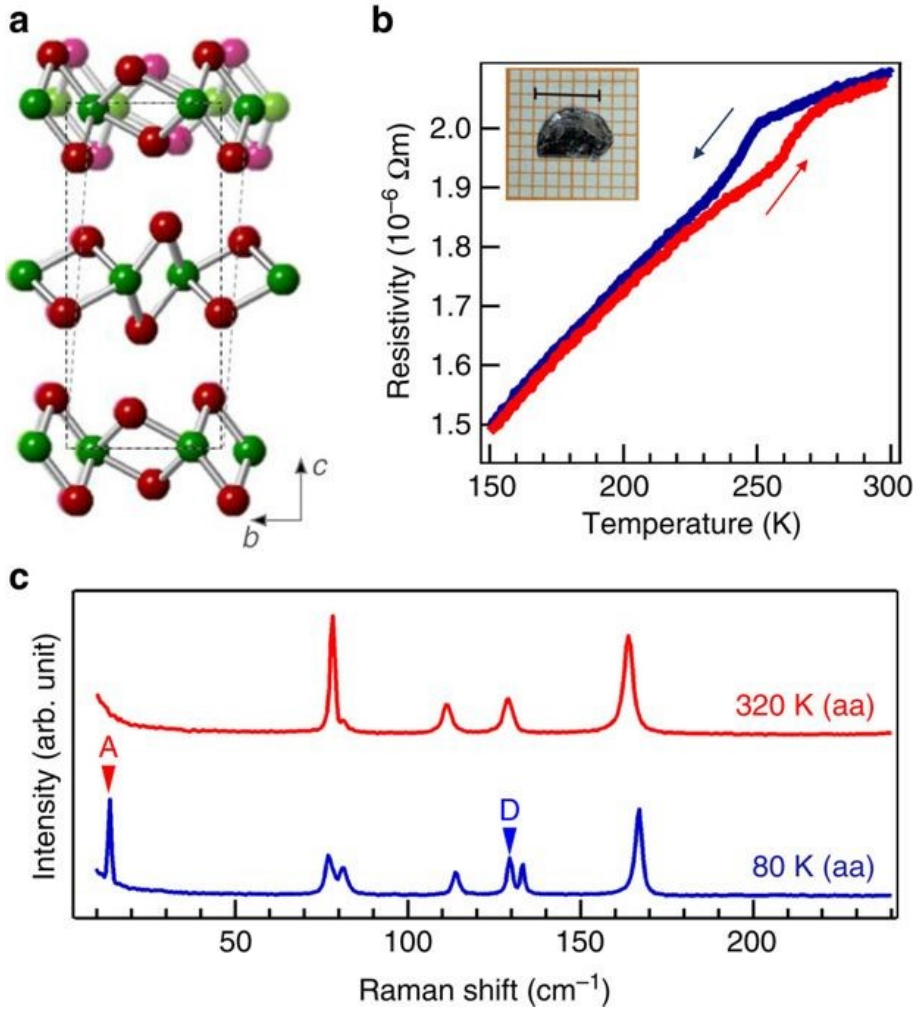

FIGURE 2.2: (a) Crystal structures of 1T′ (shadow) and T_d (solid) phases. (b) Resistivity measurement shows a temperature-induced phase transition. The inset shows a photograph of the high-quality single crystal; scale bar, 5 mm. (c) Raman spectra at 320 and 80 K. The letters inside the parenthesis indicate the polarization directions for incident and scattering lights. Reprinted figure with permission from [24]

Following the discovery of $MoTe_2$ as an inversion symmetry broken type-II Weyl semimetal below 250 K, $Mo_xW_{1-x}Te_2$ has also been demonstrated as room temperature type-II Weyl semimetal similar to the structure of $MoTe_2$. [22, 23] The band structure of different tungsten doping concentration in $MoTe_2$ was studied via ARPES [26], which shows that the Fermi arc becomes shorter with higher tungsten doping and disappears when x<0.07. [Fig(2.3)] Novel ab initio calculations were performed to pinpoint the

topological phase transition and the results agreed well with the experimental observation, indicating that the topological phase transition can also be induced by composition doping. This phase change property of $MoWTe_2$ family made it possible to compare two phases and study the unique response of the inversion broken Weyl phase.

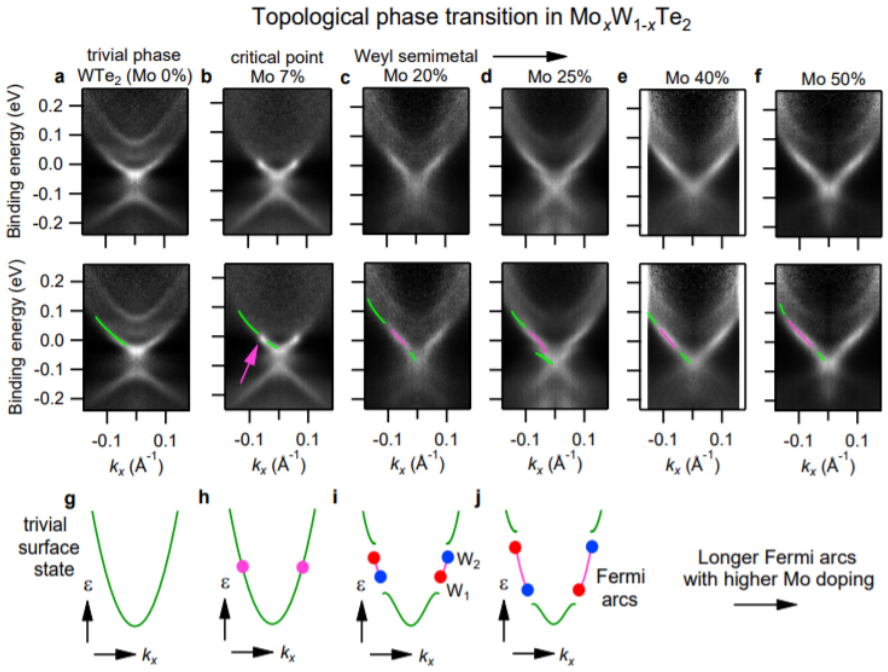

FIGURE 2.3: (a-f) As the bands invert, they first touch at a point (b). This point can be viewed as a band crossing consisting of two chiral charges on top of each other in momentum space (purple dot). Upon further inversion, the chiral charges separate, giving a Weyl semimetal (c-f). (g-j) Schematic of the configuration of Weyl points. With higher Mo doping, the band crossing occurs and the Fermi arcs become longer. Reprinted figure with permission from [26]

2.2 Experimental Setup

2.2.1 Sample preparation and characterization

Large, well-formed, ribbon-like single crystals of $MoTe_2$ and $Mo_xW_{1-x}Te_2$ (x=0.3 and 0.9) alloy were grown and provided by Zheng Liu's gorup. The phase and the quality of the $Mo_{0.9}W_{0.1}Te_2$ were confirmed through Transmission Electron Microscope

FIGURE 2.4: $Mo_{0.9}W_{0.1}Te_2$ diffraction pattern under TEM

(TEM). Bulked $Mo_{0.9}W_{0.1}Te_2$ was exfoliated by scotch tape for several times and then the tape was put into acetone. The acetone was heated and sonicated for 2 hours. TEM carbon grid was used to scoop in the acetone to transfer the $Mo_{0.9}W_{0.1}Te_2$ onto the grid. [Fig(2.4)] The diffraction pattern of the material shows single-crystallinity of the sample. The zone axis was the crystallographic c axis.

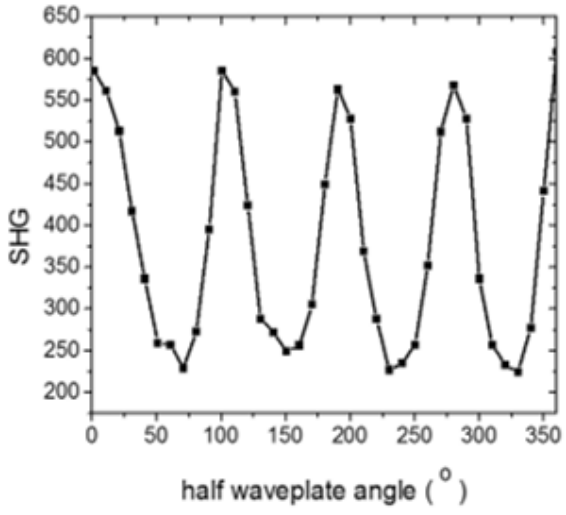

FIGURE 2.5: SHG data is collected at each half wave plate angle. At each angle, the data is collected for 30 seconds. The half wave plate is rotated from 0 to 360° and SHG is plotted as function of half wave plate angle.

Optical second harmonic generation (SHG) was also utilized to check the crystal structure. Focused beam at wavelength 950 nm was performed to generate SHG and

scanned on the sample surface. A half wave plate was placed in the optical path to control the linear polarization. (Fig 2.5) SHG signal did not show spatial dependence and four periods were obtained while rotating the half wave plate from 0 to 360°. The result satisfied the surface symmetry of $Mo_{0.9}W_{0.1}Te_2$, suggesting high quality samples.

Bulked $Mo_{0.9}W_{0.1}Te_2$ was exfoliated by scotch tape and transferred onto Si/SiO_2 substrate. The thickness of the sample was about 100nm and the dimesion was about 10um $\times$ 10 um. Two parallel contacts were patterned on AutoCAD and written by E-beam resist (PMMA) spin coating and electron beam lithography exposure. The electrodes were made by 100 nm Ti layer and 50 nm Au layer through physical vapor deposition.

2.2.2 Optoelectronic Measurement Setup

The excitation source was provided from a wavelength tunable Ti-Sapphire pulsed laser in the 680-1080 nm. The laser was focused to a near perfect Gaussian spot by a 60X objective and the full width at half maximum (FWHM) of the spot was controlled in the range of $\sim$2-20 um FWHM, with total power on the sample stage in the 1-15 mW range. The laser wavelength performed in this work was chosen to be 750 nm, and the beam size was $\sim$ 2 um. The light was polarized via a polarizer and the extinction ratio of linearly polarized light was ensured to be larger than 1000:1 before measurements.

Quarter wave plate (QWP) mounted on a motorized precision rotation stage driven by a servo motor (Thorlabs) was used to vary the angle continuously from 0-360° to obtain different laser polarizations (from linear polarization to circular polarization). The laser polarization on the sample plane was also monitored carefully to ensure accuracy. By rotating the quarter waveplate, it can change the linear polarized incident light to different light helicity output. If the angle between the fast axis of the quarter wave plate and the linear polarization direction was defined as ϕ, the polarization of the output light was linear polarization when ϕ = 0°, 90°, 180° and 270°; when ϕ= 45° and 225°, it was left circular polarization; when ϕ= 135° and 315°, it was right circular polarization.

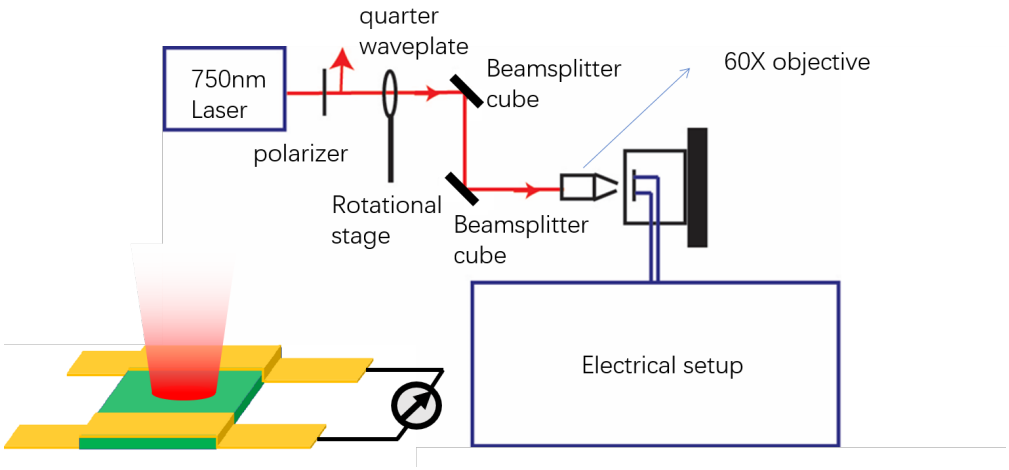

FIGURE 2.6: Experimental setup for photocurrent measurements. The light polarization is controlled by a polarizer and a quarter waveplate. Focused by a 60X lens, the beam is normal incident on the sample plane. The sample has two parallel electrodes which are connected to the electrical setup to collect photocurrent.

The experimental setup is shown as Fig 2.6. The light polarization controlled by the polarizer and quarter waveplate has been checked via the experiments mentioned above. Guided by two beamsplitter cubes, the beam was focused to 2-3 um diameter through a 60X lens and normal incident onto the sample stage. The light incident direction was aligned to the c axis of the $MoWTe_2$ crystal structure (Fig 2.1). When scanning the light beam over the sample using piezoelectric stages, the spatial coordinates were recorded with an accuracy of $\sim$200 nm. Photocurrents were recorded using a current preamplifier (DL instruments model 1211) for which the bias voltage was sourced and the output signal from the preamplifier (photocurrent was converted to an amplified voltage signal) was recorded continuously ($\sim$10 data points per second) by the PCI card (National Instrument, NI PCI-6281). The time constant of the preamplifier was chosen in the range of 100-300 ms. The quarter wave plate was rotated at the rate of 7°/sec using a motorized precision rotation stage with a servomotor.

The zero bias photocurrents were measured under different light power by adjusting the optical density filter. Incident light intensity was obtained by power meter and the photocurrent was plotted as the function of light intensity. Shown in the Fig 2.7, the photocurrent scaled linearly with laser power and all measurements in this work were

performed within this power regime.

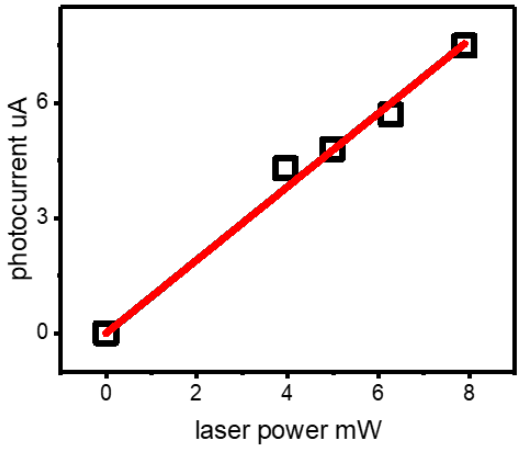

FIGURE 2.7: Photocurrents at light power = 0 mW, 3.95 mW, 4.98 mW, 6.27 mW and 7.89 mW are extracted and plotted as function of light intensity, shown as the black squares. The red line is linear fitting of the data.

2.3 Experimental Results

2.3.1 Observation of PGE in $Mo_{0.9}W_{0.1}Te_2$

As mentioned in the experimental setup, the light polarization was controlled by the quarter waveplate. For CPGE current, the response was dependent on the light helicity, meaning that the current measured at right circular polarization should be different from the current at left circular polarization. Therefore, the CPGE current, J_C should be periodical if the quarter wave plate is continuously rotating and the period is 180°. CPGE current can be expressed as $J_C(\phi) = J_C sin(2\phi)$.

Photocurrents were collected while the quarter wave plate was rotated for a circle and plotted as function of the angle ϕ shown in Fig 2.8. Obviously, the photocurrent under right circular polarization light (ϕ= 135° and 315°) was smaller than the photocurrent under left circulat polarization light (ϕ= 45° and 225°) and period was 180°. However, the photocurrent data was not a sine function as the pure CPGE current J_C,

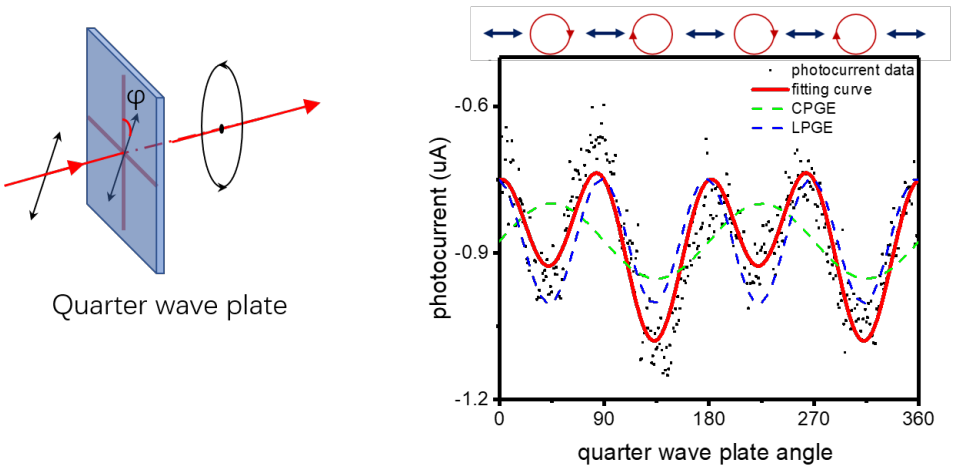

FIGURE 2.8: (left) Polarization controlled by quarter waveplate. (right) Black dots are the photocurrent data plotted as the function of quarter waveplate angle. The polarizatoin of light is marked above for each angle. The red line is the fitting curve for the total photocurrent. The green line and the blue line are the CPGE and LPGE current component respectively.

indicating another polarization dependent contribution. Thus, linear photogalvanic effect (LPGE) was considered in this experiment.

For LPGE, the photocurrent can be modified by the linear polarization, but is not sensitive to the handedness of circularly polarized light. Therefore, the photocurrent amplitude for LPGE, J_L, at ϕ = 0°, 90°, 180° and 270° (linear polarization) should be different from the photocurrent amplitude at ϕ= 45°, ϕ= 135°, 225° and 315° (circular polarization). The period for LPGE current should be 90° and LPGE current can be written as $J_L(\phi) = J_L sin(4\phi + \phi_0)$.

Considering both CPGE and LPGE, the total photocurrent can be fitted into the equation:

$$J = J_C sin(2\phi) + J_L sin(4\phi + \phi_0) + J_0 \tag{2.1}$$

where, J_C is the magnitude of the CPGE, $J_L$is the magnitude of the linear photogalvanic effect (LPGE) with a phase shift ϕ_0. J_0 is the polarization-independent background current which could be thermocurrent or Dember effect due to the heat gradients induced by asymmetric illumination on the sample. The fitting curve is shown as red line in Fig 2.8. CPGE current $J_C = 77nA$ and LPGE current $J_L = 127nA$. These two contributions

are plotted in green line and blue line respectively.

Therefore, CPGE and LPGE currents were both observed in the type-II Weyl semimetal $Mo_{0.9}W_{0.1}Te_2$. Before studying the photogalvanic effect, we needed to excluded some factors that could influence the measurements, such as the edge effect [32], polarization independent photocurrent and external field.

Edge effect could be observed by measuring the photocurrent when beam spot was close to edges and far from the edges. To minimize the influence of thermocurrent, the beam was scanning in the middle of two electrodes from left edge to right edge in a consistent speed as shown in Fig 2.9. The spatial dependent photocurrent was collected. Initially, the photocurrent was zero, implying that the beam was out of the sample. Once the beam arrived at the edge of the sample, the photocurrent showed up and gradually increased in negative direction. After reaching maximum value, the photocurrent magnitude started to decrease and become zero at certain location. Then, it flipped to positive direction and reached maximum. The current became zero when the beam moved out of the right edge. The photocurrent showed a significant spatial dependence. This property was confirmed to be repeatable by measurements on different samples.

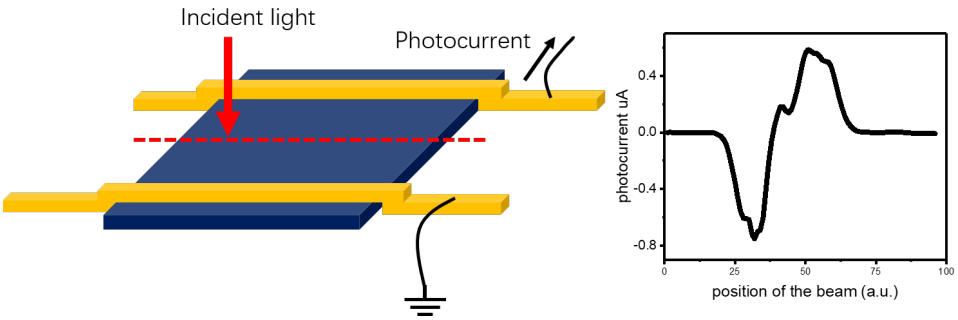

FIGURE 2.9: (left) two parallel electrodes are patterned on the top and bottom of the sample to collect photocurrent. The beam is scanning from left to right side in the middel of two electrodes indicated by red dash line. (right) Photocurrents are collected when the beam is scanning in a constant speed and plotted as function of beam location

The spatial dependent photocurrent measurement indicated that the edge effect existed in the photocurrent measurements. To exclude edge effect, $Mo_{0.9}W_{0.1}Te_2$ was exfoliated to size larger than $20um \times 20um$ and the beam was focused inside the sample to avoid touching edge.

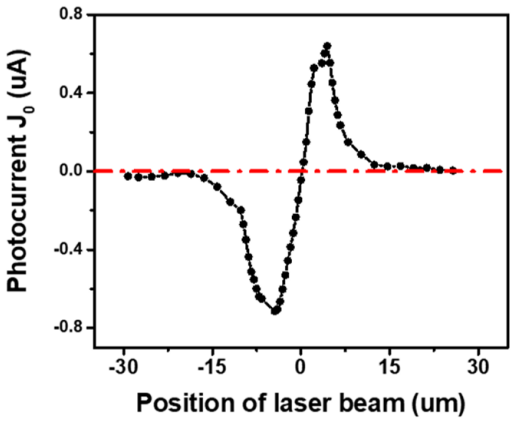

FIGURE 2.10: Polarization independent photocurrent, J_0 (black dotted line), as a function of the laser spot location, from A to B, scanned along the line connecting the two electrodes. The position where J_0 equals to zero, is approximately at the center of the two electrodes, and its two extremes occur at the ends of the electrodes. Inset shows the device geometry.

In the measurement of Fig 2.8, there was a polarization independent contribution. To confirm the origin of this term, beam was scanned from one electrode to the other with fix polarization. The photocurrent J_0 reached maximum value with opposite sign at the ends of the electrodes and vanish near the mid-point (Fig 2.10), implying that it was mostly a result of the Dember effect due to the heat gradients induced by asymmetric illumination on the sample. [28] Since J_0 did not affect polarization dependent currents J_C and J_L, it will not be discussed in this work.

Another factor which could affect the PGE measurement was the external electric field. Therefore, photocurrent was measured at a fix beam spot while applying various external field. At each external field, photocurrent was collected while rotating the quarter wave plate and plotted as function of rotation angle. Eqn 2.1 was used to fit the data and PGE current J_C was obtained. In all these conditions, CPGE and LPGE were observed, and the amplitude of CPGE J_C is 59 nA and LPGE J_L is 90.8 nA consistently,

suggesting a bias voltage independent behavior. Thus, this photogalvanic effect is not caused by external voltage.

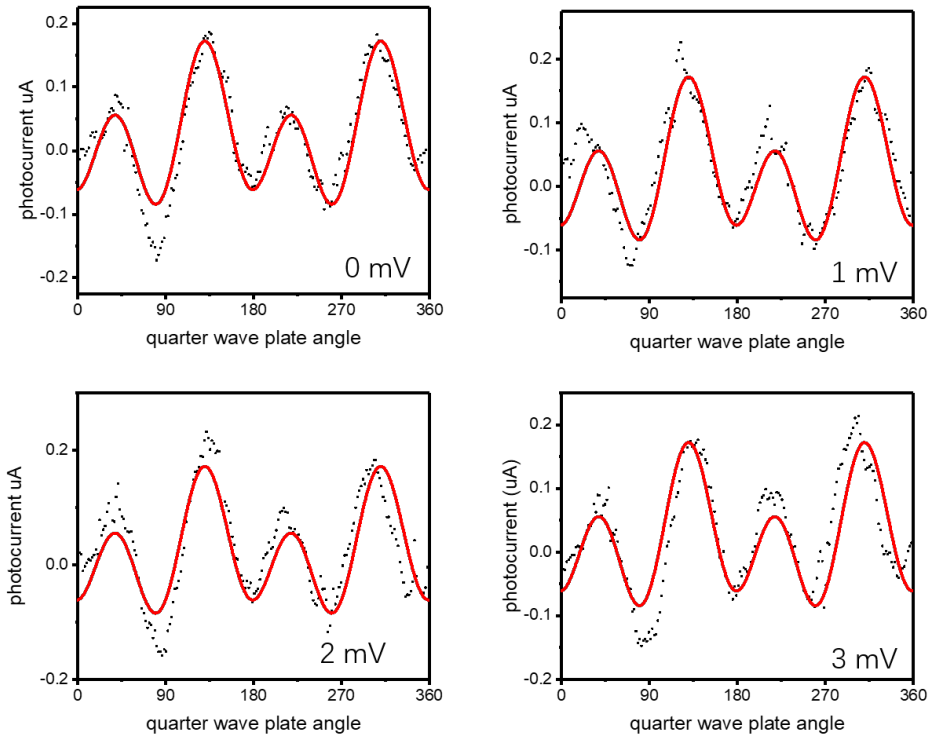

FIGURE 2.11: Photocurrents are collected while rotating the quarter waveplate for a circle and plotted as function of rotating angle when external bias voltage is applied. The measurements are repeated when the bias voltage is 0 mV, 1 mV, 2 mV and 3 mV. The black dots are the experimental data and the red line is fitting curve using Eqn 2.1.

2.3.2 Spatially dispersive CPGE in $MoWTe_2$

After the influence of edge effect, thermocurrent and external electric field was excluded, can we still observe CPGE and LPGE on Weyl semimetal $Mo_{0.9}W_{0.1}Te_2$ under normally incident light? PGE measurement was performed on a $Mo_{0.9}W_{0.1}Te_2$ flake. Both CPGE and LPGE current were observed when the beam spot was off-center of the sample without touching sample edges. Spot a was defined as the beam spot at left side of the sample and the spot b was the right side. As given in Fig 2.12, photocurrent at two spots was measured and plotted as quarter wave plate rotattion angle.

Shapes of these two photocurrents were flipped. By fitting the data into the Eqn 2.1, the contribution from CPGE and LPGE can be extracted. At spot a, the CPGE current $J_C = 36nA$ and LPGE current $J_L = -100nA$; at spot b, the CPGE current $J_C = -43nA$ and LPGE current $J_L = 63nA$. The CPGE currents at two spots had similar amplitude but different sign. In other words, if same circularly polarized light is incident on these two spots, the CPGE currents flow in different directions suggesting spatial dependent totoal photocurrent as well as CPGE.

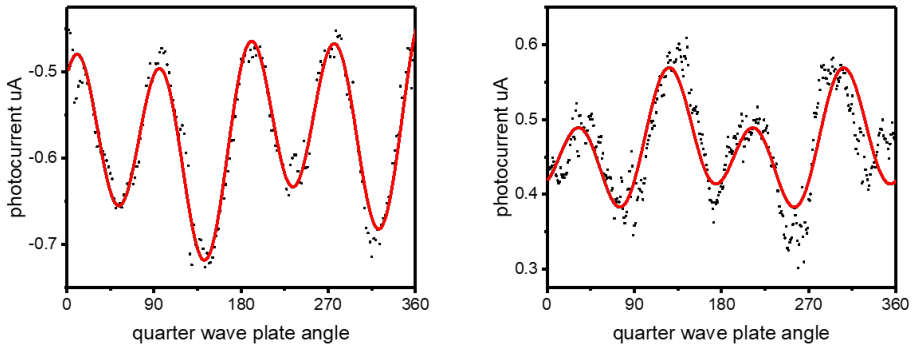

FIGURE 2.12: Photocurrent plotted as a function of quarter wave plate fast axis rotation angle ϕ at the location at spot a(left) and spot b (right). Black dots are the experimental data and red solid lines are the fits to Eqn 2.1.

A question was raised that wheth·er this CPGE exclusively existed in $Mo_{0.9}W_{0.1}Te_2$ or can be observed in other materials. Thus, $MoTe_2$ was utilized to repeat the PGE experiments on $Mo_{0.9}W_{0.1}Te_2$. Even though the $MoTe_2$ is not Weyl semimetal at room temperature, it shares the same in-plane surface crystal structure as $Mo_{0.9}W_{0.1}Te_2$. Photocurrent was measured at the off-center position on the $MoTe_2$ at room temperature and the results were in the Fig 2.13.

LPGE was clearly observed at two positions and the LPGE current direction flipped. However, the photocurrent at right circular polarization and the photocurrent at left circular polarization had similar values at both spots, suggesting that the CPGE was not obvious in room temperature $MoTe_2$. Comparing with the CPGE behaviour in $Mo_{0.9}W_{0.1}Te_2$, it is likely that this spatially dependent CPGE has different behaviours in different materials.

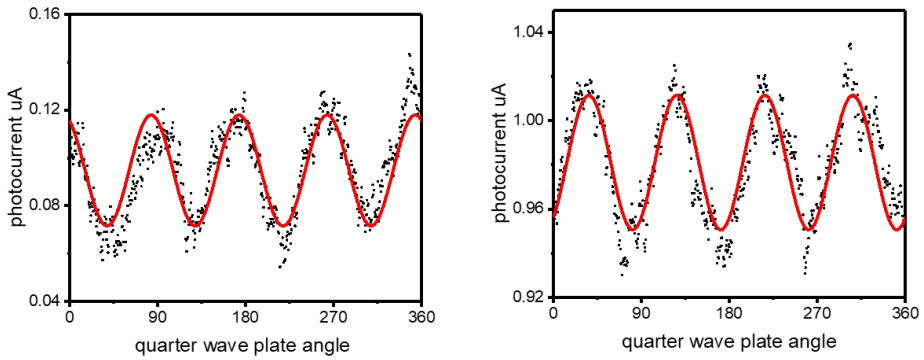

FIGURE 2.13: Photocurrents are collected on room temperature $MoTe_2$ while rotating the quarter waveplate for a circle and plotted as function of rotating angle. The location of the beam is when the current reaches negative maximum (left) and positive maximum (right). The black dots are the experimental data and the red line is fitting curve using Eqn 2.1

The difference between $MoTe_2$ and $Mo_{0.9}W_{0.1}Te_2$ is that $Mo_{0.9}W_{0.1}Te_2$ is inversion symmetry breaking via W doping in $MoTe_2$ and becomes Weyl semimetal. As mentioned before, $MoTe_2$ has another topological phase transition method, similar to the composition doping, that is the temperature induced phase change. At the temperature lower than 250 K, 1T' phase $MoTe_2$ will be changed to T_d phase inversion symmetry breaking Weyl semimetal, the phase of room temperature $Mo_{0.9}W_{0.1}Te_2$. Thus, spatial dependent CPGE measurements were performed at low temperature $MoTe_2$.

The sample was placed in a cryostat and connected with a turbo pump. The pressure was maintained to be lower than 10^{-6} Torr. The temperature was monitored by a thermocouple in the chamber and was controlled by the balance between liquid nitrogen and heating plate. In this experiment, the heating plate was close and the temperature reached 77k after 30-min cooling to make sure that the $MoTe_2$ was in the Weyl phase.

As shown in Fig 2.14, pholarization dependent photocurrents were measured at four locations: spot a and spot d were off-center position at left and right side, spot b and spot c were near the center. Clearly, at off-center positions, photocurrent at right circular polarization was different from left circular polarization, implying significant

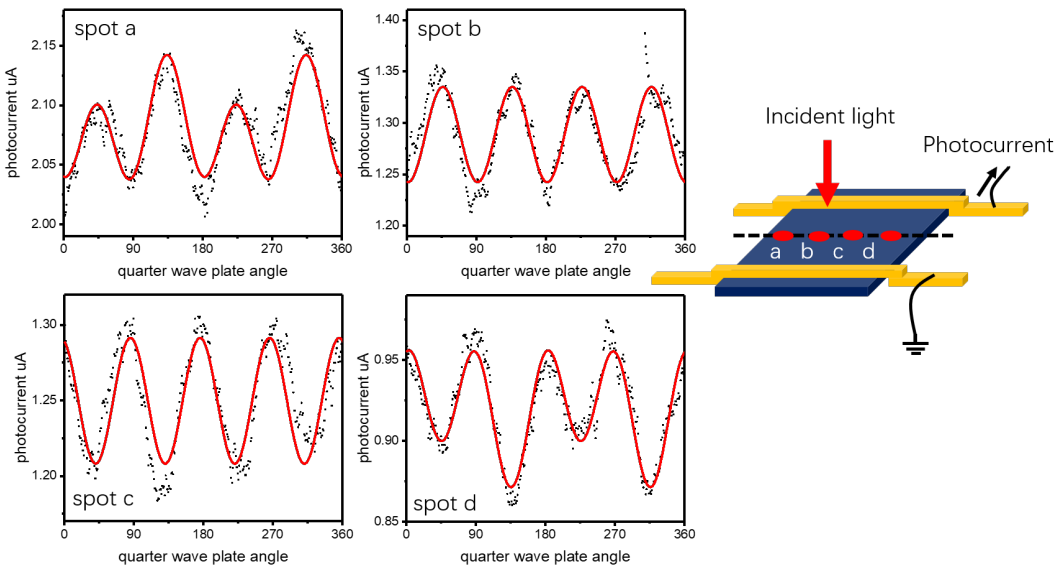

FIGURE 2.14: Photocurrents are collected at 77 K $MoTe_2$ while rotating the quarter wave plate for a circle and plotted as function of rotating angle. Four locations are selected to measure CPGE data: from left to right is spot a to d (shown in schematic figure). Photocurrent is plotted as function of quarter waveplate angle at all four positions as labeled in the figure. The black dots are the experimental data and the red line is fitting curve using Eqn 2.1

CPGE current. By fitting the data into Eqn 2.1, contribution from each component was be extracted. For spot a, CPGE current $J_C = 20.82nA$ and LPGE current $J_L = -40.57nA$; while at spot d, CPGE current $J_C = -14.26nA$ and LPGE current $J_L = 34.63nA$. Similar to the results observed in $Mo_{0.9}W_{0.1}Te_2$, the CPGE and LPGE when beam was off-center had comparable amplitude but opposite sign. When beam was close to the center, the photocurrents at spot b and spot b were almost the same at both circular polarized light, indicating that the CPGE current was negligible. Therefore, the spatial dependent CPGE can only be observed in inversion symmetry breaking Weyl phase $MoTe_2$ and $Mo_{0.9}W0.1Te_2$, but not in trivial phase $MoTe_2$.

In order to further confirm the observation above, the same $MoTe_2$ sample was heated up again to high temperature 1T' phase. The stage was heated to 360 K and maintained for 30 min before measurements, to avoid the phase lock and guarantee

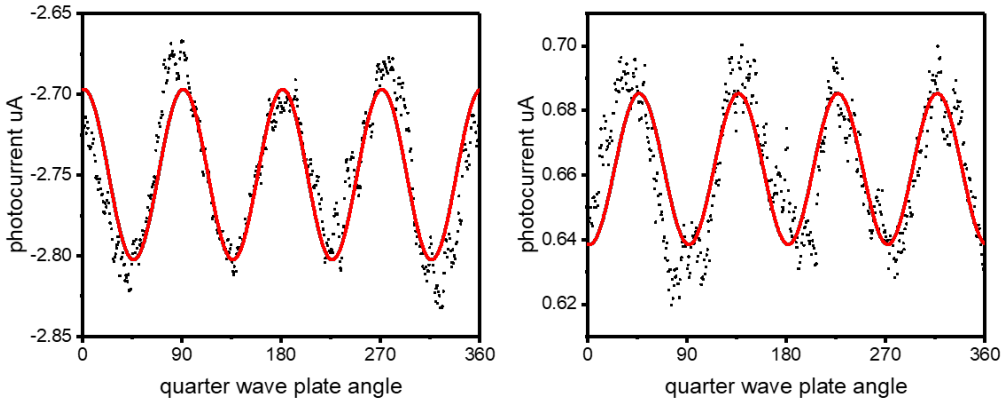

FIGURE 2.15: Photocurrents are collected after tempertaure back to 360 K on the same $MoTe_2$ sample at left side (left) and right side (right). Photocurrent is plotted as function of quarter waveplate angle. The black dots are the experimental data and the red line is fitting curve using Eqn 2.1

that the sample was completely phase changed to high temperature phase. Same experiments were performed on the sample and the results were shown in Fig 2.15. For both left and right sides of the sample, the photocurrents were the same under all of the circular polarization light, meaning that the CPGE current disappeared when the temperature increased back to room temperature. The sample showed the same property as before in Fig 2.13. Therefore, the spatially dispersive CPGE current can only be observed in the low temperature Weyl phase and this experiment was repeatable after phase transition back and forth.

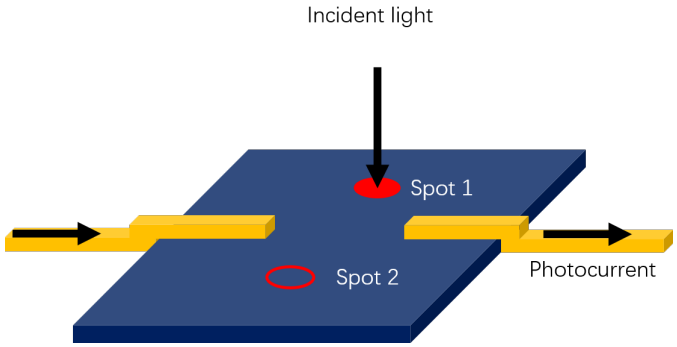

FIGURE 2.16: New device design to confirm spatially dispersive CPGE

To further confirm the observation of spatially dispersive CPGE, measurements

were repeated for many times on different $MoTe_2$ and $Mo_{0.9}W_{0.1}Te_2$ flakes. The geometry of eclectic contacts were also changed to different design. The results were all the same as shown above. For example, vertical line contacts pattern instead of two long parallel electrodes shown as Fig 2.16 were used for photocurrent measurements. Spot 1 and spot 2 marked on the figure were two sides of the sample and photocurrent were measured at these two spots.

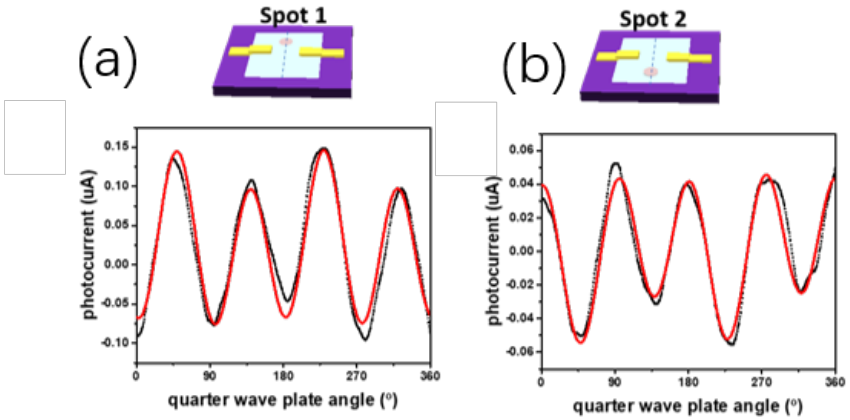

FIGURE 2.17: (a) and (b) Total photocurrent measured at the two sides of the electrodes (a) spot 1 and (b) spot 2 and plotted as quarter wavep plate angle. Black dots are the experiment data and red solid lines are the fitted curves for total photocurrent (Eqn(2.1)).

On $Mo_{0.9}W_{0.1}Te_2$ flake at room temperature, the results were the same as before in $Mo_{0.9}W_{0.1}Te_2$.]Fig 2.17 Both CPGE and LPGE contribution were significant and the direction of these currents had opposite direction at two spots. Same results were observed by repeating this experiment on another composition $Mo_{0.3}W_{0.7}Te_2$, which is also room temperature Weyl semimetal. These repeatable results strongly proved that the spatially dispersive CPGE occurred in Weyl phase.

This electrode design was used for PGE current measurements on $MoTe_2$ at 300 K and 77 K. The process of experiments were similar as before. The sample was placed in the temperature controlled cryostat and the dependence of photocurrent and quarter wave plate angle was measured at spot 1 and spot 2 at room temperature. Then, phase transition was achieved by cooling the sample to 77 k for more than 30 min and the

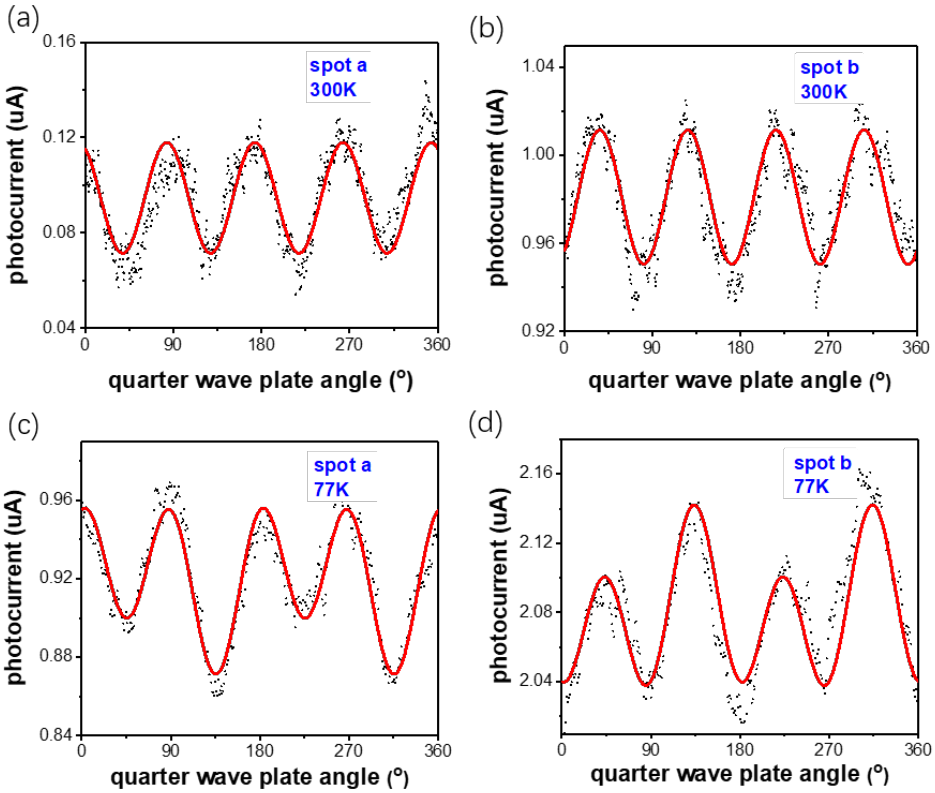

FIGURE 2.18: Photocurrents plot as the function as quarter waveplate rotation angle under different experiment condition: (a) spot a at 300 K; (b) spot b at 300 K; (c) spot a at 77 K; (d) spot b at 77 K. Black dots are the experiment data and the red solid line is the fitting curve.

photocurrent was collected at the same spot 1 and spot 2. All the data was fitted into the Eqn 2.1 to get the contribution from CPGE and LPGE. The results were listed in the table 2.1.

$MoTe_2$	spot 1		spot 2	
	J_L(nA)	J_C(nA)	J_L(nA)	J_C(nA)
300 K(1T′)	23	∼0	-30	∼0
77 K(T_d)	34	14	-40	-21

TABLE 2.1: Fitting parameters for polarization dependent photocurrent data measured on $MoTe_2$ at two different spatial locations (spot 1 and spot 2) at 77K and 300K. J_L and J_C are the LPGE and CPGE components, respectively.

Similar to the experimental results above on $MoTe_2$, (Fig 2.13 and 2.14) only LPGE current can be measured at room temperature phase (1T′); while at 77 k, 14 nA and -21

nA CPGE currents were obtained at spot 1 and spot 2 respectively. Repeated successfully, this experiment provided a strong evidence that the CPGE current only exists in the inversion broken T_d phase.

2.4 Conclusion

In conclusion, the photocurrent which is sensitive to the light polarization is observed in the type-II Weyl semimetal $MoWTe_2$. This photocurrent has both CPGE and LPGE contribution; the former component is different under right and left circular polarization light, while the latter one is controlled by the linear polarization direction. More interestingly, the CPGE current and LPGE current have significant spatial dependence; current direction is opposite when the beam is focused on different side of the sample. This experiment is repeatable and the current is giant ($\sim 10^2 nA$ under $\sim 1mW$ laser power), indicating a very robust effect.

Additionally, this spatial dependent CPGE in proven to only exist in the inversion symmetry breaking Weyl phase by the experiment on topological phase transition material $MoTe_2$. Even though the room temperature phase and low temperature phase share the same in-plane structure and only different in the stacking pattern, the spatial dependent CPGE current can only be observed at low temperature, suggesting a special effect in the type-II weyl semimetal. By further studying the mechanism of this effect, we can have a better understanding of the nature of type-II Weyl semimetal.

To distinguish from conventional CPGE due to the unique property, this novel CPGE is defined as spatial disperse CPGE (sCPGE). Even though the CPGE current is confirmed to be spatial dependent and exist in certain phase, the actual current distribution is still unclear and the reason why this effect disappears at the other phase needs to be revealed. Furthermore, from symmetry considerations, in both the T_d (C_{2v}) and 1T' phases (C_{2h}), under normally incident light on the $\hat{x} - \hat{y}$ plane (propagation direction, $\hat{z}$), any in-plane second order optical response such as PGE [29,30] or photon drag effect [31] is forbidden by the two-fold rotation symmetry. Thus, J_C and J_L should

both vanish in this material, which is contrary to our measurements. Therefore, the observations of position-dependent LPGE in the 1T′ and T_d phases as well as CPGE only in the T_d phase indicate an unconventional origin of the PGE effects.

Therefore, in the following chapter, more experiments will be designed to study the property of sCPGE. By analyzing these properties of sCPGE, we will try to build up a model to discuss the mechanism of sCPGE in the Weyl semimetal.

Bibliography

[1] Kane C. L., Mele E. J.; Z 2 topological order and the quantum spin Hall effect; Physical review letters 95 (14), 146802 (2005).

[2] Hasan M. Z., Kane C. L.; Colloquium: topological insulators; Reviews of Modern Physics 82 (4), 3045 (2010).

[3] Qi X.-L., Zhang S.-C.; Topological insulators and superconductors; Reviews of Modern Physics 83 (4), 1057 (2011).

[4] Wan X., Turner A. M., Vishwanath A., Savrasov S. Y.; Topological semimetal and Fermi-arc surface states in the electronic structure of pyrochlore iridates; Physical Review B 83 (20), 205101 (2011).

[5] Armitage N., Mele E., Vishwanath A.; Weyl and Dirac semimetals in three-dimensional solids; Reviews of Modern Physics 90 (1), 015001 (2018).

[6] Soluyanov A. A., Gresch D., Wang Z., Wu Q., Troyer M., Dai X., Bernevig B. A.; Type-II weyl semimetals; Nature 527 (7579), 495 (2015).

[7] Burkov A., Balents L.; Weyl semimetal in a topological insulator multilayer; Physical Review Letters 107 (12), 127205 (2011).

[8] Nielsen H. B., Ninomiya M.; The Adler-Bell-Jackiw anomaly and Weyl fermions in a crystal; Physics Letters B 130 (6), 389-396 (1983).

[9] Zyuzin A., Burkov A.; Topological response in Weyl semimetals and the chiral anomaly; Physical Review B 86 (11), 115133 (2012).

[10] Potter A., Kimchi I., Vishwanath A.; Quantum oscillations from surface Fermi arcs in Weyl and Dirac semimetals; Nature communications 5, 5161 (2014).

[11] Hosur P., Qi X.; Recent developments in transport phenomena in Weyl semimetals; Comptes Rendus Physique 14 (9), 857-870 (2013).

[12] Xiong J., Kushwaha S. K., Liang T., Krizan J. W., Hirschberger M., Wang W., Cava R., Ong N.; Evidence for the chiral anomaly in the Dirac semimetal Na3Bi; Science 350 (6259), 413-416 (2015).

[13] Ma Q., Xu S.-Y., Chan C.-K., Zhang C.-L., Chang G., Lin Y., Xie W., Palacios T., Lin H., Jia S.; Direct optical detection of Weyl fermion chirality in a topological semimetal; Nature Physics, (2017).

[14] Wu L., Patankar S., Morimoto T., Nair N. L., Thewalt E., Little A., Analytis J. G., Moore J. E., Orenstein J.; Giant anisotropic nonlinear optical response in transition metal monopnictide Weyl semimetals; Nature Physics 13 (4), 350 (2017).

[15] de Juan F., Grushin A. G., Morimoto T., Moore J. E.; Quantized circular photogalvanic effect in Weyl semimetals; arXiv preprint arXiv:1611.05887, (2016).

[16] Morimoto T., Zhong S., Orenstein J., Moore J. E.; Semiclassical theory of nonlinear magneto-optical responses with applications to topological Dirac/Weyl semimetals; Physical Review B 94 (24), 245121 (2016).

[17] Chan C.-K., Lindner N. H., Refael G., Lee P. A.; Photocurrents in Weyl semimetals; Physical Review B 95 (4), 041104 (2017).

[18] König E., Xie H.-Y., Pesin D., Levchenko A.; Photogalvanic effect in Weyl semimetals; Physical Review B 96 (7), 075123 (2017).

[19] Zhang Y., Sun Y., Yan B.; Berry curvature dipole in Weyl semimetal materials: An ab initio study; Physical Review B 97 (4), 041101 (2018).

[20] Wang Z., Gresch D., Soluyanov A. A., Xie W., Kushwaha S., Dai X., Troyer M., Cava R. J., Bernevig B. A.; MoTe 2: a type-II Weyl topological metal; Physical review letters 117 (5), 056805 (2016).

[21] Kaminski A.; Spectroscopic evidence for a type II Weyl semimetallic state in MoTe2, (2016).

[22] Belopolski I., Sanchez D. S., Ishida Y., Pan X., Yu P., Xu S.Y., Chang G., Chang T.R., Zheng H., Alidoust N.; Discovery of a new type of topological Weyl fermion semimetal state in $Mo_xW_{1-x}Te_2$; Nature communications 7, (2016).

[23] Chang T.-R., Xu S.-Y., Chang G., Lee C.-C., Huang S.-M., Wang B., Bian G., Zheng H., Sanchez D. S., Belopolski I.; Prediction of an arc-tunable Weyl Fermion metallic state in $Mo_xW_{1-x}Te_2$; Nature communications 7, 10639 (2016).

[24] Zhang K., Bao C., Gu Q., Ren X., Zhang H., Deng K., Wu Y., Li Y., Feng J., Zhou S.; Raman signatures of inversion symmetry breaking and structural phase transition in type-II Weyl semimetal MoTe2; Nature communications 7, (2016).

[25] Deng K., Wan G., Deng P., Zhang K., Ding S., Wang E., Yan M., Huang H., Zhang H., Xu Z.; Experimental observation of topological Fermi arcs in type-II Weyl semimetal MoTe2; Nature Physics 12 (12), 1105-1110 (2016).

[26] Belopolski I., Sanchez D. S., Ishida Y., Yu P., Zhang S. S., Chang T.-R., Chang G., Pan X., Lu H., Zheng H.; Topological Weyl phase transition in Mo $_x$ W $_{1-x}$ Te $_2$; arXiv preprint arXiv:1612.07793, (2016).

[27] Dhara S., Mele E. J., Agarwal R.; Voltage-tunable circular photogalvanic effect in silicon nanowires; Science 349 (6249), 726-729 (2015).

[28] McIver J., Hsieh D., Steinberg H., Jarillo-Herrero P., Gedik N.; Control over topological insulator photocurrents with light polarization; Nature nanotechnology 7 (2), 96 (2012).

[29] Ivchenko E., Ganichev S. Spin Physics in Semiconductors. Springer; 2008.

[30] Ganichev S. D., Prettl W.; Spin photocurrents in quantum wells; Journal of physics: Condensed matter 15 (20), R935 (2003).

[31] Shalygin V., Moldavskaya M., Danilov S., Farbshtein I., Golub L.; Circular photon drag effect in bulk tellurium; Physical Review B 93 (4), 045207 (2016).

[32] Karch J., Drexler C., Olbrich P., Fehrenbacher M., Hirmer M., Glazov M., Tarasenko S., Ivchenko E., Birkner B., Eroms J.; Terahertz radiation driven chiral edge currents in graphene; Physical Review Letters 107 (27), 276601 (2011).

[33] He X., Shen B., Chen Y., Zhang Q., Han K., Yin C., Tang N., Xu F., Tang C., Yang Z.; Anomalous photogalvanic effect of circularly polarized light incident on the two-dimensional electron gas in $Al_xGa_{1-x}N/GaN$ heterostructures at room temperature; Physical review letters 101 (14), 147402 (2008).

Chapter 3

sCPGE properties and mechanism

Reproduced in part with permission from "Ji, Z., Liu, G., Addison, Z., Liu, W., Yu, P., Gao, H., Liu, Z., Rappe, A.M., Kane, C.L., Mele, E.J. and Agarwal, R., 2018. Spatially dispersive circular photogalvanic effect in a Weyl semimetal. arXiv preprint arXiv:1802.04387."

3.1 Introduction

As discussed in Chapter 2, a strong spatial dependent CPGE current was observed in Weyl phase $MoWTe_2$ family. This CPGE only occured in Weyl phase by experiments perform on phase transition $MoTe_2$, which excluded the influce of edge effect as well. Besides, conventional CPGE current should be forbidden under normal incident for both the T_d (C_{2v}) and 1T' phases (C_{2h}) due to the symmetry [2, 3, 12]. To reveal the origin of sCPGE, we need to understand the reason of spatial dependence and explore more properties of this effect.

3.2 Experimental results and discussion

3.2.1 Swirling CPGE Current in Type-II Weyl Semimetal

The light source was still provided by a wavelength tunable Ti-Sapphire pulsed laser working at 750 nm. The laser was focused to a Gaussian profile by a 60X objective and the spot size was about 2 um diameter and 10 mW power. The light polarization

was controlled by a polarizer and a quarter wave plate installed on a motorized precision rotation stage driven by a servomotor. The polarization quality has been checked in the Chapter 2.

The bulk crystal $Mo_xW_{1-x}Te_2$ (x=0.3 and 0.9) and $MoTe_2$ was provided by Zheng Liu's group. The sample was exfoliated to flakes (20 um $\times$ 20 um) larger than previous experiments to avoid the beam reaching device edges and lowering the noise level. Layered structure $MoWTe_2$ sample was transferred onto Si/SiO_2 substrate and the crystallographic c axis of $MoTe_2$ was aligned to be parallel to the z axis which was the normal incident light direction as shown in Fig 3.1.

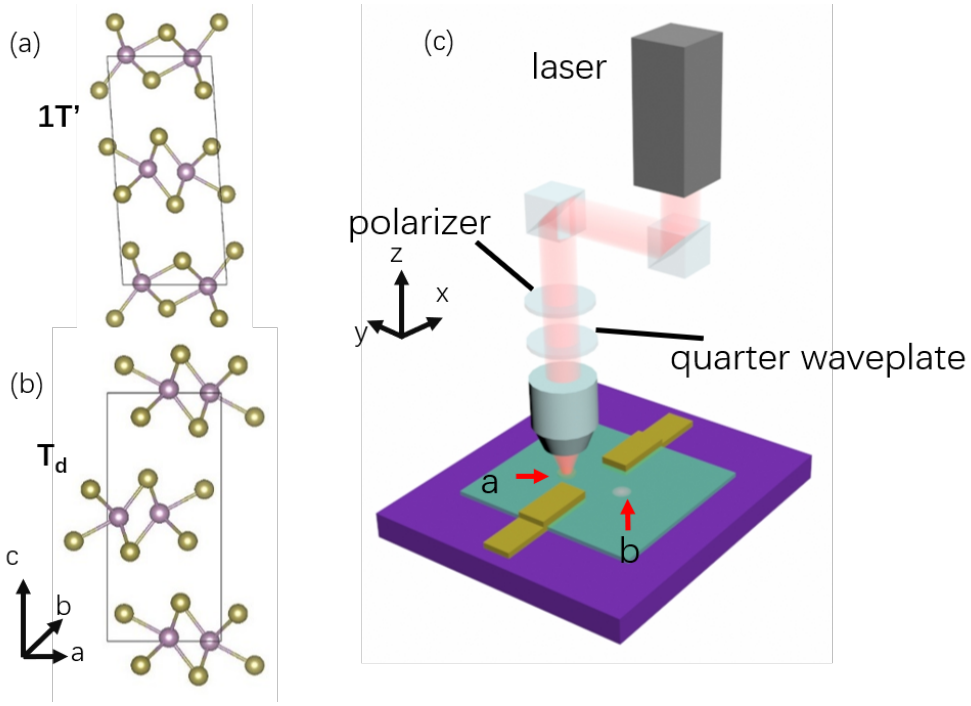

FIGURE 3.1: (a, b) Crystal structures of 1T' $MoTe_2$ (a) and T_d phase of $MoWTe_2$ (b). Yellow (purple) spheres represent Te (Mo) atoms. (c) Experimental set up of photocurrent measurement. 750 nm laser passes through a polarizer and a quarter waveplate in z direction, then normally incident on to the sample (x-y plane) after focused to 2 um diameter. Z axis in the set up is aligned as the c axis in the crystal structure.

To further test the dependence of sCPGE on position, experiments were performed

on $Mo_{0.9}W_{0.1}Te_2$ at room temperature where the beam spot was scanned along the perpendicular bisector of the two electrodes from spot a to spot b step by step, photocurrents as function of ϕ were collected at each step. Then, the photocurrents can be plotted and fitted by using the phenomenological photocurrent expression:

$$J = J_C sin(2\phi) + J_L sin(4\phi + \phi_0) + J_0 \tag{3.1}$$

The contribution from CPGE was extracted to get the position dependent CPGE. If the CPGE current distribution was swirling around the beam center, the result should be a sine shape.

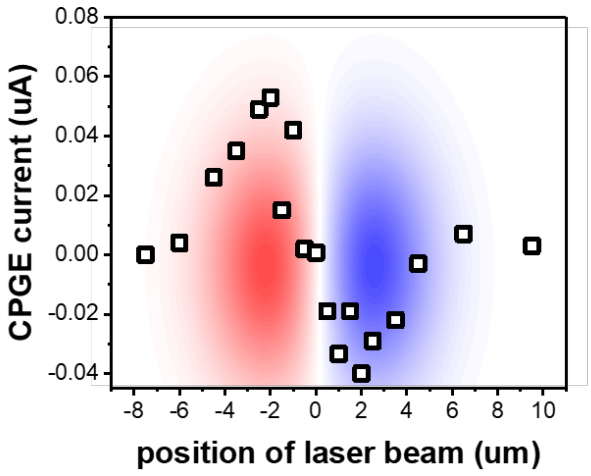

FIGURE 3.2: CPGE current, J_C, as a function of the laser beam position. Black squares are the experimental data extracted from the total photocurrent by fitting.

As given in the Fig 3.2, sCPGE J_C was zero when the laser spot was at the midpoint of two electrodes, and changed polarity when the spot moved from the left side to the right side, indicating that sCPGE current was an antisymmetric function of spot position. The CPGE current approached maximum at opposition direction when the beam position was about $\pm 2um$ away from the center. When the beam was far from the sample center, the CPGE current gradually deceased and vanished at the end. The result

was as expected for the swirling current explanation. If the beam was placed at the center, two half circle with opposite current direction would cancel each other, ending up with zero net current. When the beam was too far from the center, the electrode could not collect enough current, which was swirling around the beam spot, to get measurable data. Therefore, the CPGE maximum occurred when the distance between beam and electrode was about beam diameter, where the geometry was sufficiently asymmetric and the electrodes highly efficiently collected current.

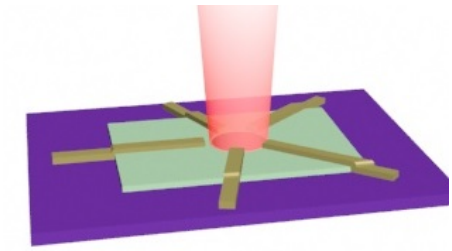

FIGURE 3.3: Schematic of our measurement set up to measure the circulating current in the Weyl phase.

According to the experiment above, the CPGE current distribution was likely to be circulating around the beam spot, however, the circulating current distribution was not the only explanation. To confirm the circulation, we designed a multi-electrode device where electrodes were arranged in a circle with the laser focused at the center and a fixed spot size, shown in the schematic Fig 3.3. If the current was flowing as a circle around the beam spot, current can be measured between two nearby electrodes. The reason why a circulating current in a plane can be collected by these two electrodes in our experimental setup can be simply explained by a electrostatic model (Fig3.4).

The electrons flowing out from the metal contacts were in equilibrium at the chemical potential of the contact (grounded in our case). Therefore, in a one-dimensional model, the electrons coming out of the grounded contacts were at zero chemical potential. Then, via the continuity equation, the current flowing into the contact would be $J = v_F(n_{in} - n_{out}) = v_F n_{in}$, with the electron density at the interface being $n = n_{in} + n_{out} = n_{in}$. In a one-dimensional ring, the Boltzmann equation and Ohm's law

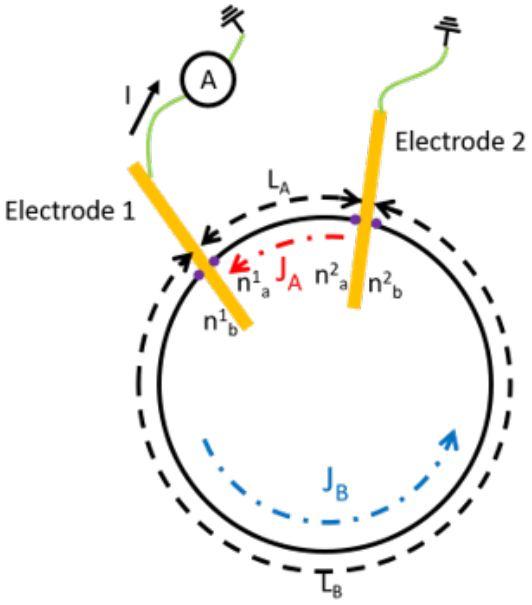

FIGURE 3.4: Schematic of our measurement set up to measure the circulating current in the Weyl phase. J_A (J_B) is the current magnitude flowing in the shorter (longer) segments of the loop, $n_a^{1(2)}$, $n_b^{1(2)}$ are the electron densities at the two Weyl semimetal-electrode interfaces of electrode 1 (2), adjacent to the shorter and longer segments, respectively.

gives, $\boldsymbol{j} = \sigma \boldsymbol{F}/e - D\frac{\partial n}{\partial x}$, and continuity equation is $\nabla \cdot j = 0$, where σ is the conductivity, F is the effective force on electrons due to optical illumination, and D is the electron diffusion constant, $D = v_F l$, where l is the electron mean free path.

For the ring geometry shown in Fig 3.4, a (b) stands for the shorter (longer) segment of the circle, J_A (J_B) is the current magnitude flowing in the shorter (longer) segment of the loop, $n_a^{1(2)}$, $n_b^{1(2)}$ are the electron densities at the Weyl semimetal-electrode interface 1 (2), adjacent to the shorter and longer segments respectively. The measured current is $I = J_A - J_B$ and $\sigma F/e$ is the transverse sCPGE current produced by light. We can then obtain,

$$J_A = v_F n_a^1 = -v_F n_a^2 = \boldsymbol{J}_{sCPGE}^{trans} - D\frac{n_a^1 - n_a^2}{L_A} \tag{3.2}$$

$$J_B = v_F n_b^2 = -v_F n_b^1 = \boldsymbol{J}_{sCPGE}^{trans} - D\frac{n_b^2 - n_b^1}{L_B} \tag{3.3}$$

which can be solved to obtain,

$$I = J_{sCPGE}^{trans} \cdot \frac{2l(L_A - L_B)}{(L_A + 2l)(L_B + 2l)} \tag{3.4}$$

Since the electrodes have a finite length, the measured current would be a radial integral of I(r). Therefore, with this multi-electrode design, same direction CPGE currents are expected to be obtain when photocurrents are measured between each two nearby electrodes under the same circularly polarized light.

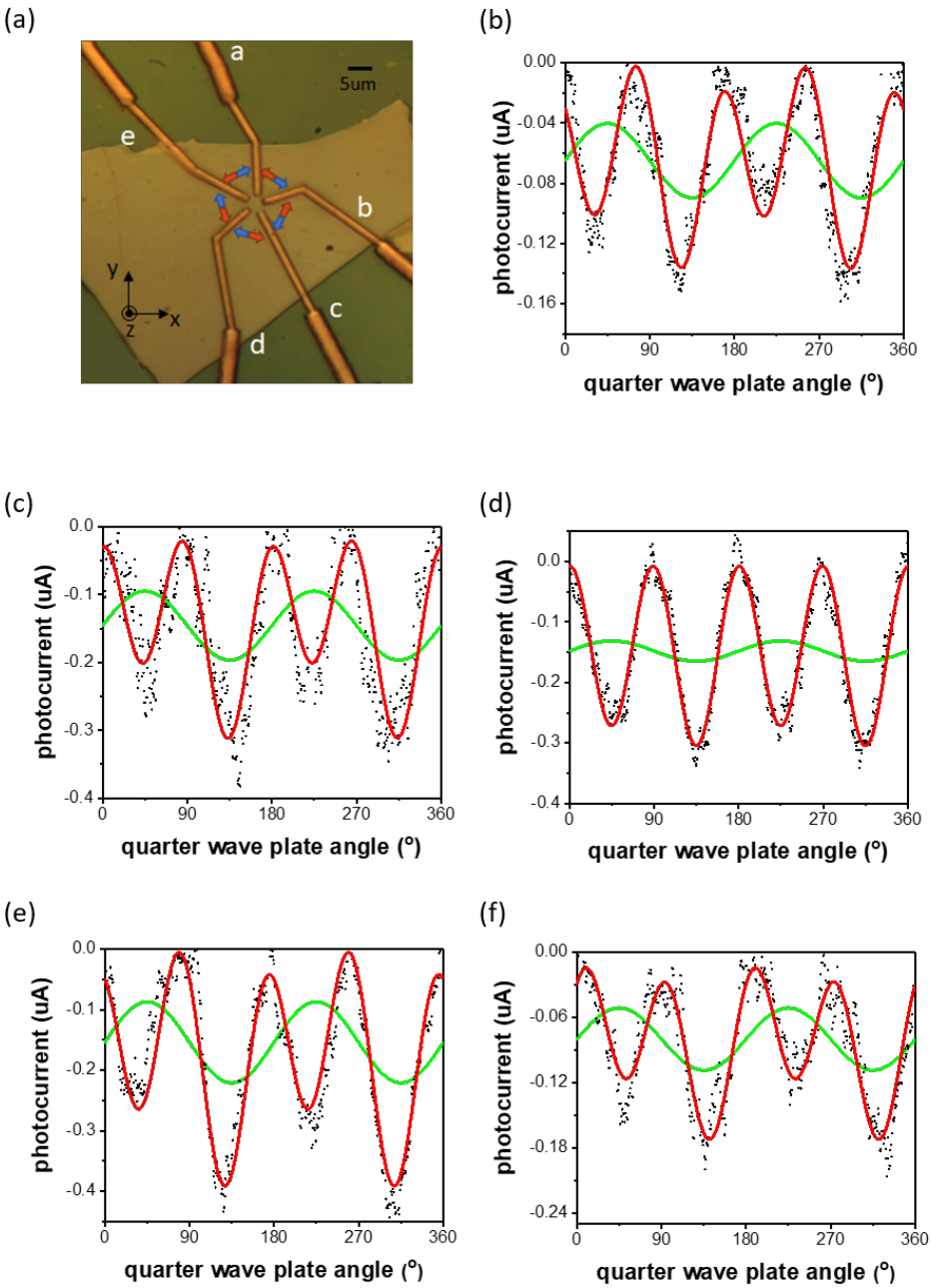

FIGURE 3.5: Measurement of circulating current in the T_d (Weyl) phase of $Mo_{0.9}W_{0.1}Te_2$ at room temperature under circularly polarized optical excitation. (a) Optical image of the multi-electrode $Mo_{0.9}W_{0.1}Te_2$ device (x-y plane). The five electrodes are labeled a-e, and red and blue arrows indicate the circulating direction of CPGE current under left and right circularly polarized light illumination (spot size ≈2um) respectively. (b-f) Photocurrents measured between each of the nearest electrode pairs and plotted as functions of the fast axis rotation angle, ϕ, of the quarter waveplate. Plots correspond to measurements performed between electrodes (b) a→b, (c) b→c, (d) c→d, (e) d→e, and (f) e→a. Black dots are the experiment data, red solid lines are the fitted curves for total photocurrent (Eqn (1)), and the green solid lines represent the fitted CPGE currents, J_C. The blue and red arrows represent the circulating CPGE current under RCP and LCP illumination, respectively.

For this multi-electrode measurement, the inversion symmetry broken T_d phase $Mo_{0.9}W_{0.1}Te_2$ was performed at room temperature. With the laser spot fixed at a point near the center of the circle surrounded by the electrodes, the photocurrent was collected between each of the nearest electrode pairs around the laser spot in the sequence, a→b, b→c, c→d, d→e and e→a. The optical photo of the device was given in Fig 3.5. As expected, sCPGE existed in $Mo_{0.9}W_{0.1}Te_2$ at room temperature and the polarization-dependent photocurrents were fitted to Eqn 3.1. sCPGE current contribution can be extracted from fitting.

All theses results between each two electrodes were shown in the Fig3.5. Obviously, the photocurrent at $\phi = 45°$ was larger than at $\phi = 135°$ in all these two measurements. Through fitting, J_C was find to be positive between all electrode pairs under right circularly polarized (RCP) light illumination and negative under left circularly polarized (LCP) light illumination, demonstrating that J_C was not biased in a single direction where the components collected by different electrode pairs would have different signs. Instead, J_C circulated clockwise (in the direction a→b→c→d→e→a) upon RCP excitation and reversed the winding direction under LCP excitation, indicating that the winding direction was determined by helicity of the light. Additionally, this circulating current by muti-electrode measurement can be repeated in different $Mo_{0.9}W_{0.1}Te_2$ devices with three, four and five electrodes. All these sCPGE current had the same circulating direction under same incident light helicity, indicating an intrinsic origin of sCPGE.

As shown in Chaper 2, the spatial dependent CPGE can only be observed in the Weyl phase by experiments on phase transition material $MoTe_2$. [10, 11] To confirm the CPGE current observed in low temperature phase $MoTe_2$ was the same circulating current as in $Mo_{0.9}W_{0.1}Te_2$, the multi-electrode experiment was repeated at $MoTe_2$ 77 k inversion symmetry broken Weyl phase.

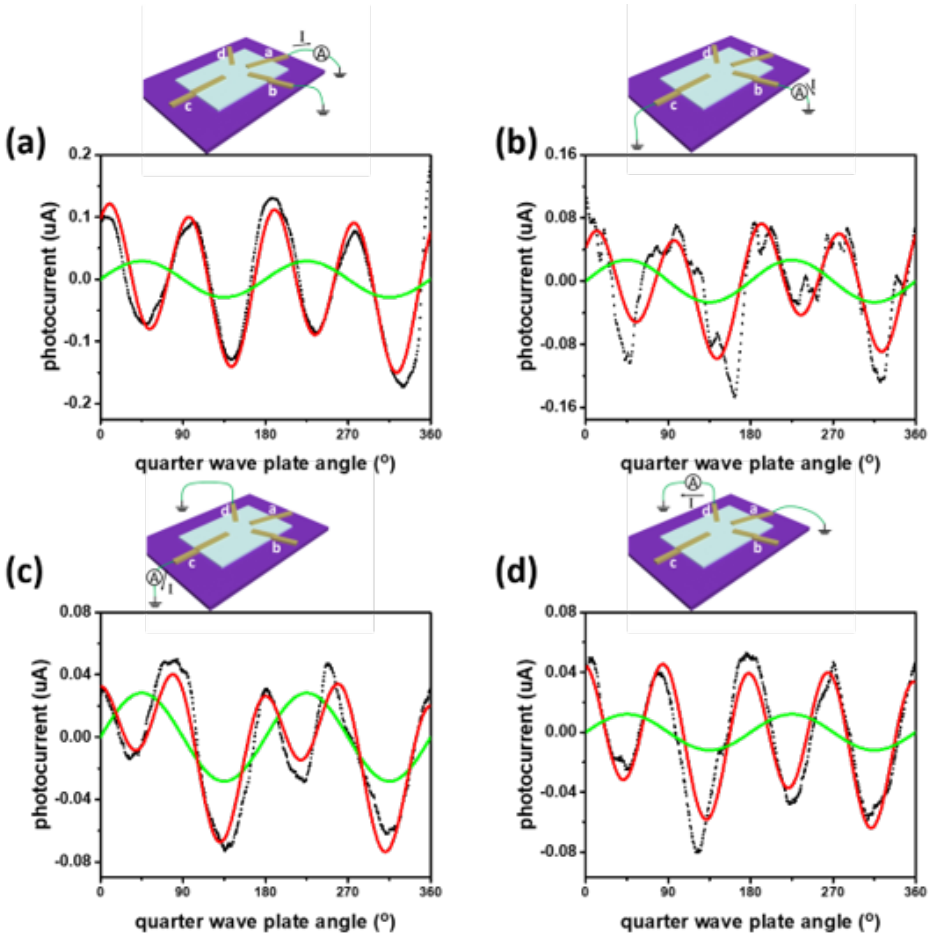

FIGURE 3.6: Measurement of circulating current in the T_d (Weyl) phase of $MoTe_2$ at 77 K under circularly polarized optical excitation. (a-d) Photocurrents measured between each of the nearest electrode pairs and plotted as functions of the fast axis rotation angle, ϕ, of the quarter waveplate. Plots correspond to measurements performed between electrodes (a) a→b, (b) b→c, (c) c→d, (d) d→a. Black dots are the experiment data, red solid lines are the fitted curves for total photocurrent (Eqn (1)), and the green solid lines represent the fitted CPGE currents, J_C. On top of each photocurrent curve is a schematic of the multi-electrode $MoTe_2$ device (x-y plane), with four electrodes labeled a-d.

In Fig 3.6, photocurrents were measured between each of the nearest electrode pairs and plotted as functions of the fast axis rotation angle, ϕ, of the quarter waveplate. The result was the same as the $Mo_{0.9}W_{0.1}Te_2$: the photocurrent at $\phi = 45°$ was larger than at $\phi = 135°$ in all measurements. All these sCPGE currents had the same sign, indicating that the current was circulating clockwise under RCP light and counterclockwise under LCP light. Therefore, this circulating CPGE was also proven at low temperature phase

$MoTe_2$, suggesting a unique effect only exists in the Weyl phase of $MoWTe_2$.

However, there was suspicion that the photocurrent can also be purely temperature dependent, for instance, the CPGE decreases with higher temperature [26]. The CPGE current at room temperature $MoTe_2$ could be too small to be collected, instead of being forbidden or suppressed by the 1T' phase. To exclude this possibility, multi-electrode measurements were performed at different temperatures between 300K and 77k on $MoTe_2$ and $Mo_{0.3}W_{0.7}Te_2$ for comparison. $Mo_{0.3}W_{0.7}Te_2$ composition used in this experiment can also check whether this effect is general in all Weyl phase composition at room temperature. At each temperature point, the measurement was similar as the multi-electrode setup shown before — photocurrents would be collected between two nearby electrodes and plotted as function of ϕ. By fitting the data into the phenomenological equation, contribution of CPGE can be obtained. The circulating CPGE amplitude was treated as the average of all of the CPGE current between two electrodes. Then, the temperature dependent circulating CPGE in $MoTe_2$ and $Mo_{0.3}W_{0.7}Te_2$ was obtained(Fig 3.7).

From the results shown in Fig 3.7, the circulating CPGE was observed at room temperature, consistent with the phenomenon in $Mo_{0.9}W_{0.1}Te_2$, which has the same phase. J_C was found positively correlated with temperature, which decreased from about 40 nA at 300 k to 18 nA at 77 K. In $MoTe_2$, J_C increased with temperature below 250 K where $MoTe_2$ had the same Weyl phase as $Mo_{0.9}W_{0.1}Te_2$ below 300 k, indicating a consistent temperature trend. However, there was a sudden drop of J_C when the temperature increased above 250 k, the phase change temperature of $MoTe_2$, and the CPGE current vanished at higher temperature. If the temperature was the only factor that affected the sCPGE current, the results above 250 K should have higher amplitude. Therefore, this experiment provided further evidence that the sCPGE current only exists in the inversion broken T_d phase.

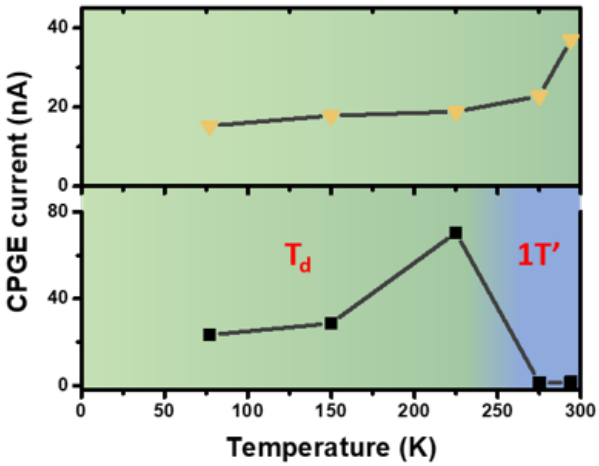

FIGURE 3.7: Temperature dependence of CPGE current measured on multi-electrode devices fabricated from $Mo_{0.3}W_{0.7}Te_2$ (top) and $MoTe_2$ (bottom). The data points are the average values of CPGE measured between four radially arranged electrode pairs. In T_d (Weyl) phase of $MoTe_2$ and $Mo_{0.3}W_{0.7}Te_2$ (top) and $MoTe_2$ (bottom). The data points are the average, which is represented by the green background color, the CPGE current maintains the same rotation direction at different temperatures and its amplitude increases with increasing temperature. In the bottom graph, above 250 K in the inversion symmetric 1T′ phase of $MoTe_2$, which is represented by the blue background color, there is no obvious CPGE current.

3.2.2 Beam Gradient controlled CPGE Current Amplitude

According to previous experiments, the sCPGE has been demonstrated to be swirling current in Weyl phase. However, the reason of the appearance of a CPGE current is still uncleared, because its circulating character requires a breaking of C_{2v} symmetry. The polarization-controlled circulating current is unlikely to originate from spatial disorder due to defects, in-plane strain during exfoliation, or formation of nanoscale junctions due to intermixing of different phases or compositions. Since in all these cases the current would flow in random directions depending on the direction of the local symmetry breaking, the experiment results can not be repeated as the work above. The possibility of CPGE current flowing along the edges of the sample can also be eliminated in Chapter 2.

However, a spatially inhomogeneous optical excitation due to a focused Gaussian

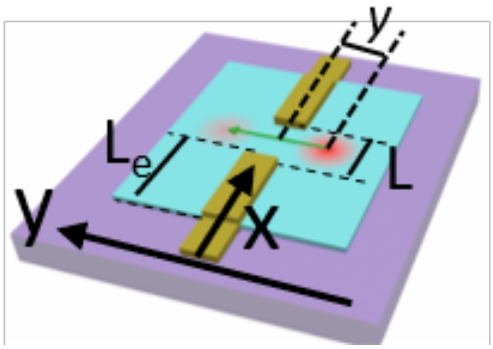

FIGURE 3.8: Parameters set for fitting the spatially dependent photocurrent measurement on $Mo_{0.9}W_{0.1}Te_2$ (x-y plane) in Fig 3.2. Laser beam (spot size about 2um) is scanned along the y axis, indicated by the green arrow. L_e is the total electrode length on the sample and L is the separation between the two electrodes.

beam profile performed in our experiments can effectively break the internal point symmetry to produce CPGE. This can be proven by analyzing the dependence of the CPGE on spatial gradients of the optical field profile. The CPGE current is circulating around the beam center with the amplitude assumed to be proportional to the beam intensity gradient. With this assumption, the qualitative description of CPGE - position dependence measurement in Fig 3.2 can be analyzed quantitatively.

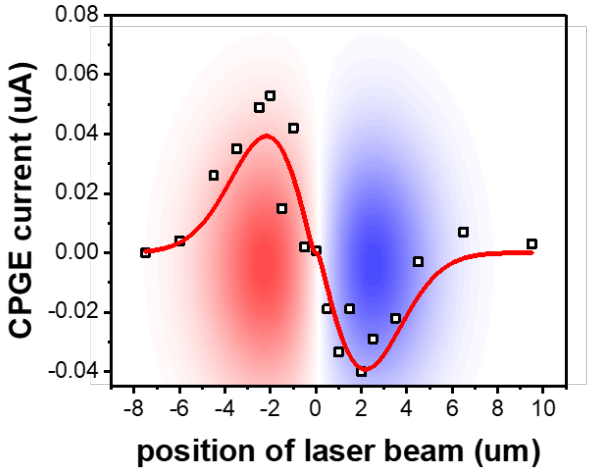

FIGURE 3.9: CPGE current, J_C, as a function of the laser beam position. Black squares are the experimental data and the red solid line is the fitting curve to the phenomenological model.

The parameters were defined in Fig 3.8. Two electrodes were separated by distance L in x direction. The beam with radius c was scanning in x direction between two electrodes. The electrodes had length L_e to collect the photocurrent. The current density at the circle with radius=r around the beam was proportional to the gradient of Gaussian profile at r. When the beam was located at position y, the measured current can be expressed as an integral of the current on electrode:

$$J_c = \int_{L/2}^{L_e+L/2} dl \cdot y e^{-\frac{y^2+(\frac{l}{2})^2}{c^2}} \beta_{\theta rz} \tag{3.5}$$

Using the Eqn 3.5 to fit the position dependent CPGE, the result was given by the red curve in Fig 3.9, which matched well with the data.

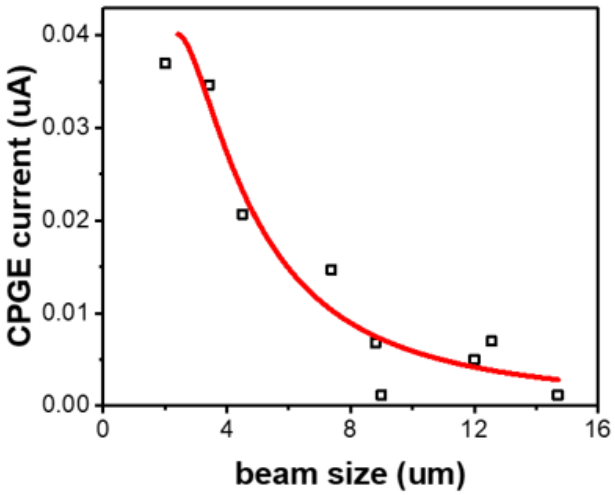

FIGURE 3.10: CPGE current, J_C, plotted as a function of the Gaussian beam diameter at a fixed distance y_0 to electrodes. Black squares are the experimental data and the red solid line is the fitting curve to the expression derived from the phenomenological model of j_{sCPGE}.

Another signature of sCPGE current can be observed upon varying the spot size while keeping the beam position fixed. In these experiments, via moving the stage up and down, the beam size was modified while the center of the beam was fixed and the beam profile was still Gaussian. At each stage height, photocurrents were collected while rotating quarter wave plate plot of photocurrent as function of ϕ. After fitting into the phenomenological equation, CPGE current component J_c can be obtained. As given

in Fig 3.10, J_c was plotted as function of beam size. The amplitude of J_C decreased when the spot size increased and the field gradients decreased. Besides, for large electrode separation compared to spot size, J_C again decreased because the circulating current can not be collected efficiently at the electrodes. If we use the same assumption as in the spatial dependent CPGE measurement, we can get the beam size dependent fitting equation:

$$J_c \sim \int_{L/2}^{L/2+L_E} \frac{1}{c^2} e^{-\frac{2r^2}{c^2}} \sigma_{\theta rz} dr \tag{3.6}$$

where c is the radius of the Gaussian beam. The fitting curve using Eqn 3.6 was plotted in Fig 3.10, which well matched the experimental data. All these experiments indicated that the observed strong sCPGE in the inversion broken phase was controlled by the optical beam profile and polarization state.

In summary, we can conclude that the sCPGE is circulating around the center of the beam and the current amplitude is controlled by the beam profile: the current has opposite sign if measured at opposite side of the beam and reaches maximum when the beam size is comparable to the distance between two electrodes, implying that the current is proportional to beam gradient. The experiments above were all under high energy excitation. Does this sCPGE keep the same property at low energy excitation?

3.2.3 sCPGE at Low Energy Excitation

To study the sCPGE at low frequency excitation around the Weyl cone, 6 um CW laser was performed for photocurrent measurements. $Mo_{0.9}W_{0.1}Te_2$ sample was exfoliated to about $500um \times 500um$ size and transferred to a chip carrier. The reason why the sample size was much bigger than the sample in experiments for 750 nm was that the laser beam size at 6um was much larger than at 750 nm. Two Al wires were bonded onto two sides of the sample, used as electrodes. Fig 3.11 was the optical image of the device, and the laser light would be normally incident on the sample plane (x-y plane).

Since the 6 um laser was CW laser and 750 nm laser was pulsed laser and the beam

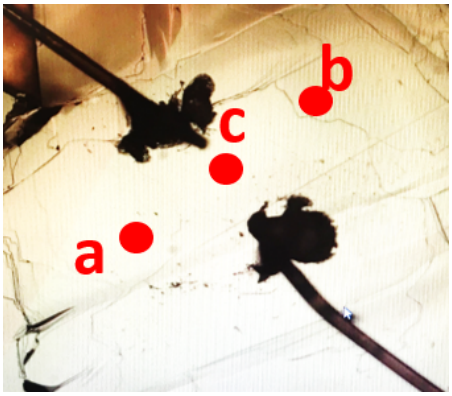

FIGURE 3.11: Optical image of the $Mo_{0.9}W_{0.1}Te_2$, in which three red spots indicate the three beam positions of photocurrent measurements.

size was much larger, the intensity gradient was significantly smaller than previous experiments, resulting in lower CPGE current. Thus, the Lock-in amplifier was added into the electrical setup for fine current measurements. (Fig 3.12) A chopper was placed in the optical path to generate a reference frequency for the light, and was connected to the Lock-in amplifier. The chopper was set to 377 Hz (lowest noise we found for measurement) and the signal, which was coming from the light excitation, can be collected only at this frequency.

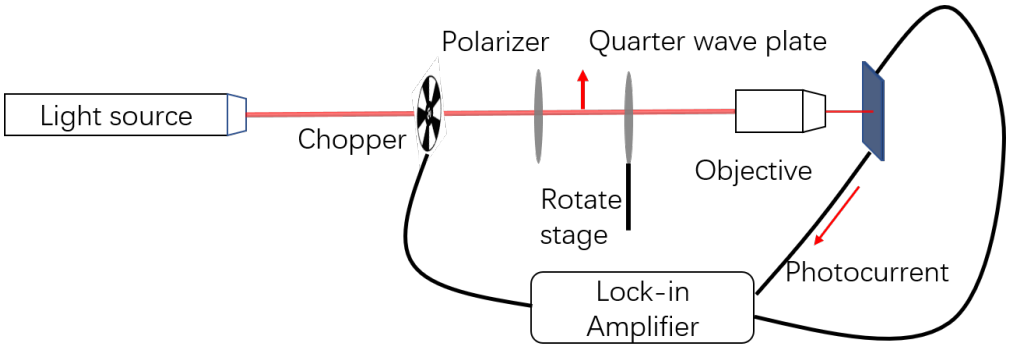

FIGURE 3.12: Electrical setup for small current measurement using Lock in amplifier.

Firstly, 750nm photocurrent measuremenfts similar to the spatial dependent measurements before were repeated on this sample. The beam size was adjusted to be comparable to the distance between two electrodes to get relatively large sCPGE current. The beam was fixed while rotating the quarter wave plate at speed $7^\circ/s$, meanwhile

collecting the photocurrent. Photocurrent was plotted as a function of quarter wave plate fast axis rotation angle ϕ. The data can be fitted into the phenomenological photocurrent equation:

$$J = J_C + sin(2\phi) + J_L sin(4\phi + \phi_0) + J_0 \tag{3.7}$$

As shown in Fig 3.13, sCPGE was clearly observed at both spot a (bottom left side) and spot b (top right side) and the sCPGE currents at two spots have opposite direction as expected.

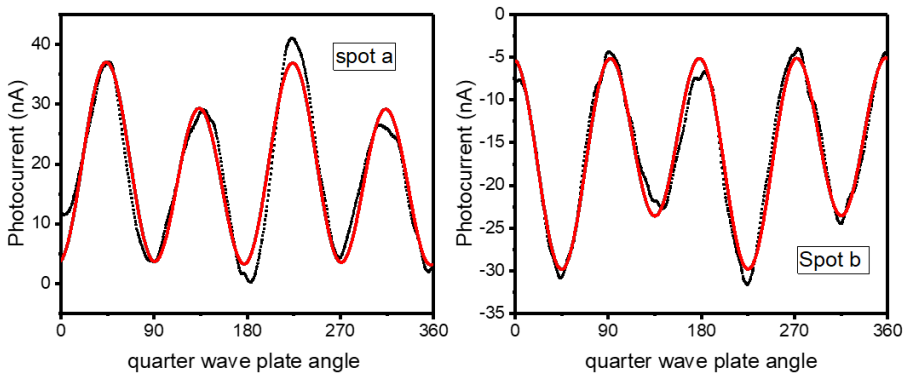

FIGURE 3.13: Photocurrents measured on $Mo_{0.9}W_{0.1}Te_2$ flake by 750 nm laser plotted as a function of quarter waveplate fast axis rotation angle ϕ at spot a and spot b respectively. Black dots are the experimental data and red solid lines are the fits to Eqn 3.7

Then, 6 um laser was performed on the same sample for low energy excitation sCPGE measurements. Because the laser spot was not visible at this wavelength, the relative position between the beam and sample was determined by sweeping the beam all over the sample and mapping out the thermo-current J_0. The positive and negative maxima thermocurrent represented the position of two electrodes. The coordinates of electrodes were recorded and the location of spot a and spot b can be calculated. The experimental process was similar to the measurement at 750 nm. As shown in Fig 3.14, the characteristics of the measured photocurrent agreed with the results at near-IR (750 nm) measurements, as the CPGE current J_C was negative at spot a and positive at spot b.

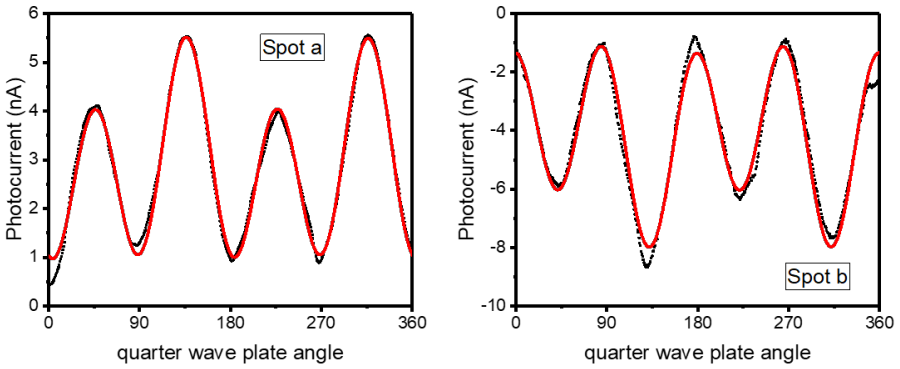

FIGURE 3.14: Photocurrents measured on $Mo_{0.9}W_{0.1}Te_2$ flake by 6 um laser plotted as a function of quarter waveplate fast axis rotation angle ϕ at spot a and spot b respectively. Black dots are the experimental data and red solid lines are the fits to Eqn 3.7

These results indicated that the CPGE current was also circulating around the beam and sCPGE existed at the Lifshitz energy scale as well.

Furthermore, beam size dependent CPGE measurement was performed under 6 um laser to prove that the sCPGE at low frequency excitation shared the same phenomenology as high frequency. By moving the stage up and down, the beam size would be modified while the center of the beam was fixed. At each stage height, photocurrents were collected while rotating quarter wave plate to plot photocurrent as function of ϕ. After fitting into the Eqn 3.7, CPGE current component J_c can be obtained and J_c was plotted as function of stage height.

The beam profile at 6 um was also Gaussian beam, therefore, it can be fitted by the same phenomenological model as 750 nm. Since the electric contact was made by directly wire bond, the collected current was proportional to beam gradient at r, where r is the distance between beam center and electrode. After focus the beam and move the objective for distance x, the radius of the Gaussian beam R should be :

$$R^2(x) = R_0^2[1 + (\frac{\lambda x}{\pi R_0^2})^2] \tag{3.8}$$

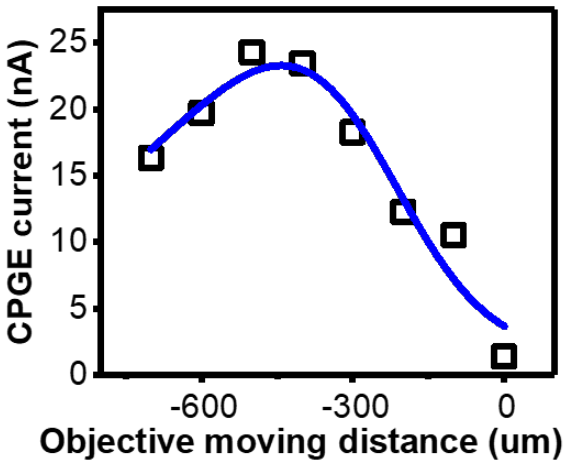

FIGURE 3.15: When the 6um laser beam position is fixed, sCPGE current is plotted as a function of the objective moving distance. The black square is sCPGE data and the blue curve is the fitting function by the phenomenological model.

where R_0 is the most focused beam radius. Therefore, at height x, the CPGE current can be expressed as:

$$J_C \sim \frac{r}{R^2} e^{-\frac{r^2}{R^2}} \beta_{\theta rz} \tag{3.9}$$

Fitting the CPGE current at different x at into the Eqn 3.9, we found that the CPGE current magnitude was still controlled by the beam profile, similar to the result at 750 nm illumination. Besides, we got the radius of Gaussian beam at zero x: $R_0 \approx 80um$, which matched very well with the design of objective. The beam size dependent experiment assured that the sCPGE at low energy excitation was also circulating around the beam center with current density determined by the beam profile gradient, suggesting that the phenomenology of sCPGE can be used in a broad energy spectrum.

More interestingly, by comparing the results of the CPGE current at 750 nm and 6 um, we found that the sign of the currents were opposite. As can be seen in the Fig 3.16, at spot a, the photocurrent at $\phi = 45°$ was larger than the photocurrent at $\phi = 135°$ for 750 nm wavelength, while the photocurrent at $\phi = 45°$ was smaller than the photocurrent at $\phi = 135°$ for 6 um. At spot b, vice versa. Therefore, the CPGE current was swirling in opposite directions at these two wavelengths. In other words,

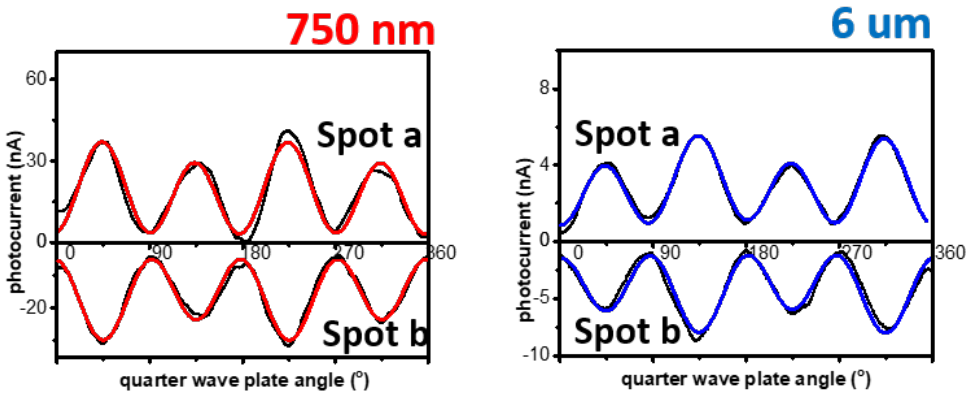

FIGURE 3.16: The photocurrents as the function of ϕ at same electrical setup for 750 nm and 6 um wavelength. The results are compared at spot a and spot b.

the circulating CPGE had opposite handedness at high and low excitation energy.

To confirm the sCPGE dependence on wavelength, several more wavelengths laser from 700 nm to 1050 nm were performed to measure the CPGE current at a fix beam spot. As can be seen in Fig 3.17, all the CPGE currents had the same polarity when the wavelength were at 700 nm, 750 nm, 800 nm, 950 nm and 1050 nm, which were all above the Lifshitz energy. The amplitude of the CPGE had a trend to decrease with longer wavelength.

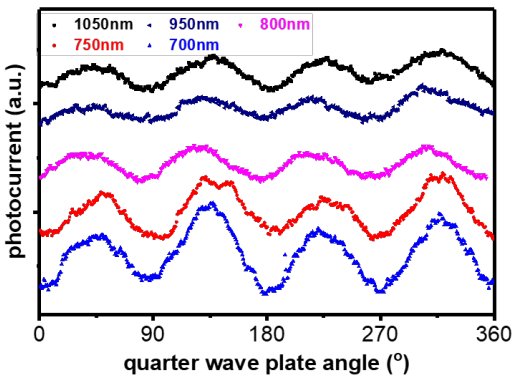

FIGURE 3.17: The photocurrents as the function of ϕ at same electrical setup for light wavelength at 700 nm, 750 nm, 800 nm, 950 nm and 1050 nm.

For a brief summary of the experimental observation, sCPGE was observed in a wide spectral range and kept the same phenomenology. However, the circulating current direction reversed at 750 nm and 6 um wavelength. A microscopic model was then derived to explain these observed properties of sCPGE.

3.3 Microscopic Model

Photogalvanic effect is a nonlinear dc response second order in the applied field, mixing the oscillating electric field components at frequencies ω and -ω, [13]

$$\begin{aligned} J_{i,PGE} &= \vartheta^{+}_{ijk}(\omega,-\omega)E_j(\omega)E_k(-\omega) + \vartheta^{-}_{ijk}(\omega,-\omega)E_j(\omega)E_k(-\omega) \\ &= \vartheta_{ijk}(\omega,-\omega)E_j(\omega)E_k(-\omega) \end{aligned} \tag{3.10}$$

where J_{PGE} is the photogalvanic current, $E_i(t) = E_i(\omega)e^{i\omega t} + E_i(-\omega)e^{-i\omega t}$ is the incident field, $E_i(\omega) = E_i^*(-\omega)$, $\vartheta^{-}_{ijk}(\omega,-\omega) = \vartheta^{+}_{jik}(\omega,-\omega)$ and $\vartheta_{ijk}(\omega,-\omega) = \vartheta^{+}_{ijk}(\omega,-\omega) + \vartheta^{-}_{ijk}(-\omega,\omega)$. The nonlinear response coefficient for PGE current $\vartheta^{-}_{ijk}(\omega)$ is a third rank tensor with the first index describing the direction of current, and the other two representing directions of the two electric fields.

General PGE expressions can be symmetrized with respect to frequency and indices j and k. Circular photogalvanic effect response is odd in frequency ω, antisymmetric under the interchange of j and k while linear photogalvanic effect response is even in ω and symmetric under the exchange of j and k.

$$\begin{aligned} J_{i,PGE} = A_{ijk}(\omega)\left(\frac{E_j(\omega)E_k(-\omega) - E_j(-\omega)E_k(\omega)}{2}\right) \\ + B_{ijk}(\omega)\left(\frac{E_j(\omega)E_k(-\omega) + E_j(-\omega)E_k(\omega)}{2}\right) \end{aligned} \tag{3.11}$$

CPGE is descirbed by $A_{ijk}(\omega) = \frac{1}{2}(\vartheta_{ijk}(\omega) - \vartheta_{ijk}(-\omega)$, and LPGE is described by $B_{ijk}(\omega) = \frac{1}{2}(\vartheta_{ijk}(\omega) + \vartheta_{ijk}(-\omega)$.

Spatially dispersive photogalvanic effect (s-PGE) is a specific photogalvanic response when the optical field is spatially inhomogeneous, characterized by a spatial gradient wavevector, $\boldsymbol{q}$. In the perturbative (small $\boldsymbol{q}$) limit, where s-PGE current is dominated

by components with first order in $\boldsymbol{q}$. sCPGE and sLPGE can be written as:

$$\begin{aligned} J^i_{sCPGE}(\boldsymbol{r}) &= \Sigma_{\boldsymbol{q}} J^i_{sCPGE}(\boldsymbol{q}) e^{2i\boldsymbol{q}\cdot\boldsymbol{r}} = \Sigma_{\boldsymbol{q}} \beta_{ilj} q_l (\boldsymbol{E}(\boldsymbol{q},\omega) \times \boldsymbol{E}(\boldsymbol{q},-\omega))_j e^{2i\boldsymbol{q}\cdot\boldsymbol{r}} \\ J^i_{sLPGE}(\boldsymbol{r}) &= \Sigma_{\boldsymbol{q}} J^i_{sLPGE}(\boldsymbol{q}) e^{2i\boldsymbol{q}\cdot\boldsymbol{r}} \\ &= \Sigma_{\boldsymbol{q}} \gamma_{iljk} q_l \left(\frac{(E_j(\boldsymbol{q},\omega)E_k(\boldsymbol{q},-\omega)) + (E_j(\boldsymbol{q},-\omega)E_k(\boldsymbol{q},\omega))}{2}\right) e^{2i\boldsymbol{q}\cdot\boldsymbol{r}} \end{aligned} \tag{3.12}$$

where pseudo third rank tensor β and fourth rank tensor γ are the conductivity matrices for s-PGE current. For small $\boldsymbol{q}$, the equations adopt a simpler form,

$$\begin{aligned} J^i_{sCPGE}(\boldsymbol{r}) &= \beta_{ilj} q_l (\boldsymbol{E}(\boldsymbol{r},\omega) \times \boldsymbol{E}(\boldsymbol{r},-\omega))_j \\ J^i_{sLPGE}(\boldsymbol{r}) &= \gamma_{iljk} q_l \left(\frac{(E_j(\boldsymbol{r},\omega)E_k(\boldsymbol{r},-\omega)) + (E_j(\boldsymbol{r},-\omega)E_k(\boldsymbol{r},\omega))}{2}\right) \end{aligned} \tag{3.13}$$

Furthermore, continuity equation $\partial_t \rho + \nabla \cdot J = 0$ suggests that the steady state s-PGE current satisfies $\nabla \cdot \boldsymbol{J}_{sCPGE} = 0$ to obey charge conservation. If not, the longitudinal part of $\boldsymbol{J}_{sPGE}$ would be compensated by some in-plane scalar potential (chemical, electric, etc) and would not contribute to the circulating current ($\boldsymbol{q} \cdot \boldsymbol{J}_{sPGE} = 0$). So, we divide $\boldsymbol{J}_{sPGE}$ into transverse and longitudinal parts, $\beta_{ilj} = \frac{1}{2}(\beta_{ilj} - \beta_{lij}) + \frac{1}{2}(\beta_{ilj} + \beta_{lij})$, with the transverse s-PGE given by,

$$J^{trans}_{i,sCPGE}(\boldsymbol{q}) = \frac{1}{2}(\beta_{ilj} - \beta_{lij}) q_l (\boldsymbol{E}(\boldsymbol{r},\omega) \times \boldsymbol{E}(\boldsymbol{r},-\omega))_j \equiv \sigma_{jlj} q_l (\boldsymbol{E}(\boldsymbol{r},\omega) \times \boldsymbol{E}(\boldsymbol{r},-\omega))_j \tag{3.14}$$

$$\begin{aligned} J^{trans}_{i,sLPGE}(\boldsymbol{q}) &= \frac{1}{2}(\gamma_{iljk} - \gamma_{lijk}) q_l \frac{(E_j(\boldsymbol{r},\omega)E_k(\boldsymbol{r},-\omega)) + (E_j(\boldsymbol{r},-\omega)E_k(\boldsymbol{r},\omega))}{2} \\ &\equiv \mu_{iljk} q_l \frac{1}{2}(\gamma_{iljk} - \gamma_{lijk}) q_l \frac{(E_j(\boldsymbol{r},\omega)E_k(\boldsymbol{r},-\omega)) + (E_j(\boldsymbol{r},-\omega)E_k(\boldsymbol{r},\omega))}{2} \end{aligned} \tag{3.15}$$

As for the electric field of a Gaussian beam with photon energy $\hbar\omega$ in real space, $\boldsymbol{E}(\boldsymbol{r},t) = \Sigma_{\boldsymbol{q},\omega} \boldsymbol{E_0}(\boldsymbol{q},\omega) e^{i\omega t} e^{i\boldsymbol{q}\cdot\boldsymbol{r}} \propto e^{-(r-r_g)^2/\omega^2}$ where $r - r_g$ is the radial coordinate of r relative to the spot center r_g, and ω is the Gaussian beam width. Using the equation of continuity, the circulating CPGE current arises from the transverse part of $\boldsymbol{j}_{sCPGE}$,

produced by the antisymmetric term in the conductivity: $\sigma_{ilj} = 1/2(\beta_{ilj} - \beta_{lij})$. The direction of the transverse current $\boldsymbol{j}_{sCPGE}$ is then determined by the direction of $\boldsymbol{q}$ and the propagation direction of the optical field $\hat{\boldsymbol{n}}$ ($\hat{\boldsymbol{n}}$ defined by $i\hat{\boldsymbol{E}} \times \hat{\boldsymbol{E}}^*$) : $\hat{\boldsymbol{j}}_{\boldsymbol{sCPGE}} = \hat{\boldsymbol{q}} \times \hat{\boldsymbol{n}}$. Here $\boldsymbol{q}$ is in the radial direction, and its magnitude follows the distribution obtained via a Fourier transform of the two-dimension Gaussian beam profile, while $\hat{\boldsymbol{n}}$ is along the light propagation direction, i.e., $\pm\hat{\boldsymbol{n}}$. Therefore, $\boldsymbol{j}_{sCPGE}$ circulates around the beam center with an amplitude proportional to the length of $\boldsymbol{q}$ and a sign determined by the photon helicity, as observed experimentally. The measured photocurrent magnitude can be related to $\boldsymbol{j}_{sCPGE}$ by a geometric factor associated with the electrode positions, and photocurrent is captured by a simple electrostatic model as mentioned before. When scanning the laser spot position perpendicular to the two electrodes Fig 3.9, J_C collected by the electrode pair reflects the antisymmetric dependence on spatial coordinates of $\boldsymbol{j}_{sCPGE}$, and can be well fitted. The dependence of J_C on the Gaussian beam width when the laser beam position is fixed is also reproduced by our model, (Fig 3.10) indicating that the phenomenological expression is consistent with the experimental data.

3.3.1 Calculation of electron density matrix under inhomogeneous optical excitation

To describe s-PGE microscopically, the conductivity matrix needs to be derived. The second order susceptibility formalism developed by Sipe et al. [14] is capable of describing most of the PGE responses for a spatially homogeneous beam excitation, but it cannot be applied to our case of excitation with a spatially varying optical beam. This type of excitation makes the spatially varying carrier excitation not captured in Sipe's formalism. Therefore, we started with the general kinetic equation of the quantum density matrix $\rho(\mathbf{r}, \mathbf{k}, t)$ obtained from a Wigner transformation of the quantum Liouville equation as derived by Sekine et al. [15] The equation for $\rho(\mathbf{r}, \mathbf{k}, t)$ is then expanded to

first order in spatial gradients to calculate the response functions for s-PGE. The quantum kinetic equation is given by,

$$\frac{\partial\rho(\mathbf{r},\mathbf{k},t)}{\partial t}+\frac{i}{\hbar}[H_0,\rho(\mathbf{r},\mathbf{k},t)]+\frac{1}{2\hbar}\frac{DH_0}{Dk}\cdot\nabla\rho(\mathbf{r},\mathbf{k},t)+K(\rho(\mathbf{r},\mathbf{k},t))=\frac{e\mathbf{E}}{\hbar}\cdot\frac{D\rho(\mathbf{r},\mathbf{k},t)}{Dk} \tag{3.16}$$

where $\rho(\mathbf{r},\mathbf{k},t)$ is a $N\times N$ density matrix. $\rho(\mathbf{r},\mathbf{k},t)$ can be solved order by order in the electric field which is shown in Z. Ji, et al's work [29].

3.3.2 Spatially dispersive PGE response function

Photogalvanic response consists of injection [14], shift [14, 16] and anomalous currents [17, 18]. The full response at spatial local $\boldsymbol{r}$ is denoted by

$$j_{sPGE}(r)=j_{s-Inj}(r)+j_{s-Shift}(r)+j_{s-Ano}(r) \tag{3.17}$$

Injection current, or so called "circular photocurrent" appears only under circularly polarized light excitation and is regarded as the dominate contribution to CPGE measurements. Analogous to the injection current, $\boldsymbol{j}_{sPGE}$ has a component like $e\Sigma_{k,n}\rho^{(2)}_{nn}\mathbf{v}_{nn}(\mathbf{k})$, where $\Sigma_{\mathbf{k}}\equiv\frac{\int_{\mathbf{k}}d^3\mathbf{k}}{(2\pi)^3}$, and density matrix was derived in the work. [29]

There are two interband transition terms that are expected to control the response functions at high energy excitation. The first term originates from the contribution of the non-Fermi surface part of $j(\mathbf{q})\sim e\Sigma_{k,n}\rho^{(2,0)}_{nn}\cdot v_{nn}v_{nn}$, and the current is:

$$\begin{aligned}&i^k_{s-Inj,1}(\mathbf{q})=q_l\sum_{k,n,m}\frac{2e^3}{\hbar^2}(\Gamma_{nm}(\omega)+\Gamma_{nm}(-\omega))(f_0(\varepsilon_m)-f_0(\varepsilon_n))R^i_{nm}R^j_{mn}\\&(v^l_{nn}v^k_{nn}\tau^2_{nn}-v^l_{mm}v^k_{mm}\tau^2_{mm})E_i(\mathbf{q},\omega)E_j(\mathbf{q},-\omega)\end{aligned} \tag{3.18}$$

The second term is from $j(\mathbf{q})\sim e\Sigma_{k,n,m}(R_{nm}\rho^{(1,1)}_{mn}-\rho^{(1,1)}_{nm}R_{mn})v_{nn}$, and the current can be written as:

$$j^k_{s-Inj,2}(\mathbf{q}) = iq_l \sum_{k,n,m} \frac{e^3}{2\hbar}(\Gamma^2_{nm}(\omega) + \Gamma^2_{mn}(-\omega))R^i_{nm}R^j_{mn}(f_0(\varepsilon_n) - f_0(\varepsilon_m)) \\ (v^l_{nn} + v^l_{mm})(v^k_{nn}\tau_{nn} - v^k_{mm}\tau_{mm})E_i(\mathbf{q},\omega)E_j(\mathbf{q},-\omega) \tag{3.19}$$

Spatially dispersive CPGE part (sCPGE)

The components in $j^k_{s,1}(\mathbf{q})$ and $j^k_{s,2}(\mathbf{q})$ that we are particularly interested in are those odd of frequency giving rise to sCPGE. The expressions are:

$$j^k_{sCPGE,1}(\mathbf{q}) = q_l \sum_{k,n,m} \frac{e^3}{\hbar^2}(\Gamma_{nm}(\omega) + \Gamma_{mn}(-\omega))(f_0(\varepsilon_m) - f_0(\varepsilon_n))(R^i_{nm}R^j_{mn} - R^i_{mn}R^j_{nm}) \\ (v^l_{nn}v^k_{nn}\tau^2_{nn} - v^l_{mm}v^k_{mm}\tau^2_{mm})E_i(\mathbf{q},\omega)E_j(\mathbf{q},-\omega) \tag{3.20}$$

$$j^k_{sCPGE,2}(\mathbf{q}) = iq_l \sum_{k,n,m} \frac{e^3}{4\hbar}(\Gamma^2_{nm}(\omega) + \Gamma^2_{mn}(-\omega))(R^i_{nm}R^j_{mn} - R^i_{mn}R^j_{nm})(f_0(\varepsilon_n) - f_0(\varepsilon_m)) \\ (v^l_{nn} + v^l_{mm})(v^k_{nn}\tau_{nn} - v^k_{mm}\tau_{mm})E_i(\mathbf{q},\omega)E_j(\mathbf{q},-\omega) \tag{3.21}$$

The two j^k_{sCPGE} expressions only involve the antisymmetric parts of τ_{nn}, which needs inversion symmetry to be broken. If we further assume that $\tau_{nn} = \tau_{mm}$ does not dependent on band index, then $j^k_{sCPGE,1}$ is purely longitudinal, while $j^k_{sCPGE,2}$ contains a transverse part. The quantity that appears in the equations, $\Omega^k_{nm}(\mathbf{k}) = -i(R^i_{nm}R^j_{mn} - R^i_{mn}R^j_{nm})$ along $\hat{k} = \hat{i} \times \hat{j}$ is associated with the Berry curvature $\mathcal{B}^k_n(\mathbf{k})$, $\mathcal{B}^k_n(\mathbf{k}) = \Sigma_m \Omega^k_{nm}(k)$. It transforms like Berry curvature: $\Omega^k_{nm}(\mathbf{k}) = \Omega^k_{nm}(-k)$ under inversion symmetry, and $\Omega^k_{nm}(k) = -\Omega^k_{nm}(-\mathbf{k})$ under time reversal symmetry. Therefore, in a system with both time reversal and inversion symmetry, $\Omega^{ij}_{nm}(\mathbf{k})$ vanishes, and so do sCPGE terms in the equation 3.20 and 3.21.

Spatially dispersive LPGE part (sLPGE)

Conventionally, linearly polarized light cannot produce injection current in centrosymmetric materials. However, here we find that it can contribute to sLPGE in these systems. Similar to $\boldsymbol{j}_{sCPGE}$, $\boldsymbol{j}_{sLPGE}$ represents the spatially dispersive LPGE part. Again, if we assume that the relaxation time does not depend on the band index ($\tau_{nn} = \tau_{mm}$), the transverse part of $\boldsymbol{j}_{sLPGE}$ is mainly from $\boldsymbol{j}_{s-Inj,2}$:

$$\begin{aligned} j^k_{sLPGE,2}(\mathbf{q}) =& iq_l \sum_{k,n,m} \frac{e^3}{4\hbar}(\Gamma^2_{nm}(\omega) + \Gamma^2_{mn}(-\omega))(R^i_{nm}R^j_{mn} + R^i_{mn}R^j_{nm})(f_0(\varepsilon_n) - f_0(\varepsilon_m)) \\ & (v^l_{nn} + v^l_{mm})(v^k_{nn}\tau_{nn} - v^k_{mm}\tau_{mm})E_i(\mathbf{q},\omega)E_j(\mathbf{q},-\omega) \end{aligned} \tag{3.22}$$

The equation can also be written in the form of conductivity. A linearly polarized light in the ith direction could give a sLPGE conductivity [29]:

$$\begin{aligned} \mu_{klii} =& i \sum_{k,n,m} \frac{e^3}{2\hbar}(\Gamma^2_{nm}(\omega) + \Gamma^2_{mn}(-\omega))R^i_{nm}R^i_{mn}(f_0(\varepsilon_n) - f_0(\varepsilon_m)) \\ & (v^l_{nn} + v^l_{mm})(v^k_{nn}\tau_{nn} - v^k_{mm}\tau_{mm}) \end{aligned} \tag{3.23}$$

The LPGE integral is not constrained by inversion symmetry, in accordance with the experimental observation that sLPGE responses exist in both the inversion broken Weyl phase and the 1T′ phase.

Spatially Dispersive Shift Current and Anomalous Current

The other part of the s-PGE response is the "spatially dispersive shift current" denoted as s-Shift current. Time dependent measurements have been done to distinguish shift current from injection current. [19] However, compared to the injection current whose magnitude in the no collision (large relaxation time) limit grows linearly to infinity, shift current is always finite, so in steady state CPGE measurements for materials with long relaxation time (weak disorder) are not considered a dominating term. [20]

Besides, s-Shift current has both CPGE and LPGE parts, but is not affected by inversion operation. In our experiments, CPGE only appears upon phase transition to an inversion broken Weyl phase, s-Shift current that would exist in both phases cannot be the main contribution to the measured current.

Close to the Fermi surface, CPGE response will reflect intraband transitions related to anomalous velocity, i.e., the cross product of Berry curvature and electric field, called the nonlinear Hall effect. [17] It could be further studied by low frequency excitation, which is not suitable for the previous experiments.

3.3.3 Experimentally observed s-PGE current

The three parts of $\mathbf{j}_{sPGE}(r)$, i.e. $\mathbf{j}_{s-Inj}(r)$, $+\mathbf{j}_{s-Shift}(r)$ and $\mathbf{j}_{s-Ano}(r)$ have some similar characteristics but are related to very different physical mechanisms. Among the three types of currents, s-Inj produces a large CPGE current for inversion broken materials and does not have excitation energy constraints, so we attribute it as the origin of our experimental observation. As a result, the CPGE part of s-Inj current is regarded as the sCPGE current and is discussed in detail.

In summary, a general microscopic model has been developed to describe the observed s-PGE current. The general quantum kinetic equation is obtained from the equation of motion for the Wigner transformation for ρ, which includes the spatial inhomogeneity of ρ through the electric field driving term. Analogous to the injection current in a homogenous system, the derived steady state response functions of j_{sPGE} consist of $\rho^{(2)}$ which is quadratic in $\boldsymbol{E}$ and linear in $\boldsymbol{q}$, and the band diagonal velocity, $\mathbf{v}_{nn} = \frac{\partial \varepsilon_n(\mathbf{k})}{\partial \mathbf{k}}$, with $\varepsilon_n(\mathbf{k})$ being the energy of band n at Bloch momentum $\boldsymbol{k}$. We assume that the measured j_{sPGE} is dominated by electronic interband transitions due to the high photon energy of the excitation beam (about 1.65eV), the two terms that control the conductivity tensor β for $\mathbf{j}_{sCPGE}$ in Eqn 3.12 are:

$$\begin{aligned}\beta_{ilj,1} = \sum_{k,n,m} \frac{ie^3}{2\hbar^2}(\Gamma_{nm}(\omega) + \Gamma_{mn}(-\omega))(f_0(\varepsilon_m) - f_0(\varepsilon_n))\Omega^i_{nm}(k) \\ (v^l_{nn}v^i_{nn}\tau^2_{nn} - v^l_{mm}v^i_{mm}\tau^2_{mm})\end{aligned} \tag{3.24}$$

$$\beta_{ilj,2} = \sum_{k,n,m} \frac{e^3}{8\hbar}(\Gamma^2_{nm}(\omega) + \Gamma^2_{mn}(-\omega))(f_0(\varepsilon_m) - f_0(\varepsilon_n))\Omega^i_{nm}(k) \\ (v^l_{nn} + v^l_{mm})(v^i_{nn}\tau_{nn} - v^i_{mm}\tau_{mm}) \tag{3.25}$$

where $f_0(\varepsilon_n(\mathbf{k})$ is the Fermi-Dirac distribution, $\tau_{nn}(\mathbf{k})$ is the relaxation time of excited carriers in band n, $\Gamma_{nm}(\mathbf{k},\omega) = \frac{1}{\hbar\omega+\varepsilon_n-\varepsilon_m-\frac{i\hbar}{\tau_{nm}}}$, and $\Omega^i_{nm}(\mathbf{k}) = -i(R^j_{nm}R^k_{mn} - R^k_{nm}R^j_{mn})$ is derived from interband matirx elements of the non-diagonal Berry connection, $\mathbf{R}_{nm}(\mathbf{k})$. This quantity transform like the Berry curvature: $\Omega^i_{nm}(\mathbf{k}) = \Omega^i_{nm}(-\mathbf{k})$ under inversion symmetry and $\Omega^i_{nm}(\mathbf{k}) = -\Omega^i_{nm}(-\mathbf{k})$ under time reversal symmetry. Therefore, it is allowed only if time reversal or inversion symmetry is broken, which is in a good agreement with the observation.

Although the response functions have no symmetry restrictions, the dominating part (Eqn 3.24 and 3.25) would become vanishingly small under inversion symmetry. Therefore, the expressions explain why sCPGE does not exist in the inversion symmetric 1T' phase of $MoTe_2$ but arises only after a temperature or doping induced phase transition to the inversion broken T_d phase. Quantitively, $\mathbf{j}_{sPGE}$ magnitude is sensitive to the details of the band dispersion since these response functions carry two orders of the band diagonal velocities, and are also closely related to the band resolved Berry curvature $\Omega^i_{nm}(\mathbf{k})$ involved in optical transitions.

Unlike conventional injection current, momentum space asymmetry in the electron scattering rate is crucial for the existence of sCPGE since only the antisymmetric contribution to the relaxation time, $\tau_{nm}(-\mathbf{k})^{(a)} = -\tau_{nm}(-\mathbf{k})^{(a)}$ can give rise to nonzero β_1 or β_2. In general, the scattering probability function follows the crystal symmetry, [22] so an antisymmetric modulation of the relaxation time of $\boldsymbol{k}$ is allowed only in the broken inversion phase in these materials. Furthermore, when large spin-orbit coupling is present, spin-dependent skew scattering [23–25] of positive and negative $\boldsymbol{k}$ states occur with different probabilities, i.e. $W_{kk'} \neq W_{k'k}$, and would augment an isotropic scattering rate by an antisymmetric contribution which is the main contribution to $\tau_{nm}(\mathbf{k})^{(a)}$.

This microscopic description of the sCPGE response requires controlling the k-space distribution of excited electrons using optical field gradients, in contrast to conventional

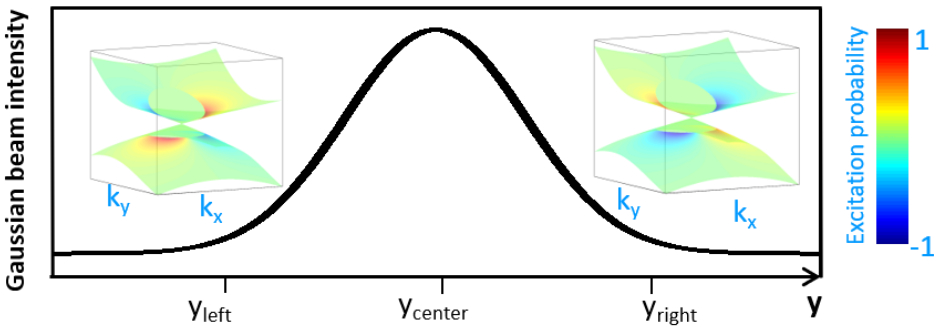

FIGURE 3.18: Schematic of asymmetric interband excitation by a Gaussian beam, where the band touching points are located along the x axis, and light propagates in the z direction. (Main) Spatial intensity distribution of a Gaussian beam along the y axis, with y_{center} being the y coordinate of the Gaussian beam center. (Inset) Local excitation patterns contributing to sCPGE current in the momentum space at the left (yleft) and right (yright) tails of the Gaussian beam. The color map shows the normalized difference between the excitation probability (nonequilibrium electron population) under right and left circularly polarized light illumination. A negative value (blue region) implies that in comparison to homogenous excitation, the optical field gradient results in less electrons being excited, while a positive value (red color) implies excitation of more electrons.

CPGE which uses only the polarization of a spatially uniform optical field. The effect is illustrated by a transition between the valence and conduction bands under Gaussian beam excitation, shown in Fig 3.18. The bands are colored by the difference of excitation probability (nonequilibrium electron population distribution) under RCP and LCP light, derived from the density matrix formalism. [29]

Contrary to the conventional CPGE where the electrons would be excited following the intrinsic distribution of $\Omega^i_{nm}(\boldsymbol{k})$, (Fig 3.18 inset), the excitation probability of sCPGE has an asymmetric component, which changes sign when the local $\boldsymbol{q}$ is reversed (i.e. on the opposite side of the Gaussian beam), showing that the interaction of the bands with the optical field can be controlled by the beam profile. The measured positive correlation between sCPGE and temperature (Fig 3.7), which differs from most conventional CPGE [26], is a novel feature that arises from this unique microscopic mechanism.

Overall, the sCPGE response in $MoTe_2$ and $Mo_xW_{1-x}Te_2$ expressed in terms of $\Omega^i_{nm}(\boldsymbol{k})$ is allowed by the broken inversion symmetry and is related to a large spin-orbit interaction (SOI) in Weyl semimetals. [27] This naturally raises a question about

the effect of band crossings in a Weyl semimetal on sCPGE. To study the sCPGE at low frequency excitations below Lifshitz energy near the Weyl cone, 6um laser was performed for photocurrent measurements in the next section.

3.3.4 Minimal model at low energy excitation

To understand the sCPGE behaviour at low energy excitation, we calculated our response functions using a minimal model describing a three dimensional Dirac semimetal. By studying how it changes upon phase transition between two typical topological phases (from Dirac to Weyl semimetal, accompanied with inversion symmetry breaking, which is similar to out experiments), we can extract more fundamental physical insights into the origin of this novel sCPGE. The Hamiltonian describing a three dimensional Dirac semimetal is adopted by a A_3Bi (A=Na, K, Rb) system. [28] Taking into account the spin orbit coupling, the orbitals considered are $|S^+_{\frac{1}{2}}, \frac{1}{2}>$, $|P^-_{\frac{3}{2}}, \frac{3}{2}>$, $|S^+_{\frac{1}{2}}, -\frac{1}{2}>$, $|P^-_{\frac{3}{2}}, -\frac{3}{2}>$ and the leading order Hamiltonian around Γ point is:

$$H_\Gamma(k) = \varepsilon_0(k) + \begin{pmatrix} M(k) & Ak_+ & 0 & B^*(k) \\ Ak_- & -M(k) & B^*(k) & 0 \\ 0 & B(k) & M(k) & -Ak_- \\ B(k) & 0 & -Ak_- & -M(k) \end{pmatrix} \tag{3.26}$$

where $k_\pm = k_x \pm ik_y$, $\varepsilon_0 = C_0 + C_1k_z^2 + C_2(k_x^2 + k_y^2)$, $M(k) = M_0 - M_1k_z^2 - M_2(k_x^2 + k_y^2)$, and $B(k) = b_3k_zk_+^2$, which is taken to be zero. Two fold degenerate bands form two Dirac points at $(0, 0, \sqrt{\frac{M_0}{M_1}})$ along the $\hat{k}_z$ axis (Fig 3.19). Because of the time reversal and inversion symmetry, $\Omega^{ij}_{nm}(k)$ is zero, and all relevant terms in sCPGE vanished.

Now we add a small inversion breaking term controlled by the parameter L_0 to break the inversion symmetry:

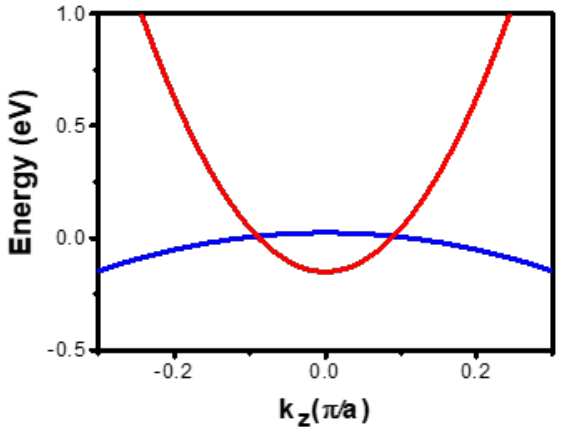

FIGURE 3.19: Band structure of a Dirac semimetal [29]

$$\begin{aligned} H'_\Gamma(k) &= H_\Gamma(k) + L_0 k_z \sigma_z \otimes \tau_z \\ &= H_\Gamma(k) + L_0 k_z \cdot \begin{pmatrix} 1 & 0 & 0 & 0 \\ 0 & -1 & 0 & 0 \\ 0 & 0 & -1 & 0 \\ 0 & 0 & 0 & 1 \end{pmatrix} \end{aligned} \tag{3.27}$$

where $TH'_\Gamma(k)T^{-1} = H'_\Gamma(k)$ and $IH'_\Gamma(k)I^{-1} \neq H'_\Gamma(k)$. The system then becomes an inversion broken Weyl semimetal with broken inversion symmetry. This Weyl semimetal has four Weyl points separated along the $\hat{k}_z$ axis. (Fig 3.20) The nonvanishing $\Omega^i_{nm}(k)$ produces a nonzero J_{sCPGE} and the transverse part of the conductivity, σ_{zyx}. This conductivity matrix can be plotted as a function of frequency. It describes the case where the electric field of circularly polarized light lies in the y-z plane, and the transverse CPGE current is collected along z axis. The frequency dependence shows linear behavior at low frequency and $\frac{1}{\omega^2}$ dependence at high frequencies, which can be fitted by

$$\sigma_{zyx}(\omega) = \frac{\alpha\omega + \alpha'\omega^2}{1 + \beta\omega^3 + \beta'\omega^4} \tag{3.28}$$

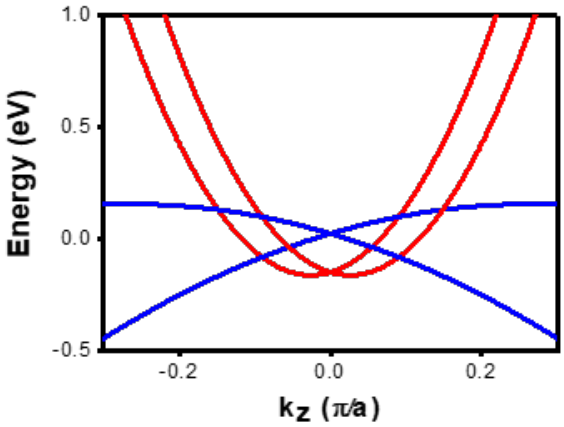

FIGURE 3.20: Band structure of the inversion broken Weyl semimetal obtained from Fig3.19 by adding an inversion breaking term from Eqn.3.27 [29]

where $\alpha, \alpha', \beta, \beta'$ are the coefficients. The response function suggests that:

$$\sigma_{zyx}(\omega) \sim \sum_k \Omega(k) v(k)^2 (\Gamma^2_{mn}(\omega) + \Gamma^2_{mn}(-\omega)) \tag{3.29}$$

where $\Gamma^2_{mn}(\omega) + \Gamma^2_{mn}(-\omega)$ can be expanded in powers of $\frac{\omega}{\Delta E(k)}$. [29] The low and high frequency scaling behaviour can be rationalized as follows. In the low frequency regime, due to the Pauli blocking, $\Omega(k)v(k)^2 \sim 1$, $\Delta E(k) \sim k > \omega$. The dominating expansion term in $\frac{\omega}{\Delta E(k)}$ is linear to ω, so $\sigma_{zyx}(\omega)$ is linear to ω and the slope is determined by a k space integral: [29]

$$\int dk \frac{\Omega(k)v(k)^2}{(\Delta E(k) - \frac{i}{\tau})^3} \tag{3.30}$$

For the high frequency regime, the k space integral can be divided into three parts, determined by two boundaries k' and k^*. k' defines the small k regime so that when $k > k'$, the high frequency scaling $\omega(k) \sim \frac{1}{k^2}$, $v(k) \sim k$ and $\Delta E(k) \sim k^2$ can be used. k^* is derived from $\omega = \Delta E(k^*)$. When $k < k^*$, the expansion of $\Gamma^2_{mn}(\omega) + \Gamma^2_{mn}(-\omega)$ is still in powers of $\frac{\Delta E(k)}{\omega}$ but when $k > k^*$, the expansion is in Taylor series of $\frac{\omega}{\Delta E(k)}$. The response would be dominated by the second (intermediate k) and the third (large k) k space integrals. The second integral in leading orders of ω is proportional to $\frac{a_1}{\omega^{\frac{3}{2}}} + \frac{a_2 k'}{\omega^2}$ and the third integral is proportional to $\frac{a_3}{\omega^{\frac{3}{2}}}$, where a_1, a_2, a_3 are constants. For our continuum

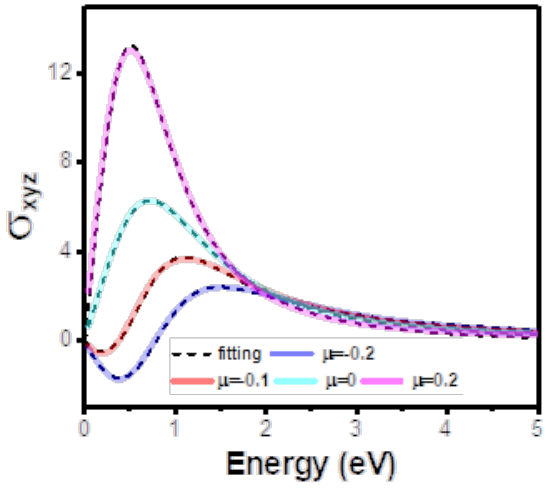

FIGURE 3.21: Plots of the transverse sCPGE conductivity σ_{zyx} of the Weyl semimetal as a function of optical frequency, ω at different Fermi energies and fittings to the scaling function Eqn 3.28. [29]

model we employ a numerical large k cutoff so that $\frac{a_1}{\omega^{\frac{3}{2}}} < \frac{a_2 k'}{\omega^2}$, leading to an overall integral scaled as ω^{-2} at high frequency. [29]

For comparison, conductivity of conventional CPGE current, described by:

$$A_{ijk}(\omega) \sim \sum_k \Omega(k) v(k) (\Gamma_{mn}(\omega) + \Gamma_{nm}(-\omega)) \tag{3.31}$$

is plotted as a function of frequency. (Fig 3.22) The conductivity, $A_{zyz}(\omega)$, is calculated for the same external field and current direction. Different from sCPGE, the frequency dependence shows $\frac{1}{\omega}$ dependence at high frequency, and can be fitted by:

$$A_{zyz}(\omega) = \frac{\lambda\omega}{1+\delta\omega^2} + \frac{\lambda'\omega^2}{1+\delta'\omega^3} \tag{3.32}$$

where $\lambda, \lambda', \delta, \delta'$ are the coefficients. [29]

The behavior of the frequency dependence is significantly different between conventional CPGE and sCPGE. Other than the $1/\omega$ scaling at high frequency, the conductivity of conventional CPGE will keep the same sign at certain Fermi energy. However, when the Fermi level is less than the Lifshitz energy, σ_{zyx} changes its sign at a certain

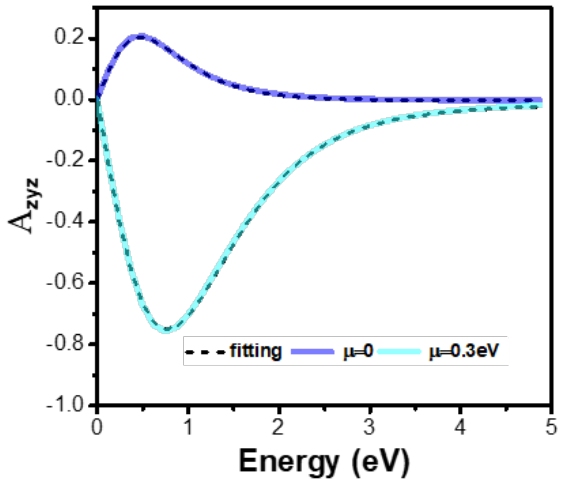

FIGURE 3.22: Plots of the CPGE conductivity A_{zyz} of the Weyl semimetal as a function of optical frequency, ω at different Fermi energies along with the fits to Eqn. 3.32, to compare with sCPGE. [29]

frequency determined by the chemical potential, which is related to band crossing in Weyl semimetal. Upon increasing the inversion breaking parameter L_0, the initial slope α gradually increases, leading to a stronger sCPGE (Fig 3.23).

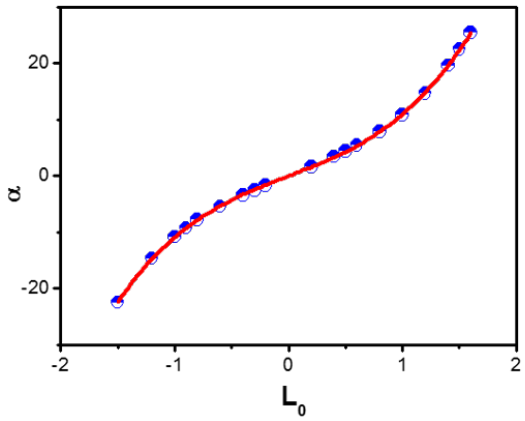

FIGURE 3.23: Plots shows the dependence of the fitting parameter α on the inversion breaking parameter L_0, at the Fermi energy $\mu = 0.3eV$. [29]

For our system, the Fermi energy of $MoTe_2$ is intrinsically below the Weyl points. As

illustrated by this minimal model analysis, when changing the excitation energy from high frequency to low frequency, the conductivity has a sign reversal. Also, since the sCPGE conductivity is weighted by the relaxation and velocity terms, the sign reversal would happen at a higher energy than Lifshitz scale, which means the CPGE sign is expected to be opposite at 750nm and at 6um excitation. This model is in good agreement with the experimental results of Fig 3.16

3.4 Conclusion

In conclusion, a strong spatially dispersive CPGE with photon helicity dependent circulating photocurrent is observed in type-II Weyl semimetal $MoTe_2$ and $Mo_xW_{1-x}Te_2$ (x=0.3, 0.9). Different from conventional CPGE, this sCPGE current is circulating around the beam center and the amplitude is affected by the gradient of the beam profile. The sCPGE current properties are confirmed by multi-electrode measurements and beam size dependence experiments. Besides, sCPGE can only be measured in the inversion symmetry breaking Weyl phase via the experiment on $MoTe_2$ phase transition.

The newly derived nonlinear susceptibilities encode the effects of spatially inhomogeneous field excitation and explain the existence of sCPGE in Weyl semimetals. In this framework, these effects are attributed to the inversion symmetry breaking and asymmetric carrier excitation in momentum space due to optical field gradients. The frequency dependence is another significant difference between sCPGE and conventional CPGE. The polarity is opposite when excitation energy changes from high energy to low energy, which is related to the band crossing.

Overall, since sCPGE shows a different scaling behavior in comparison to conventional CPGE at high frequency and is sensitive to detailed band parameters and topology at low frequency, sCPGE may be a very useful spectroscopic probe of topological materials. More generally it can be applied to control photogalvanic response via the patterning of light intensity distribution and polarization, broadening the application of conventional photogalvanic effect by providing an additional degree of freedom that

can be experimentally accessed. Our work also demonstrates that precisely tailored photon spin-dependent optoelectronic responses can be engineered in these systems by shaping and patterning optical field profiles, which can greatly enhance the applications of topological materials over a broad spectral range.

Bibliography

[1] Ivchenko E., Ganichev S. Spin Physics in Semiconductors. Springer; 2008.

[2] Ganichev S. D., Prettl W.; Spin photocurrents in quantum wells; Journal of physics: Condensed matter 15 (20), R935 (2003).

[3] Shalygin V., Moldavskaya M., Danilov S., Farbshtein I., Golub L.; Circular photon drag effect in bulk tellurium; Physical Review B 93 (4), 045207 (2016).

[4] He X., Shen B., Chen Y., Zhang Q., Han K., Yin C., Tang N., Xu F., Tang C., Yang Z.; Anomalous photogalvanic effect of circularly polarized light incident on the two-dimensional electron gas in $Al_xGa_{1-x}N/GaN$ heterostructures at room temperature; Physical review letters 101 (14), 147402 (2008).

[5] Tang, Y.Q., Shen, B., He, X.W., Han, K., Tang, N., Chen, W.H., Yang, Z.J., Zhang, G.Y., Chen, Y.H., Tang, C.G. and Wang, Z.G.; Room-temperature spin-oriented photocurrent under near-infrared irradiation and comparison of optical means with Shubnikov de-Haas measurements in $Al_xGa_{1-x}N/GaN$N heterostructures. Applied Physics Letters, 91(7), p.071920 (2007).

[6] Ganichev, Sergey D., and Wilhelm Prettl; "Spin photocurrents in quantum wells." Journal of physics: Condensed matter 15.20 : R935(2003).

[7] Dyakonov, M. I., and V. I. Perel. "Current-induced spin orientation of electrons in semiconductors." Physics Letters A 35, no. 6 : 459-460(1971).

[8] Hirsch, J. E; Spin hall effect. Physical Review Letters, 83(9), 1834(1999).

[9] Hankiewicz, E. M., Jian Li, Tomas Jungwirth, Qian Niu, Shun-Qing Shen, and Jairo Sinova; "Charge Hall effect driven by spin-dependent chemical potential gradients and Onsager relations in mesoscopic systems." Physical Review B 72, no. 15 155305(2005).

[10] Wang Z., Gresch D., Soluyanov A. A., Xie W., Kushwaha S., Dai X., Troyer M., Cava R. J., Bernevig B. A.; MoTe 2: a type-II Weyl topological metal; Physical review letters 117 (5), 056805 (2016).

[11] Kaminski A.; Spectroscopic evidence for a type II Weyl semimetallic state in MoTe2, (2016).

[12] Ivchenko E., Ganichev S. Spin Physics in Semiconductors. Springer; 2008.

[13] Belinicher V., Sturman B.; The photogalvanic effect in media lacking a center of symmetry; Physics-Uspekhi 23 (3), 199-223 (1980).

[14] Sipe J., Shkrebtii A.; Second-order optical response in semiconductors; Physical Review B 61 (8), 5337 (2000).

[15] Sekine A., Culcer D., MacDonald A. H.; Quantum Kinetic Theory of the Chiral Anomaly; arXiv preprint arXiv:1706.01200, (2017).

[16] von Baltz R., Kraut W.; Theory of the bulk photovoltaic effect in pure crystals; Physical Review B 23 (10), 5590 (1981).

[17] Sodemann I., Fu L.; Quantum nonlinear Hall effect induced by Berry curvature dipole in time-reversal invariant materials; Physical Review Letters 115 (21), 216806 (2015).

[18] Deyo E., Golub L., Ivchenko E., Spivak B.; Semiclassical theory of the photogalvanic effect in non-centrosymmetric systems; arXiv preprint arXiv:0904.1917, (2009).

[19] Bieler M., Pierz K., Siegner U., Dawson P.; Shift currents from symmetry reduction and Coulomb effects in (110)-orientated $GaAs/Al_{0.3}Ga0.7$ As quantum wells; Physical Review B 76 (16), 161304 (2007).

[20] König E., Xie H.-Y., Pesin D., Levchenko A.; Photogalvanic effect in Weyl semimetals; Physical Review B 96 (7), 075123 (2017).

[21] Wang Z., Sun Y., Chen X.-Q., Franchini C., Xu G., Weng H., Dai X., Fang Z.; Dirac semimetal and topological phase transitions in A_3Bi (A= Na, K, Rb); Physical Review B 85 (19), 195320 (2012).

[22] Olbrich P., Golub L., Herrmann T., Danilov S., Plank H., Bel'kov V., Mussler G., Weyrich C., Schneider C., Kampmeier J.; Room-temperature high-frequency transport of Dirac fermions in epitaxially grown Sb 2 Te 3-and Bi 2 Te 3-based topological insulators; Physical review letters 113 (9), 096601 (2014).

[23] Hirsch J.; Spin hall effect; Physical Review Letters 83 (9), 1834 (1999).

[24] Rubin L., Sample H. The Hall Effect and Its Applications, edited by CL Chien and CR Westgate. Plenum, New York; 1980.

[25] Deyo E., Golub L., Ivchenko E., Spivak B.; Semiclassical theory of the photogalvanic effect in non-centrosymmetric systems; arXiv preprint arXiv:0904.1917, (2009).

[26] McIver J., Hsieh D., Steinberg H., Jarillo-Herrero P., Gedik N.; Control over topological insulator photocurrents with light polarization; Nature nanotechnology 7 (2), 96 (2012).

[27] Tamai A., Wu Q., Cucchi I., Bruno F. Y., Ricco S., Kim T., Hoesch M., Barreteau C., Giannini E., Besnard C.; Fermi arcs and their topological character in the candidate type-II Weyl semimetal MoTe 2; Physical Review X 6 (3), 031021 (2016).

[28] Wang Z., Sun Y., Chen X.-Q., Franchini C., Xu G., Weng H., Dai X., Fang Z.; Dirac semimetal and topological phase transitions in A_3Bi (A= Na, K, Rb); Physical Review B 85 (19), 195320 (2012).

[29] Ji, Z., Liu, G., Addison, Z., Liu, W., Yu, P., Gao, H., Liu, Z., Rappe, A.M., Kane, C.L., Mele, E.J. and Agarwal, R., 2018. Spatially dispersive circular photogalvanic effect in a Weyl semimetal. arXiv preprint arXiv:1802.04387.

Chapter 4

Photo Induced Anomalous Hall Effect in Weyl Semimetal

4.1 Introduction

4.1.1 Ordinary Hall Effect

In 1879, Edwin H. Hall made a momentous discovery that voltage difference can be observed across an electrical conductor in the transverse direction of the electric current in the conductor when a magnetic field is applied perpendicular to the current. [1] This effect comes from the nature of current in a conductor. (Fig 4.2) When a magnetic field is present, the carriers, such as electron and hole, will experience the Lorentz force whose direction is vertical to the plane of magnetic field and current. The carriers, pressed by this force, would accumulate at the side of the conductor and build up an electric field, which is measured as Hall voltage.

The Hall voltage can be written as $V_H = \frac{I_x B_z}{ned}$ and Hall coefficient is defined as $R_H = \frac{E_y}{j_x B_z} = \frac{V_H d}{IB} = -\frac{1}{ne}$, which is only dependent on the carrier density. This effect provides a simple but useful tool to measure the carrier concentration in nonmagnetic conductors and motivate the development of semiconductor physics and solid-state electronics, which was honoured as the queen of solid-state transport experiments.

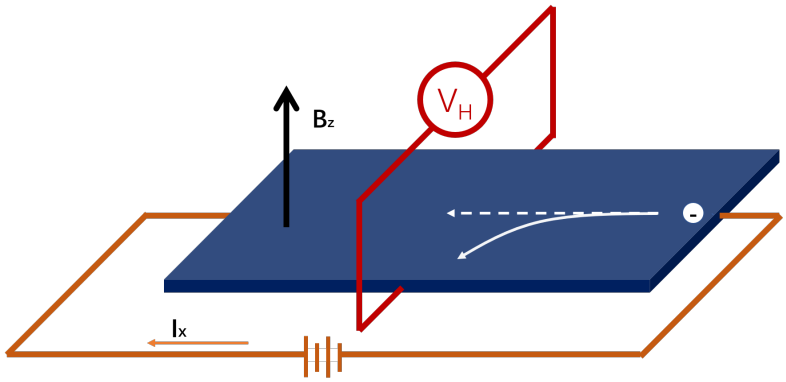

FIGURE 4.1: Schematic interpretation of ordinary Hall effect in conductor. Hall voltage V_H can be measured in y direction when external electric field is applied in x direction and meganatic field in z direction.

4.1.2 Anormalous Hall Effect in Ferromagnetic Materials

Few years later, this effect measured in ferromagnetic iron was found to be ten times larger than in nonmagnetic conductors that was known as the anomalous Hall effect. [2] The theoretical and experiential study on the AHE has been last for almost a century, and recently, the core concepts was given out. Different from the linear dependence of the Hall resistivity ρ_{xy} on the field H_z in ordinary Hall effect, ρ_{xy} in ferromagnetic materials increases steeply and saturates at large field and can be written as: [3–7]

$$\rho_{xy} = R_0 H_z + R_s M_z \tag{4.1}$$

whereH_z is the applied perpendicular field and M_z is the magnetization. R_0 in the first term is known to be dependent on the carrier density, while R_s in the second term is unclear. In the following decades, the theory of AHE was controversial since several explanations were raised in different views to describe the properties of this effect. Karplus and Luttinger (KL) came up with the "anomalous velocity" theory that was perpendicular to the electric field contributing to the Hall effect, which gives a relationship of $\rho_{xy} \sim \rho^2$. [8] Because this mechanism is independent on scattering, it is named as intrinsic contribution.

On the other side, some theories which focused on the disorder scattering argued

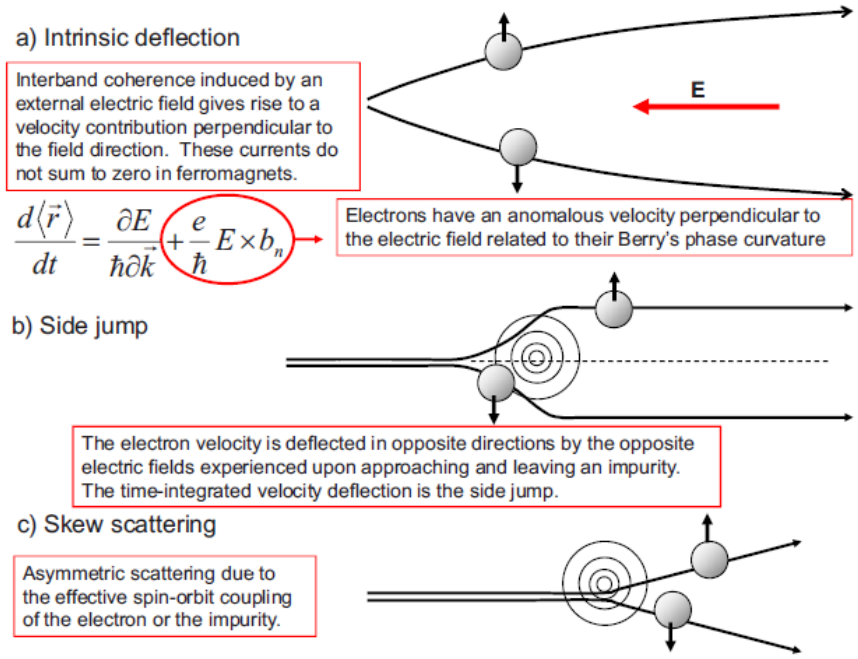

FIGURE 4.2: Three main origin of the AHE current: intrinsic, side jump and skew scattering. In any real material all of these mechanisms act to influence electron motion. Reprinted figure with permission from reference [12] Copyright (2019) by the American Physical Society.

that skew scattering caused by spin orbit interaction concluded that extrinsic contribution was the main source, suggesting $R_s \sim \rho_{xx}$. [9, 10] Another external contribution, side-jump origin, was presented in 1970 by Berger who treated the AHE current as the product of the side jump per scattering event. [11] This theory gave another different power relationship: $R_s \sim \rho_{xx}^2$.

With the development of concepts about topology and geometry, the intrinsic contribution was realized to come from the Berry phase supported anomalous velocity. [12–16] According to Bloch's theorem, the wave function for n^{th} band:

$$|\Phi_n(\boldsymbol{k},\boldsymbol{r})> = e^{i\boldsymbol{k}\cdot\boldsymbol{r}}|u_n(\boldsymbol{k},\boldsymbol{r})> \tag{4.2}$$

where $|u_n(\boldsymbol{k},\boldsymbol{r}) >$ has the lattice periodicity. The Bloch electron group velocity is expressed by:

$$v = \frac{\partial \varepsilon_n}{\hbar \partial k} - \dot{k} \times \Omega_n \tag{4.3}$$

$$\dot{k} = -\frac{e}{\hbar}(E + \dot{r} \times B) \tag{4.4}$$

where Ω is the Berry curvature. The Berry curvature of band n is described by:

$$\Omega_n = -Im\langle \frac{\partial u_n}{\partial k}| \times |\frac{\partial u_n}{\partial k}\rangle \tag{4.5}$$

The second term in Eqn 4.3 is zero when both time reversal and spatial inversion symmetry are preserved, which lead to zero Berry curvature. However, with non zero Berry curvature, the direction of this term is perpendicular to the electric field $\boldsymbol{E}$ without external magnetic field $\boldsymbol{B}$, giving a transverse component of the velocity. Therefore, by adding up this term over all occupied states, the AHE can be defined as:

$$\sigma_{AH} = \frac{e^2}{\hbar} \sum_n \int \frac{dk}{(2\pi)^3} f(\varepsilon_n(k)) \Omega_n \tag{4.6}$$

where $f(\varepsilon_n(k))$ is the Fermi-Dirac distribution function. In ferromagnetic system, the time reversal symmetry is broken. With SOI that couple the spin up and spin down bands, a non zero Hall current can be derived. [17] Therefore, AHE can be obtained in systems with broken time reversal symmetry as a consequence of spin-orbit coupling, such as in ferromagnetic materials.

4.1.3 Photo induced Anormalous Hall Effect

Is it possible to observe AHE in non-ferromagnetic materials with time reversal symmetry? Recently, photoinduced anomalous Hall effect has been theoretically predicted [18] and experimentally observed in quantum wells [19–21]. There is very strong

Rashba spin orbit coupling (SOC) existing in the quantum well, such as the InGaAs/AlGaAs, $Al_{0.25}Ga_{0.75}N/GaN$ heterostructures or n-type GaAs bulk. When circularly polarized light is incident in z direction and an external electric field is applied in x direction, a Hall current can be generated in y direction, written as: $J = \sigma_{xy}\lambda E \times e_p$, where e_p is the Poynting unit vector and $\lambda = \pm 1$ represents the helicity of the light. For symmetry argument, with the time reversal symmetry broken by the circularly polarized light, the non zero Berry curvature leads to the AHE current. As measured in $Al_{0.25}Ga_{0.75}N/GaN$ heterostructures by CM Yin [22], the AHE current contribution could be obtained by fitting the total photoccurent. Under different longitudinal electrical fields, the AHE current changed linearly with varied filed, suggesting anomalous Hall conductivity to be $\sigma_{AH} = 9.0 \times 10^{-10}\Omega^{-1}$ (Fig. 4.3).

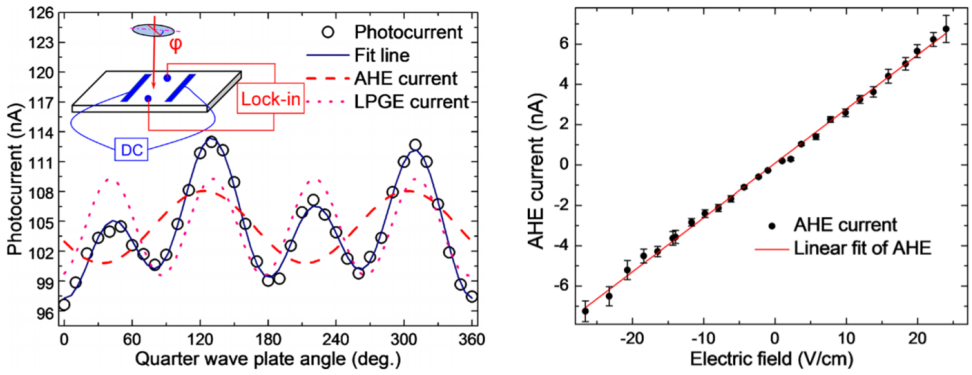

FIGURE 4.3: (left) The total photocurrent measured under the longitudinal electric field of 20 V/cm in an $Al_{0.25}Ga_{0.75}N/GaN$ heterostructure. The current is fitted in to the equation: $j = j_{AHE}sin2\varphi + j_L sin2\varphi cos2\varphi + j_0$. (right) The amplitude of the photoinduced AHE current as a function of the longitudinal electric field in an $Al_{0.25}Ga_{0.75}N/GaN$ heterostructure. The solid line is the linear fit. Reprinted figure with permission from [22]

As mentioned before, the CPGE requires centrosymmety to be broken. In the photoinduced AHE experiments, the transverse electric field breaks the in-plane symmetry. In the system whose CPGE is forbidden by symmetry, CPGE current can be obtained by applying transverse field. Under same illumination, CPGE current has opposite direction when the transverse filed changes sign. This so called "helicity-dependent photocurrent induced by the in-plane transverse electric current" was reported in an InAs

quantum well. [23] The CPGE current was observed to be proportional to the transverse bias voltage.

Weyl semimetals consist of large spin orbit coupling was considered as a promising candidate for AHE. Besides, since the Weyl semimetal breaks time reversal symmetry or inversion symmetry, the Berry curvature is non zero. Obviously, if the splitting of the Weyl points is due to time reversal symmetry breaking, which is ferromagnetic Weyl semimetal, the intrinsic AHE was expected and was calculated. [24] However, for the other class of Weyl semimetal, such as the $MoWTe_2$ family, the time reversal symmetry is preserved but the inversion symmetry is broken. Time reversal symmetry needs to be broken for non-zero AHE current.

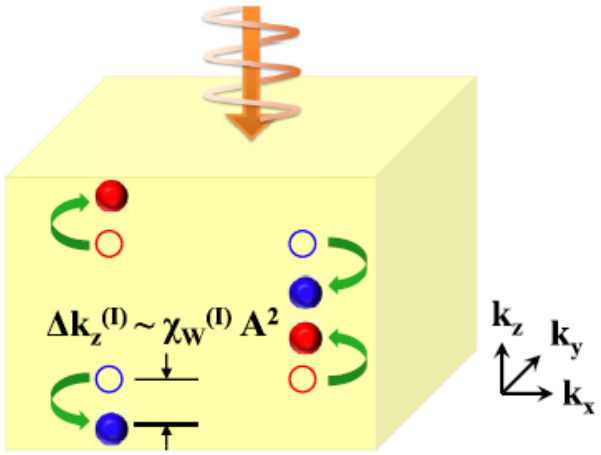

FIGURE 4.4: Schematic figure for a Weyl semimetal in momentum space under illumination of circular polarized light. Blue and red circles are Weyl nodes with opposite chiralities $\chi_W^{(I)}$. The node position are shifted by the photons in a chirality-dependent manner and the shift is proportional to A^2. The overall nonzero Chern vector shift, $\delta v_k = \sum_I \chi_W^{(I)} \cdot \delta q_k^{(I)} \neq 0$, will result in photo induced anomalous Hall conductivity. Reprinted figure with permission from reference [25] Copyright (2019) by the American Physical Society.

In 2016, the theory for photoinduced anomalous Hall effects in Weyl Semimetals was proposed. [25] In that work, AHE was proven to generally present in all Weyl systmes when coupled to a CP light source, even though AHE was intrinsically absent

in some typical Weyl materials for symmetry reason. Through a general tight - binding model analysis, Weyl node positions were calculated to be shifted by the circularly polarized light and the shift was proportional to A^2, where A was the electromagnetic wave amplitude. (Fig 4.4) The electronic transport property would be changed because of the Weyl node shift. For all Weyl nodes, the change of the anomalous Hall conductivity was written as:

$$\delta\sigma_{ij} = \frac{e^2}{2\pi\hbar}\epsilon_{ijk}\delta v_k \tag{4.7}$$

and δv_k was the change of the Chern vector:

$$\delta v_k = \sum_I \chi_W^{(I)} \cdot \delta q_k^{(I)} \tag{4.8}$$

where $q_k^{(I)}$ was the momentum shifts and the $\chi_W^{(I)}$ was the chirality of the Weyl node. Even though the total momentum shift was zero, the sum of Chern vector shift had finite value, leading to the A^2 order AHE current, meaning a Hall current proportional to the light intensity.

It can also be explained by symmetry argument. For Weyl semimetals breaking time reversal symmetry and preserving inversion, the momentum shift of a pair of nodes had the relation: $\delta q_k^{(1)} = -\delta q_k^{(2)}$. The two nodes with opposite chiralities would produce the same Chern vector change: $\chi_W^{(I)} \cdot \delta q_k^{(I)}$ and contribute to the Hall conductivity together. On the contrary, in the Weyl system breaking the inversion symmetry and keeping the time reversal symmetry, $\delta q_k^{(1)} = \delta q_k^{(2)}$ and $\chi^{(1)} = \chi^{(2)}$. The Chern vector change would have the same non zero result.

According to the analysis above, observable AHE is expected in the type-II Weyl semimetals by exciting the electrons with chiral light. Since the experimental study is still absent, the work in this chapter focused on this photoinduced AHE in type-II Weyl semimetal $MoWTe_2$ family. Due to the symmetry of this material, the conventional CPGE is forbidden under normal incident light, which means that this is also an electric field induced helicity-dependent photocurrent effect. More interestingly, the

topological phase transition property of $MoTe_2$ provides with more degree of freedom to analyze this effect via comparing the phenomenon in two phases.

4.2 Experimental Setup

A wavelength tunable Ti - Sapphire pulsed laser working at 750 nm was used as light source in experiments. The laser was focused to a Gaussian profile by a 60X objective and the spot size was about 2 um diameter 10 mW power. The light polarization was controlled by a polarizer and a quarter wave plate installed on a motorized precision rotation stage driven by a servo motor. (Fig. 4.5) The polarization quality has been checked by the method stated in the Chapter 2. Photocurrents were recorded using a current pre-amplifier (DL instruments model 1211) for which the voltage bias was sourced and the output signal from the pre-amplifier (photocurrent was converted to an amplified voltage signal) recorded continuously (10 data points per second) by the PCI card (National Instrument, NI PCI-6281). The time constant of the pre-amplifier was chosen to be 300 ms for lower noise level. The quarter wave plate was rotated at a fixed rate using a motorized precision rotation stage with a servo motor.

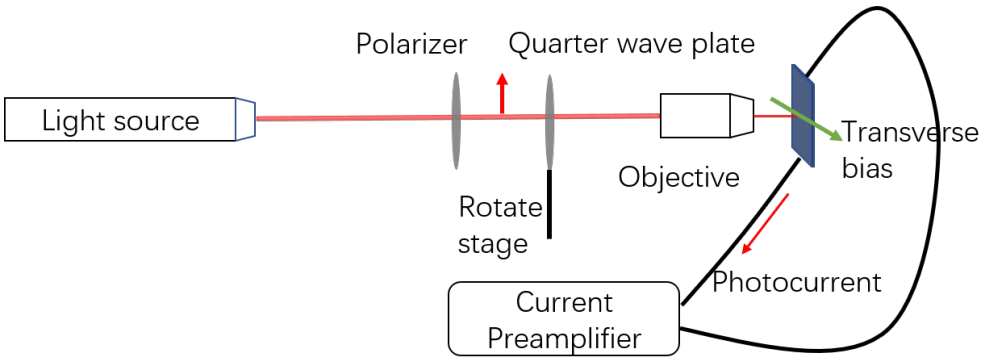

FIGURE 4.5: Optical and electrical setup for the Hall measurement. Polarization of 750 nm wavelength light is controlled by a polaizer and a quarter wave plate. The light is focused by an 60x objective lens and normal incident on the sample plane. Photocurrent is measured by a pre-amplifier while the sample can be applied transverse bias voltage.

The bulk crystal $Mo_{0.9}W_{0.1}Te_2$ and $MoTe_2$ was provided by Zheng Liu's group, same

as in Chapter 2. The sample was exfoliated to $\sim$ 20 um $\times$ 20 um flake and transferred onto Si/SiO_2 substrate. The crystallographic c axis of $MoTe_2$ was aligned to be parallel to the the z axis which was the normal incident light direction as shown in Fig 4.5. The electric contact was fabricated by the E-beam lithography and physical vapor deposition of Ti/Cu with total thickness equal to 500 nm.

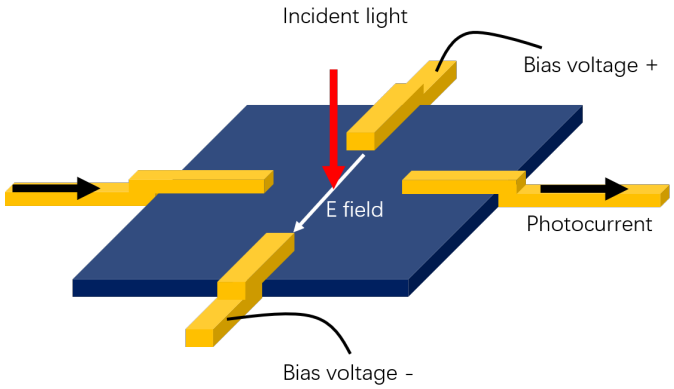

FIGURE 4.6: Schematic figure of the device for Hall effect measurement. Light is normally illuminated on the center of the sample to generate photocurrent which and be collected by a pair of electrodes. Transverse bias voltage is applied by the other pair of electrodes in perpendicular direction.

Four electrodes were symmetrically arranged in four orientations as a cross geometry for Hall measurements (Fig 4.6). While bias voltage was applied by a pair of electrodes, photocurrent were collected by another pair of electrodes in the transverse direction. The light was illuminated at the center of the sample to avoid the sCPGE effect induced by Gaussian profile discussed in Chapter 2 and 3. At fixed bias voltage, while rotating the quarter wave plate , photocurrent was measured as function of the quarter wave plate rotation angle ϕ. If the time reversal symmetry can be broken by the circularly polarized light, anomalous Hall current was expected to be obtained in this experiment, and the current direction should be opposite under different light helicity. Besides, photoinduced AHE current would be measured in $MoTe_2$ at both room temperature 1T' phase and 77 K Weyl phase for comparison.

4.3 Results and Discussion

Firstly, AHE measurements were carried out at room temperature Weyl semimetal $Mo_{0.9}W_{0.1}Te_2$. The photocurrent was obtained while the bias voltage was applied and plotted as the the function of quarter wave plate angle. The result was fitted to the phenomenological equation to get the current contribution from circular polarized light:

$$J = J_C sin(2\phi) + J_L sin(4\phi + \phi_0) + J_0 \tag{4.9}$$

As shown in Fig 4.7, at zero bias, the photocurrent at right and left circular polarized light showed same amplitude, indicating negligible CPGE. With the knowledge of sCPGE discussed in previous chapters, this result was as expected because the geometry symmetry was not broken when the beam was focus at the electrodes center.

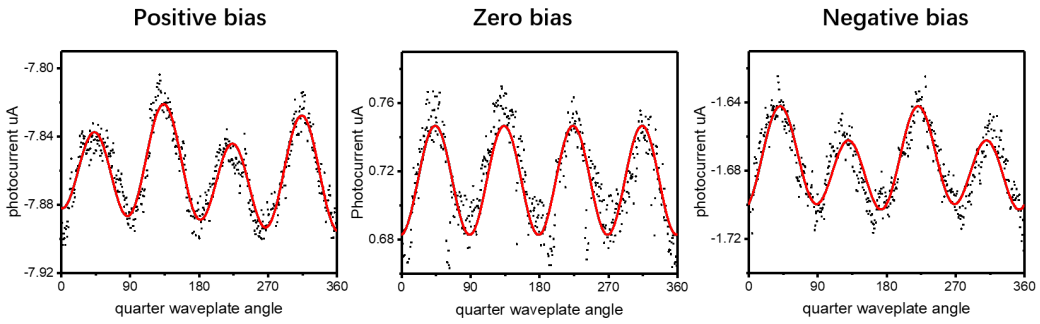

FIGURE 4.7: Under certain transverse bias voltage, photocurrent on $Mo_{0.9}W_{0.1}Te_2$ flake is measured while rotating the quarter wave plate and plotted as function of rotation angle ϕ. From left to right, the condition is positive bias, zero bias and negative bias respectively. The black dots are the experimental data and the red curves are the fitting function by the phenomenological equation.

Under transverse bias, CPGE was obtained in the same sample. At positive bias (8 mV), photocurrent at right circular polarized light ($\phi = 135°, 315°$) was higher than at left circular polarized light ($\phi = 455°, 25°$); while at negative bias (-17 mV), photocurrent at right circular polarized light was lower than at left circular polarized light. Through fitting into the Eqn 4.9, the amplitude of CPGE J_C can be extracted, which was 9.92 nA at positive voltage and 10.13 nA at negative voltage. It was an obvious

signal that the CPGE appeared under transverse bias voltage and the CPGE current direction was opposite for positive and negative bias. The reason why the same CPGE currents were observed at two different bias was the existence of fringe field in the device, which could be owning to the narrow width of the electrodes for transverse bias and the imperfect sample geometry.

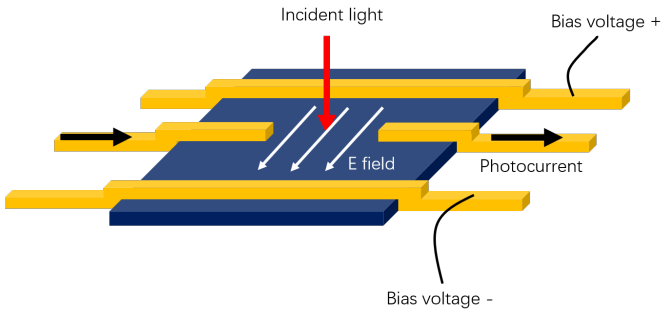

FIGURE 4.8: To avoid the influence of fringe field, two parallel electrodes are patterned for applying bias instead of crossing shape. The electric field in the center regime of the sample is considered to be perpendicular to the photocurrent measurement direction.

To improve the measurement, two parallel electrodes were patterned through the sample to minimize the field in other direction as shown in Fig 4.8. Two electrodes for photocurrent measurement were pattern near the center of the sample flake separated by 5 um. This pattern guaranteed that the electric field within the measurement area was almost parallel. Another Weyl semimetal $Mo_{0.9}W_{0.1}Te_2$ flake was used in this measurement and process was similar as before, while the positive bias and negative bias were same amplitude, 3 mV. The results were given in the Fig 4.9.

Same as the previous results, photocurrent at right circular polarized light ($\phi = 135°, 315°$) was higher than at left circular polarized light; while at negative bias, it was opposite, indicating the CPGE current induced by transverse bias. Additionally, comparing the CPGE current direction shown in Fig 4.7, the CPGE at two flakes had the same CPGE current direct if the bias and light helicity were the same, suggesting a robust effect that caused by the intrinsic property of the material.

Before discussion of further experiments studying properties of AHE, we needed to

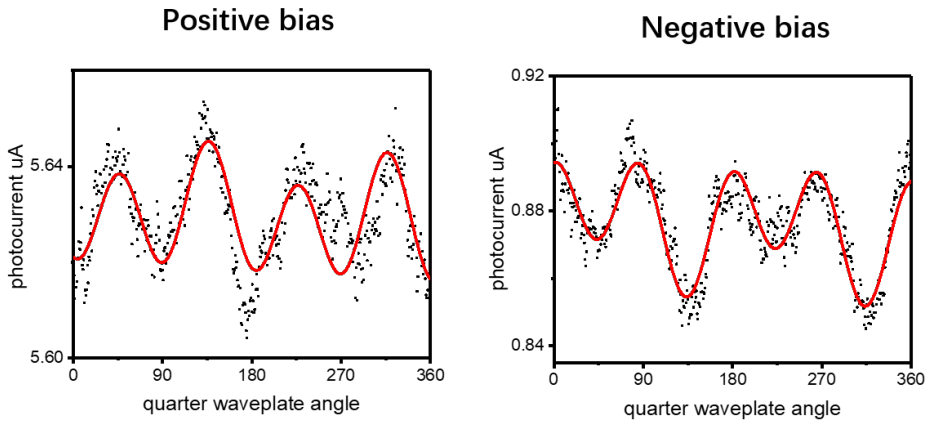

FIGURE 4.9: Under positive and negative bias voltage applied by parallel electrodes, photocurrent on $Mo_{0.9}W_{0.1}Te_2$ flake is measured while rotating the quarter wave plate and plotted as function of rotation angle ϕ in the left and right figure respectively. The black dots are the experimental data and the red curves are the fitting function by the phenomenological equation.

ensure that these photocurrent experiments were performed within the linear regime of the light power. Measurements were carried out at various incident beam intensity by adjusting optical density filters. With fixed beam position and same bias voltage, photocurrent was measured during rotating the quarter wave plate and plotted as angle ϕ at each light intensity. CPGE current was extracted via fitting equation and corresponded to the incident laser power measured by power meter. As given in the Fig 4.10, CPGE current had linear relationships with excitation power in our measurement range.

To further explore the dependence of the photo induced CPGE current on the transverse bias voltage, CPGE current at various transverse bias was required to be obtained, instead of only positive and negative situations. However, during the attempt of the measurement on photocurrent under various bias voltage magnitude, we found that the resolution of the pre-amplifier was not high enough for current lower than 1nA scale, as the photoinduced CPGE current J_C was generally blow 10nA shown in previous results. Thus, it was not accurate to obtain the CPGE difference within small step of bias.

To lower down the electrical noise and improve data quality, optical chopper and

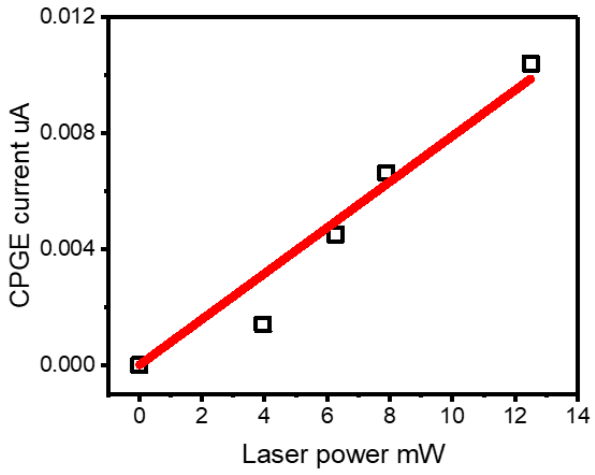

FIGURE 4.10: Dependence of CPGE current magnitude on 750 nm laser power.J_C is fitted to linear relationship with laser power.

lock-in amplifier were utilized in the measurement. The laser was chopped and illuminated on the sample at a certain speed (377 Hz in this work), which was provided to the lock-in amplifier as a reference frequency. Only the electrical signal with the reference frequency which was generated by the incident light, can be measured. The photocurrent was collected by the lock-in amplifier, while transverse bias voltage was applied by a source meter working at lower magnitude range (Keithley 2635).

Furthermore, according to the previous work on Chapter 2 and 3, the sCPGE current exists on the sample plane when the focused Gaussian beam is incident on the device. The reason why the CPGE is not measurable without bias is that the position of beam is at the center and geometry symmetric electrodes can not collect net signal from circulating current. Even though the signal is not measurable, the sCPGE is not forbidden in room temperature Weyl semimetal $Mo_{0.9}W_{0.1}Te_2$, which means that the sCPGE current is swirling around the beam during the measurement above. It naturally raises a hypothesis that the electric field acts as the driving force, pushing the carriers on the sample to be off center-and breaking the symmetry of the geometry. For instance, the carriers generated by the circular polarized light and circulating around the beam center is possible to be driven be the transverse electric field and shifted in

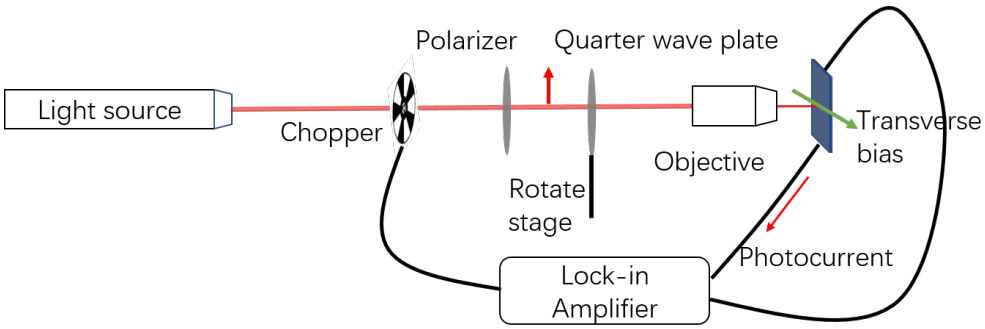

FIGURE 4.11: Optical and electrical setup for the Hall measurement. 750 nm wavelength light is chopped and controlled by a polaizer and a quarter wave plate. The light is focused by an objective and normal incident on the sample plane. Photocurrent is measured by a Lock-in amplifier while applied transverse bias voltage is applied.

the field direction, resulting in the situation that the carriers are circulating off center. This case is similar to the previous sCPGE experiment when the beam is incident at the left or right side of electrodes leading to measurable sCPGE with the help of field. For field in the opposite direction, the carrier would be shifted to the other side of the sample, leading to CPGE current with opposite sign. The longitudinal field can only shifts the carriers between two electrodes and the sCPGE is still not measurable due to the symmetry. This explanation matches all of the observation above. To simplify the origin of the CPGE current, homogeneous illumination is better to be carried out in the measurement instead of focused Gaussian beam.

Therefore, the 60X objective lens was replaced by a 10X lens (Fig 4.11) to make the beam few times larger than the sample flake. Weyl semimetal $Mo_{0.9}W_{0.1}Te_2$ flake with area 20 um $\times$ 20 um was illuminated by beam whose diameter was about 50 um. Within the measurement regime in the center of the sample, the beam intensity gradient could be negligible. Transverse bias voltage magnitude varied from -15mV to 15mV with increments of 2 mV. The beam position and size were fixed during the whole measurement process. At each transverse bias, total photocurrent was collected while rotating the quarter wave plate and plotted as function of ϕ. The contribution from CPGE and LPGE was taken out by fitting into the equation. In Fig 4.12, the CPGE and LPGE current were shown as the function of transverse bias. Both CPGE and LPGE show linear

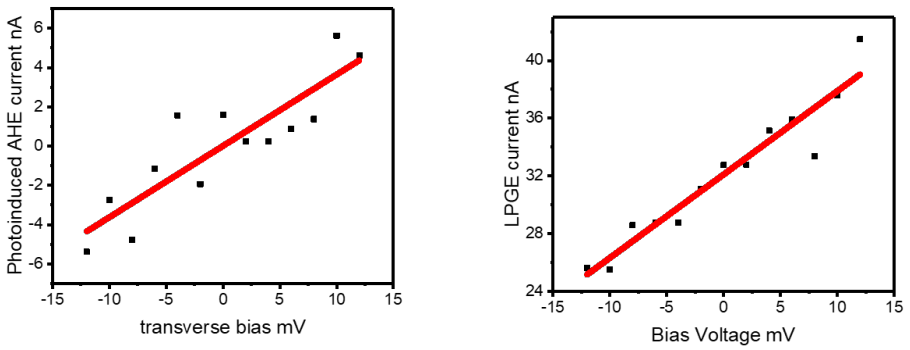

FIGURE 4.12: CPGE (left) and LPGE (right) current on $Mo_{0.9}W_{0.1}Te_2$ under illuminated of big beam spot with transverse bias from -15 mV to +15 mV. The contribution from circularly polarized light and linearly polarized light are obtained by fitting the total photocurrent. The black dots are current data and the red line is linear fitting of the CPGE/LPGE current dependence on bias voltage.

relationship with the transverse bias. Without the influence from sCPGE, this CPGE current was confirmed to be the photoinducded AHE current. Thus, in one hand, the results can be viewed as CPGE appearing in a symmetry forbidden system due to the transverse electric field; in the other hand, it can also be treated as a hall effect in non-magnetic system induced by circular polarized light.

According to the beam size dependence experiment in Chapter 3, sCPGE can not be efficiently collected if the distance between electrodes is much larger or smaller than the beam size. Therefore, by focusing the beam to be the smallest spot by 60X lens ($\sim$ 2 um) on a larger sample flake, the sCPGE contribute can also be excluded. To further confirm the mechanism of this photoinduced AHE, the measurement was performed again on a larger $Mo_{0.9}W_{0.1}Te_2$ flake with electrodes separated for 10um with 2um size focused beam. (Fig 4.13) The dependence of CPGE on bias voltage was the same as big beam spot measurement in Fig 4.12, showing linear relationship. This result was another strong evidence to prove that the sCPGE did not contribute to these photoinduced AHE measruements. Avoiding the influence of edge, the noise of focused beam situation (R=0.9931) was smaller than at big beam experiment (R=0.8756). Therefore, focused beam would be utilized for the following experiments.

The result of the different beam size experiments was a strong evidence that the

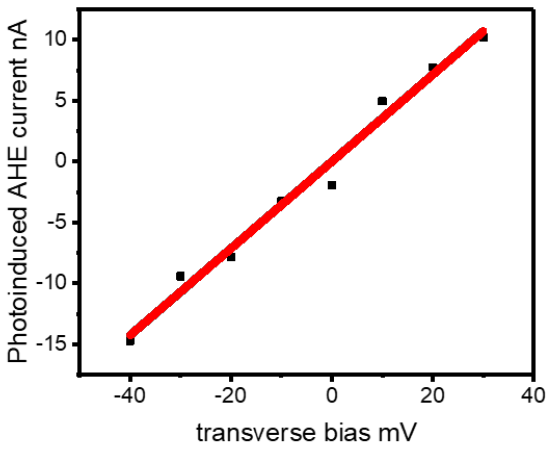

FIGURE 4.13: CPGE current extracted by photocurrent on $Mo_{0.9}W_{0.1}Te_2$ under focused beam with transverse bias from -40 mV to +30 mV. The black dots are experimental data and the red lines are linear fitting of the CPGE current dependence on bias voltage.

observed CPGE does not come from the sCPGE shifted by the transverse electric field. However, to further reveal the origin of this phenomena, more properties of this effect were required to be explore by new experiments. To understand the generality of this photoinduced AHE, the measurements were carried out on the central symmetric phase $MoTe_2$ at room temperature. Similar size $MoTe_2$ flakes (20 um $\times$ 20 um) were prepared on the SiO_2/Si substrate with Ti/Cu electrodes patterned as Fig 4.8. Focused beam with diameter 2 um was normal incident at the sample center and the electrode pair for photocurrent measurement was separated for 10 um. Transverse bias voltage was chosen to be 100 mV, 0 mV and -100 mV. Polarized dependent photocurrents were collected at each bias and the results were shown in the Fig 4.14. Qualitatively, the observation was similar to measurement on $Mo_{0.9}W_{0.1}Te_2$: the CPGE contribution was zero without bias; while under positive and negative transverse field, CPGE current showed up with comparable amplitude but opposite sign. However, quantitatively speaking, the effect was much weaker in $MoTe_2$. Compare with the result in $Mo_{0.9}W_{0.1}Te_2$ whose CPGE current was 10 nA under 3 mV transverse bias, J_C obtained in $MoTe_2$ with 100 mV after fitting is about 4 nA, meaning that the CPGE current in $Mo_{0.9}W_{0.1}Te_2$ was almost 100

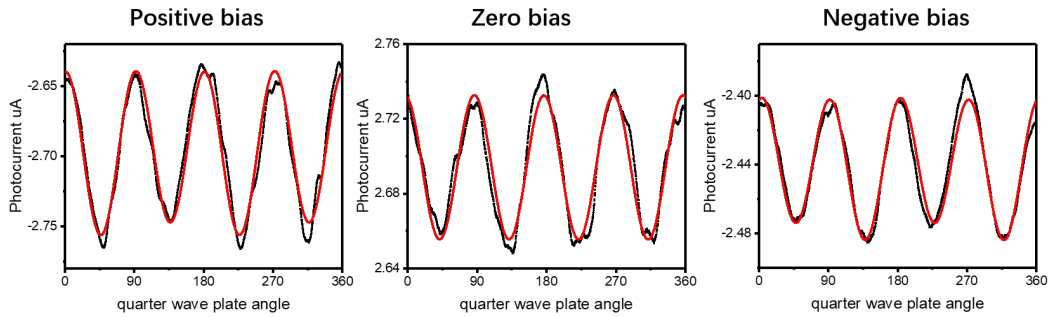

FIGURE 4.14: Photocurrents collected on room temperature $MoTe_2$ under illuminated of focused beam with transverse bias at 100 mV (left), 0 mV (middle) and -100 mV (right) is plotted as function of quarter wave plate angle. The black dots are current data and the red line is the fitting curve using the phenomenological equation. At positive bias, J_C=4.5 nA and J_L=56.9 nA; at negative bias, J_C=-4.9 nA and J_L=38.51 nA.

times larger than in $MoTe_2$ for same circumstance.

As stated in Chapter 2 and Chapter 3, the in-plane crystal structure at room temperature of $Mo_{0.9}W_{0.1}Te_2$ and $MoTe_2$ are very similar, the difference is that the former is Weyl semimetal due to inversion symmetry breaking while the later one has inversion symmetry. The significant magnitude difference between the 1T′ phase and T_d naturally raised a hypothesis that the inversion symmetry breaking Weyl phase was likely to greatly enhance the anomalous Hall effect. To confirm this different behaviours at 1T′ phase and T_d phase of photoinduced AHE, same compound of material at different phase is better for comparison. The temperature induced phase change property in $MoTe_2$ could be utilized for comparing the 1T′ phase and the T_d phase. Since the phase change occurs at 250 K, the measurement was performed on $MoTe_2$ at 77 K. The temperature was controlled by a heating stage in a cryostat and liquid nitrogen and monitored by a thermocouple. The pressure was maintained below $10^{-6} Torr$ by a turbo pump.

Photocurrent was measured as the function of quarter wave plate rotaion angle when bias voltage was applied at 20 mV, 10 mV, 0 mV, -10 mV and -20 mV. (Fig 4.15) The result at low temperature was significantly different from room temperature: the CPGE was greatly affected by the transverse bias; in other words, there was a significant photoinduced AHE in the T_d phase of $MoTe_2$. With 20 mV bias, the photocurrent at left circularly polarized light ($\phi = 45^\circ$ and 225°) was higher than at right circular

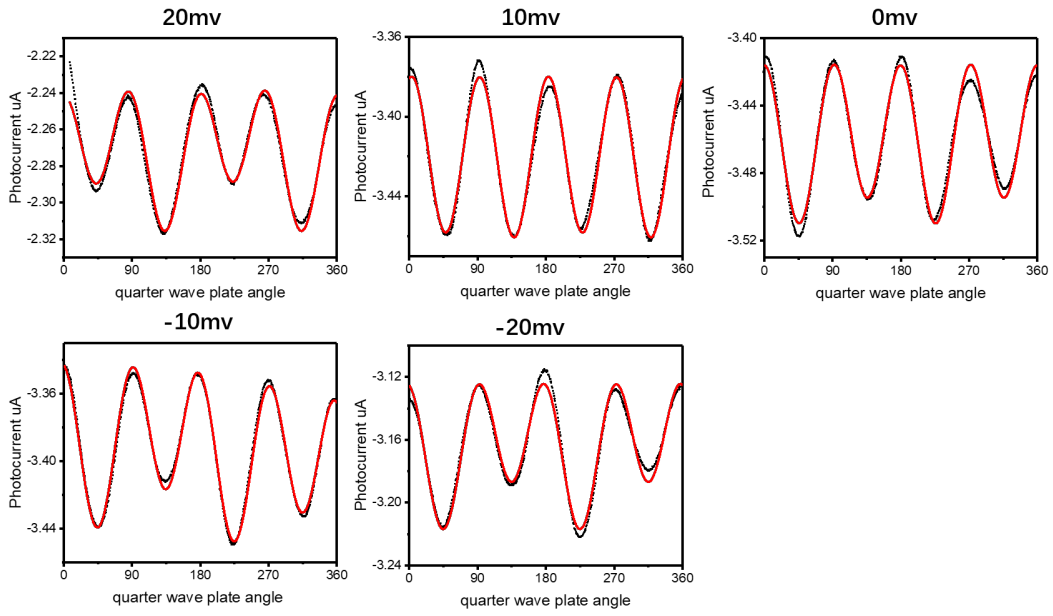

FIGURE 4.15: Photocurrents collected on 77 K $MoTe_2$ under illuminated of focused beam with transverse bias at 20 mV, 10 mV, 0 mV, -10 mV and -20 mV (marked above) is plotted as function of quarter wave plate angle. The black dots are current data and the red line is the fitting curve using the phenomenological equation. By fitting, CPGE at each bias can be obtained: J_C=13.37 nA, 1.23 nA, -7.62 nA, -12.71 nA, -15.04 nA when bias was 20 mV, 10 mV, 0mV, -10 mV and -20 mV respectively.

polarized light ($\phi = 135°$ and 315°); while under -20 mV bias, it was the opposite. By fitting into the photocurrent equation, the CPGE current changed from -15.04 nA to 13.37 nA when transverse bias varied for 40 mV, indicating AHE conductivity to be 0.71 nA/mV. Comparing with the result at room temperature phase which was smaller than 0.045 nA/mV, the effect was enhanced for more than an order. CPGE current was extracted from all these five data via fitting and plotted with the corresponding bias voltage, shown in Fig 4.16. Same as the $Mo_{0.9}W_{0.1}Te_2$ at room temperature, the CPGE current dependence on transverse bias voltage can be fitted to linear relationship. The experiment was a good evidence to show that the transverse bias induced CPGE or photoinduced AHE was significantly stronger in the T_d Weyl phase compared with the 1T' trivial phase.

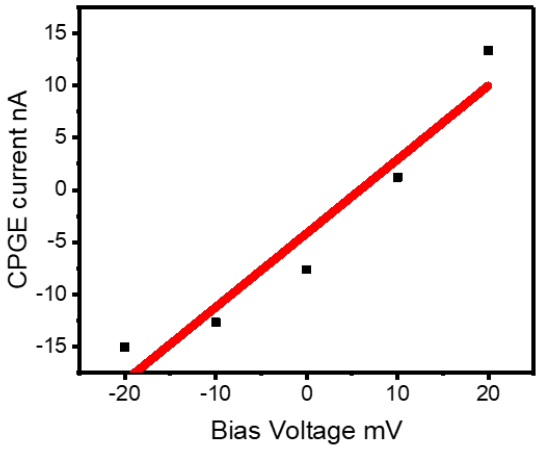

FIGURE 4.16: CPGE current on low temperature $MoWTe_2$ under focused beam with transverse bias from -20 mV to +20 mV. The contribution from circularly polarized light are obtained by fitting the total photocurrent. The black dots are current data and the red lines are linear fitting of the CPGE current dependence on bias voltage.

4.4 Mechanism

4.4.1 Symmetry arguments

CPGE effect and LPGE effect could be represented by two third rank tensors,

$$\begin{aligned} J_{i,PGE} = A_{ijk}(\omega)\left(\frac{E_j(\omega)E_k(-\omega) - E_j(-\omega)E_k(\omega)}{2}\right) \\ + B_{ijk}(\omega)\left(\frac{E_j(\omega)E_k(-\omega) + E_j(-\omega)E_k(\omega)}{2}\right) \end{aligned} \tag{4.10}$$

$A_{ijk}(\omega) = \frac{1}{2}(\vartheta_{ijk}(\omega) - \vartheta_{ijk}(-\omega))$, describes CPGE and $B_{ijk}(\omega) = \frac{1}{2}(\vartheta_{ijk}(\omega) + \vartheta_{ijk}(-\omega))$ describes LPGE. Since $MoTe_2$ has a C_{2v} point group symmetry, CPGE is characterized by two independent components, $A_{xxz} = -A_{xzx}$ and $A_{yyz} = -A_{yzy}$. Thus, CPGE current is forbidden by the two fold rotation symmetry in its x-y plane, when the light proprogates in the z direction. Similarly, LPGE, and photon drag effect are not allowed under normal incidence. It explains that in the experiment, without external electric field, there was no CPGE nor LPGE observed.

Then, when an electric field is applied, at least one mirror symmetry in plane would

be broken, and the symmetry of the system would be reduced to C_s. Assuming that the electric field is applied along y direction (crystallographic a axis), CPGE tensor would have two more nonzero components, $A_{xxy} = -A_{xyx}$. As a result, CPGE current could be observed along x (crystallographic b axis) direction. When the electric field is applied along an arbitrary direction, i.e. having a θ polar angle, then four more nonzero components would appear in CPGE tensor, $A_{xxy} = -A_{xyx}, A_{yxy} = -A_{yyx}$ but those coefficients will be correlated as $A_{xxy} = A_{yxy} \cdot tan\theta$. It implies that CPGE current would always be perpendicular to the external electric field, as observed in the experiment.

4.4.2 Phenomenological description

With above symmetry arguments to explain the existence of this optically induced Hall effect in $MoTe_2$, here we use a phenomenological model to explore its physical insights.

$$j_{CPGE,kij} = \sum_{k,n} \rho^{(2)}_{nn} v_{nn}$$
$$= \sum_{k,n,m} \frac{e^3}{\hbar^2} (\delta(\epsilon_m - \epsilon_n - \omega))(f_0(\varepsilon_m) - f_0(\varepsilon_n))(R^i_{nm} R^j_{mn} - R^i_{mn} R^j_{nm})(v^k_{nn} - v^k_{mm}) E_i(\omega) E_j(-\omega) \tag{4.11}$$

$\rho^{(0)}_{nm} = f_0(\varepsilon_n(\mathbf{k}))\delta_{nm}$ is the Fermi-Dirac distribution at T=0. The matrix elements of the velocity operator acting on Bloch states is given by $\mathbf{v}_{nm}(\mathbf{k}) =< u_n(\mathbf{k})|\frac{\partial H_0}{\partial \mathbf{k}}|u_m(\mathbf{k})$. At energy $\varepsilon_n(\mathbf{k})$, the band-diagonal velocity is given by $\mathbf{v}_{nn} = \nabla_{\mathbf{k}}\varepsilon_{\mathbf{n}} \cdot \frac{D}{D\mathbf{k}}$ defined as $\frac{DO}{D\mathbf{k}} = \nabla_{\mathbf{k}} O - i[R(\mathbf{k}), O]$is the momentum space covariant derivative operator on an arbitrary matrix O, where $\mathbf{R}_{nm}(\mathbf{k}) = i < u_n(\mathbf{k})|\frac{\partial u_m(\mathbf{k})}{\partial \mathbf{k}} >$ is the non-diagonal Berry connection. When $n \neq m, \mathbf{R}_{nm}(\mathbf{k}) = \frac{v_{nm}(\mathbf{k})}{i(\varepsilon_n(\mathbf{k}) - \varepsilon_m(\mathbf{k}))}$. $\rho^{(2)}$ is the second order in electric field density matrix, or the so called transition matrix. The quantity that appears in equation 4.11, which we call a band resolved Berry curvature $\Omega^k_{nm}(\mathbf{k}) = -i(R^i_{nm} R^j_{mn} - R^i_{mn} R^j_{nm})$ along $\hat{k} = \hat{i} \times \hat{j}$ is associated with the berry curvature $\mathcal{B}^k_n(\mathbf{k})$, $\mathcal{B}^k_n(\mathbf{k}) = \Sigma_m \Omega^k_{nm}(k)$. It transforms like Berry curvature: $\Omega^k_{nm}(\mathbf{k}) = \Omega^k_{nm}(-k)$ under inversion symmetry, and $\Omega^k_{nm}(\boldsymbol{k}) = -\Omega^k_{nm}(-\mathbf{k})$ under time reversal symmetry. Therefore, in a system with both

time reversal and inversion symmetry, $\Omega^{ij}_{nm}(\mathbf{k})$ vanishes. In a two band system, this band density collapses into the real Berry curvature.

CPGE current vanishes in $MoTe_2$ because the band velocity and the diagonal terms of the second order density matrix, are both symmetric under C_{2v} symmetry. In a weak field limit, the effect of electric field on the CPGE tensor is reflected mostly on the electron density matrix. An external electric field would shift the electron distribution in the Brilioun zone, rendering the Fermi-Dirac distribution $(f_0(\varepsilon_m) - f_0(\varepsilon_n))$ asymmetric on the Fermi surface. Consequently, $\rho^{(2)} = \Omega^{ij}_{nm}(\delta(\epsilon_m - \epsilon_n - \omega))(f_0(\varepsilon_m) - f_0(\varepsilon_n))$ would not be symmetric under C_{2v} symmetry with the electric field.

To treat this perturbatively, the new tensor elements will be linear in the dc electric field. Density matrix $\Delta\rho^{(2)} \sim E_{dc}\Omega^{ij}_{nm}(\delta(\epsilon_m - \epsilon_n - \omega))(f'_0(\varepsilon_m) - f'_0(\varepsilon_n))$ is now weighted by a new k-dependent Fermi-Dirac distribution. Therefore, the Hall angle is expected to be highly dependent on the 'Berry curvature band density' in the system. To compare the two phases of $MoTe_2$, the high temperature 1T' phase has inversion symmetry and no Berry curvature band density, while the low temperature Weyl T_d phase has a large Berry curvature. Although in both phases, the electric field modulation are allowed, their magnitude could be different by orders, which is in good agreement with our measurements.

4.5 Conclusion

In summary, transverse bias induced CPGE was observed in room temperature Weyl semimetal $Mo_{0.9}W_{0.1}Te_2$ under normal incident light. The CPGE current showed opposite direction when the transverse bias flipped the sign. The influence of circulating sCPGE current by various beam size, this phenomenon was confirmed to be photoinduced AHE. Applied by different transverse bias, the current generated by the circular polarized light was revealed to have linear dependence on the transverse field.

Different behaviours at 1T' phase and T_d phase of this effect was obtained by performing the measurements on topological phase transition material $MoTe_2$ at room

temperature (1T') and 77 K (T_d). The result at Weyl phase $MoTe_2$ was the same as $Mo_{0.9}W_{0.1}Te_2$, suggesting consistent photoinduced AHE in Weyl semimetal. However, the AHE response at 1T' phase was much smaller or even negligible compared with Weyl phase. This was the first time for the photoinduced AHE experimentally observed in the time reversal symmetry preserved Weyl semimetal.

For symmetry argument, the in-plane symmetry of Weyl semimetal $Mo_{0.9}W_{0.1}Te_2$ is reduced by transverse field, allowing the present of CPGE current. The observation of CPGE magnitude linearly dependence on transverse field is also explained by a phenomenological equation. By derivation of response function of CPGE current, the dominate term in CPGE current expression consist of the band resolved Berry curvature, implying the significantly different AHE conductivity between the 1T' phase and the T_d phase.

In the future, we will try to perform the photoinduced anomalous Hall effect within the Liftshiz energy scale and explain the result by DFT calculation. With less band involved, real band model could be easier to be carried out and the microscopic origin of the AHE conductivity is expected to be extracted from the calculation. The significant Hall conductivity difference with and without inversion symmetry in two phases of $MoTe_2$ is likely to be numerically calculated and fitted into the experimental results. By this nonlinear optical response, we will try to probe the Berry curvature and band structure of the Weyl semimetal.

Bibliography

[1] Hall, E. (1879). On a New Action of the Magnet on Electric Currents. American Journal of Mathematics, 2(3), 287-292. doi:10.2307/2369245

[2] Hall, E., 1881, Philos. Mag. 12, 157.

[3] Kundt, A. "A. Kundt, Wied. Ann. 49, 257 (1893)." Wied. Ann. 49 (1893): 257.

[4] Webster, W.L., 1927, July. The Hall effect in single crystals of iron. In Mathematical Proceedings of the Cambridge Philosophical Society (Vol. 23, No. 7, pp. 800-803). Cambridge University Press.

[5] Smith, A.W., 1910. AW Smith, Phys. Rev. 30, 1 (1910). Phys. Rev., 30, p.1.

[6] Pugh, E.M. and Lippert, T.W., 1932. Hall emf and intensity of magnetization. Physical Review, 42(5), p.709.

[7] Pugh, E.M., 1930. Hall effect and the magnetic properties of some ferromagnetic materials. Physical Review, 36(9), p.1503.

[8] Karplus, R. and Luttinger, J.M., 1954. Hall effect in ferromagnetics. Physical Review, 95(5), p.1154.

[9] Smit, J., 1955. The spontaneous Hall effect in ferromagnetics I. Physica, 21(6-10), pp.877-887.

[10] Smit, J., 1958. The spontaneous Hall effect in ferromagnetics II. Physica, 24(1-5), pp.39-51.

[11] Berger, L., 1970. Side-jump mechanism for the Hall effect of ferromagnets. Physical Review B, 2(11), p.4559.

[12] Nagaosa, N., Sinova, J., Onoda, S., MacDonald, A.H. and Ong, N.P., 2010. Anomalous hall effect. Reviews of modern physics, 82(2), p.1539.

[13] Xiao, D., Chang, M.C. and Niu, Q., 2010. Berry phase effects on electronic properties. Reviews of modern physics, 82(3), p.1959.

[14] MacDonald, A. and Niu, Q., 2004. New twist for magnetic monopoles. Physics World, 17(1), p.18.

[15] Onoda, S., Sugimoto, N. and Nagaosa, N., 2006. Intrinsic versus extrinsic anomalous Hall effect in ferromagnets. Physical review letters, 97(12), p.126602.

[16] Jungwirth, T., Niu, Q. and MacDonald, A.H., 2002. Anomalous Hall effect in ferromagnetic semiconductors. Physical review letters, 88(20), p.207208.

[17] Onoda, S., Sugimoto, N. and Nagaosa, N., 2006. Theory of Non-Equilibirum States Driven by Constant Electromagnetic Fields: —Non-Commutative Quantum Mechanics in the Keldysh Formalism—. Progress of theoretical physics, 116(1), pp.61-86.

[18] Dai, X. and Zhang, F.C., 2007. Light-induced Hall effect in semiconductors with spin-orbit coupling. Physical Review B, 76(8), p.085343.

[19] Miah, M. Idrish. "Observation of the anomalous Hall effect in GaAs." Journal of Physics D: Applied Physics 40.6 (2007): 1659.

[20] Yu, J.L., Chen, Y.H., Jiang, C.Y., Liu, Y., Ma, H. and Zhu, L.P., 2012. Observation of the photoinduced anomalous Hall effect spectra in insulating InGaAs/AlGaAs quantum wells at room temperature. Applied Physics Letters, 100(14), p.142109.

[21] Yin, C.M., Tang, N., Zhang, S., Duan, J.X., Xu, F.J., Song, J., Mei, F.H., Wang, X.Q., Shen, B., Chen, Y.H. and Yu, J.L., 2011. Observation of the photoinduced anomalous Hall effect in GaN-based heterostructures. Applied Physics Letters, 98(12), p.122104.

[22] Yin, C.M., Tang, N., Zhang, S., Duan, J.X., Xu, F.J., Song, J., Mei, F.H., Wang, X.Q., Shen, B., Chen, Y.H. and Yu, J.L., 2011. Observation of the photoinduced anomalous Hall effect in GaN-based heterostructures. Applied Physics Letters, 98(12), p.122104.

[23] Li, J.B., Wu, X.G., Wang, G.W., Xu, Y.Q., Niu, Z.C. and Zhang, X.H., 2016. Helicity-dependent photocurrent induced by the in-plane transverse electric current in an InAs quantum well. Scientific reports, 6, p.31189.

[24] Zyuzin, A.A. and Tiwari, R.P., 2016. Intrinsic anomalous Hall effect in type-II Weyl semimetals. JETP letters, 103(11), pp.717-722.

[25] Chan, C.K., Lee, P.A., Burch, K.S., Han, J.H. and Ran, Y., 2016. When chiral photons meet chiral fermions: photoinduced anomalous Hall effects in Weyl semimetals. Physical review letters, 116(2), p.026805.

Chapter 5

Future Work

5.1 Introduction

Even though the conventional CPGE was forbidden under normally incident light [1–3] because of the in-plane two-fold symmetry, different methods were used to reduce the symmetry and CPGE current in $MoWTe_2$ Weyl semimetal family was successfully observed. Breaking the symmetry by focused beam, a novel CPGE working in a broad spectral range was obtained in type-II Weyl semimetals, such as $T_d - MoTe_2$, $Mo_{0.9}W_{0.1}Te_2$ and $Mo_{0.3}W_{0.7}Te_2$ and was named as sCPGE. This effect exhibited same properties in various Weyl semimetal compounds and showed same phenomenology at different excitation energy. Photocurrent of sCPGE was proven to be circulating around the beam center and the current magnitude was controlled by the beam gradient. The circulating direction at high energy excitation was observed to be opposite from the direction at low energy, which was related to the band crossing property of Weyl semimetal. The frequency dependent phenomenon could inspire further interests in probing the band topology of Weyl semimetals. Besides, the sCPGE with more degree of freedom could have promising application in current engineering.

CPGE was also achieved in type-II Weyl semimetal by applying transverse bias voltage while the sample was normally incident by homogeneous illumination. The CPGE current magnitude showed linear relationship with the electric field. This effect was called photoinduced anomalous Hall effect, which was also working in wide excitation

energy. Observed by experiments and explained by response function, AHE conductivity was shown to be much larger in the inversion symmetry breaking Weyl phase but negligible small in 1T′ phase. At low energy excitation, more information of the Berry curvature and the Weyl node could be expected to be extracted by this photoinduced AHE.

5.2 Probing band crossing of $MoWTe_2$ alloys by sCPGE

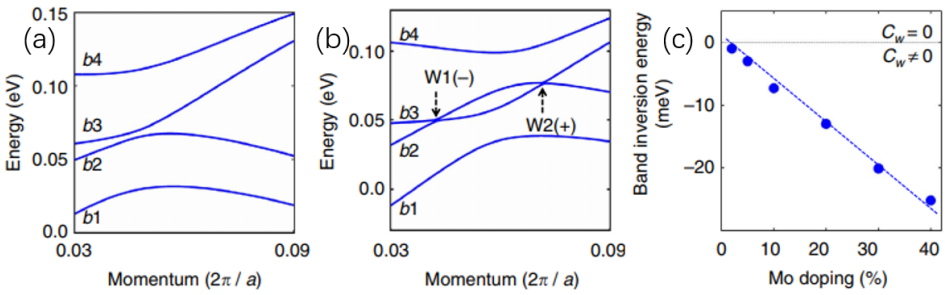

FIGURE 5.1: (a)Band structures of WTe2 along momentum space cut. (b) Band structures of Mo0.2W0.8Te2 along momentum space cut. (c)The energy difference between the extrema of the b2 and b3 bands as a function of Mo doping x. This characterizes the magnitude of the band inversion. Reprinted figure with permission from [4]

Calculated by theory [4] and observed by ARPES [5], the Fermi arc in $MoWTe_2$ alloys was shown to be tunable by different Mo concentration. As shown in Fig 5.1, there is no band inversion in pure WTe_2; while bands gradually touching each other with Mo doping. The band inversion increases with higher Mo doping concentration. As mentioned in Chapter 3, sCPGE current measured at the same spot of type-II Weyl semimetal with same circularly polarized light reversed direction at 750nm wavelength and 6um, which was related to the band crossing in the band structure of $Mo_{0.9}W_{0.1}Te_2$. Therefore, by adjusting the wavelength step by step, the sCPGE-wavelength dependence can be obtained.

For $Mo_xW_{1-x}Te_2$ alloys with different concentration x, we can repeat the sCPGE-wavelength dependence experiments and measure the zero sCPGE wavelength for

each x. Because smaller band crossing is expected at higher x, the sign reverse of sCPGE should occurs at lower photon energy and longer light wavelength. Through this experiment, the mechanism of sCPGE can be further confirmed and the topological band crossing in Weyl semimetal can be probe by nonlinear optical response. This effect can be a promising tool to detect Weyl semimetal and study other topological materials in the further.

5.3 CPGE Current Engineering by Beam Profile

Giant CPGE current was generated to circulating around the focused beam and controlled by the beam gradient. The reason why the beam was circulating was because the beam was Gaussian profile. What if the beam gradient has other distribution? In principle, the CPGE current distribution can be patterned to any shape via engineering the beam gradient. It will be very interesting and useful to manually control the current in plane with optical excitation.

Multi-beam can be utilized and incident on the type-II Weyl semimetal at the same time but different position. By controlling the helicity, beam position and beam size of each light source, the CPGE current is expected to flowing on the sample surface as a curve. Electrodes can be fabricated on the sample in the current path to confirm the CPGE current magnitude and direction.

The in-plane current engineering can also be achieved by homogeneous light source. Inhomogeneous polymer can be pre-coated on the top of Weyl semimetal $Mo_{0.9}W_{0.1}Te_2$. Even though the beam profile is even, the sample can experience spatially different light intensity due to the coating layer. With well designed coating pattern, electrical circuits on the sample can be switched on/off by right/left circularly polarized light. This experiment has potiential application in on-chip lab and computing in the future.

Furthermore, with the information of beam profile and light helicity, sCPGE can also be utilized for detector. Under the illumination of unknown beam, sCPGE current

could be generated, whose sign and magnitude are controlled by light circular polarization and beam gradient respectively. By patterning the electrode array on the Weyl semimetal sample, we can measure the photocurrent between each two electrodes. Therefore, the light polarization and beam profile can be detected and mapped out, which is a promising tool for future sensor and detector.

5.4 Low Energy Excitation of Photoinduced AHE

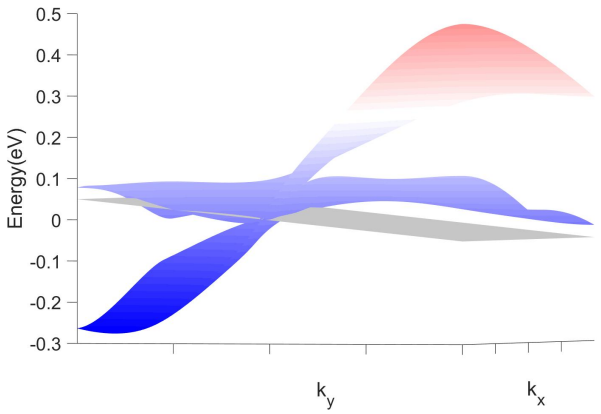

FIGURE 5.2: Calculated band structure of $MoTe_2$ with dc electric field modulated Fermi surface

By applying electric field in x-y plane, the Fermi surface will be modified and tilted in the momentum space. The band structure of the crossing regime was calculated and shown in Fig 5.2. The tilted Fermi surface was represented by the grey color plane. The tilting angle was determined by the field. Therefore, under certain bias, some Weyl points will locate above the Fermi level while the other Weyl point below the Fermi level.

Low energy excitation below Lifshitz energy can be designed for photoinduced anomalous Hall effect. With small electrical field, all Weyl points are above the Fermi level and the transition are allowed for all Weyl cones under circularly polarized light. Gradually increase the transverse bias, transition of a Weyl cone will be muted eventually, since the Weyl point is too high above the tilted Fermi surface. Further increase the

field, only the transition in the other Weyl cone is expected. Extract the CPGE current at each transverse bias, photoinduced AHE current can be plotted as the function of bias. The contribution of AHE current is different before and after some Weyl points are muted, which means that the AHE conductivity is supposed to be discontinuous, represented by different AHE current-transverse bias slope. Through photoinduced AHE, Weyl cones can be probed separately and more band information can be extracted.

Bibliography

[1] Ivchenko E., Ganichev S. Spin Physics in Semiconductors. Springer; 2008.

[2] Ganichev S. D., Prettl W.; Spin photocurrents in quantum wells; Journal of physics: Condensed matter 15 (20), R935 (2003).

[3] Shalygin V., Moldavskaya M., Danilov S., Farbshtein I., Golub L.; Circular photon drag effect in bulk tellurium; Physical Review B 93 (4), 045207 (2016).

[4] Chang, T.R., Xu, S.Y., Chang, G., Lee, C.C., Huang, S.M., Wang, B., Bian, G., Zheng, H., Sanchez, D.S., Belopolski, I. and Alidoust, N., 2016. Prediction of an arc-tunable Weyl Fermion metallic state in $Mo_xW_{1-x}Te_2$. Nature communications, 7, p.10639.

[5] Belopolski I., Sanchez D. S., Ishida Y., Yu P., Zhang S. S., Chang T.-R., Chang G., Pan X., Lu H., Zheng H.; Topological Weyl phase transition in $Mo_xW_{1-x}Te_2$; arXiv preprint arXiv:1612.07793, (2016).